Experimental study of the rotating-disk boundary-layer flow

by

Shintaro Imayama

May 2012
Technical Reports from
Royal Institute of Technology
KTH Mechanics
SE-100 44 Stockholm, Sweden

Akademisk avhandling som med tillstånd av Kungliga Tekniska Högskolan i Stockholm framlägges till offentlig granskning för avläggande av teknologie licentiatsexamen den 8 juni 2012 kl 10.15 i Seminarierrummet, Brinellvägen 32, Kungliga Tekniska Högskolan, Stockholm.

Universitetsservice US–AB, Stockholm 2012

Shintaro Imayama 2012, **Experimental study of the rotating-disk boundary-layer flow**
Linné FLOW Centre, KTH Mechanics, Royal Institute of Technology
SE–100 44 Stockholm, Sweden

Abstract

Rotating-disk flow has been investigated not only as a simple model of cross flow instability to compare with swept-wing flow but also for industrial flow applications with rotating configurations. However the exact nature of laminar-turbulent transition on the rotating-disk flow is still major problem and further research is required for it to be fully understood, in particular, the laminar-turbulent transition process with absolute instability. In addition the studies of the rotating-disk turbulent boundary-layer flow are inadequate to understand the physics of three-dimensional turbulent boundary-layer flow.

In present thesis, a rotating-rotating disk boundary-layer flow has been investigated experimentally using hot-wire anemometry. A glass disk with a flat surface has been prepared to archieve low disturbance rotating-disk environment. Azimuthal velocity measurements using a hot-wire probe have been taken for various conditions. To get a better insight into the laminar-turbulent transition region, a new way to describe the process is proposed using the probability density function (PDF) map of azimuthal fluctuation velocity.

The effect of the edge of the disk on the laminar-turbulent transition process has been investigated. The disturbance growth of azimuthal fluctuation velocity as a function of Reynolds number has a similar trend irrespective of the various edge conditions.

The behaviour of secondary instability and turbulent breakdown has been investigated. It has been found that the kinked azimuthal velocity associated with secondary instability just before turbulent breakdown became less apparent at a certain wall normal heights. Furthermore the turbulent breakdown of the stationary mode seems not to be triggered by its amplitude, however, depend on the appearance of the travelling secondary instability.

Finally, the turbulent boundary layer on a rotating disk has been investigated. An azimuthal friction velocity has been directly measured from the azimuthal velocity profile in the viscous sub-layer. The turbulent statistics normalized by the inner and outer sclaes are presented.

Descriptors: Fluid mechanics, boundary layer, rotating disk, laminar-turbulent transition, convective instability, absolute instability, secondary instability, crossflow instability, hot-wire anemometry.

Preface

This licentiate thesis within the area of fluid mechanics deals with boundary-layer flow on a rotating disk based on experimental work, including the instability, laminar-turbulent transition and fully developed turbulence. The thesis is divided into two parts. The first part contains an introduction, an overview, summary of the present study and an appendix giving the governing equations. Ths second part consists of four papers. One of them has already been published however it is presented in a different format here to align with the formatting of the thesis. In chapter 5 of the first part of the thesis, the authors' contributions to the papers are stated.

May 2012, Stockholm
Shintaro Imayama

Contents

Part I

Overview and summary

CHAPTER 1

Introduction

An incompressible boundary layer over a rotating disk without any imposed flow is discussed in this study. The aim of this experimental work is to investigate the laminar-turbulent transition process and turbulence on the rotating-disk boundary-layer flow.

The flow is purely driven by the disk rotation. The laminar boundary layer has a three-dimensional velocity profile with an inflection point in the radial velocity component. This boundary layer is known as the 'von Kármán boundary layer' and it belongs to a family of rotating boundary-layer flows, including the so-called Bödewadt, Ekman and von Kármán boundary layers (BEK boundary layers) that are exact solutions of the Navier-Stokes equations. The differences between these flows are characterized by the Rossby number Ro, which is written as

$$Ro = \frac{\Omega_f^* - \Omega_d^*}{\Omega_a^*} \tag{1.1}$$

$$\text{with } \Omega_a^* = (\Omega_f^* + \Omega_d^*)/4 + ((\Omega_f^* + \Omega_d^*)^2/16 + (\Omega_f^* - \Omega_d^*)^2/2)^{1/2},$$

where Ω_f^* and Ω_d^* are the fluid angular velocity outside the boundary layer and the disk angular velocity (Arco *et al.* 2005), respectively. Ro on this study is -1 as $\Omega_f^* = 0$ and therefore $\Omega_a^* = \Omega_d^*$. The flow is also characterized by the Reynolds number, which is the ratio of inertial forces to viscous forces. It is defined as

$$R = r^* \sqrt{\frac{\Omega^*}{\nu^*}}, \tag{1.2}$$

where r^* is the radius of the disk at the measurement position, Ω^* is the angular velocity of the disk, ν^* is the kinematic viscosity of the fluid and * denotes a dimensional quantity.

The radial velocity component with an inflection point satisfies Rayleigh's inflection-point criterion which relates to the existence of an inviscidly unstable mode. The rotating-disk flow is therefore inviscidly unstable, namely it remains

unstable at infinite Reynolds number. Three-dimensional boundary layers that have an inviscid instability such as this are said to have 'crossflow instability'.

The rotating-disk boundary-layer flow has been used as a model for the flow over a swept wing because of the similarity of the velocity profiles and because both flows are susceptible to crossflow instability since the work by Gregory *et al.* (1955). Furthermore there is an advantage in investigating the crossflow instability of a rotating-disk flow rather than swept-wing flow. Because the rotating-disk flow is independent of a pressure-gradient parameter or a variable sweep angle that are required for the boundary layer flow over a swept wing. However, the flow over the rotating disk has Coriolis effects in contrast to swept-wing boundary layers. Nevertheless, Lingwood (1995*a*) found 'local absolute instability', attributed by an inviscid mechanism in the rotating-disk boundary layer, linked to the onset of nonlinearity and transition and therefore the Coriolis and streamline curvature effects were shown not to be of primary importance to the laminar-turbulent transition mechanism. Lingwood (1997*b*) revealed that the flow over the swept wing could in certain circumstances be absolutely unstable in the chordwise direction but because the swept wing has no spanwise periodicity the laminar-turbulent transition could still be a convective process.

The exact nature of the laminar-turbulent transition process for the rotating-disk flow is still not well understood. In particular, to what extent the absolute instability is involved in the transition process. This study helps us to understand a nature of the absolutely-unstable crossflow instability. Flows driven by one or more rotating disks have constituted a major field of study in fluid mechanics since the last century. Many application areas, such as rotating machinery, viscometry, computer storage devices and crystal growth processes, require the study of rotating flows (Brady 1987). Thus, this study will help the understanding of flows in more complicated applications.

The thesis is organised as follows: Part I, chapter 2, will continue describing the basis of the work, including the aims of the study, application examples, previous authors' work and the governing equations; chapter 3 describes the experimental set-up and measurement method including the calibrations. Part I ends with a summary of results and a list of publications as well as describing the author's contribution to the papers in chapter 4 and 5, respectively. Part II contains four papers on various aspects of the rotating-disk flow.

CHAPTER 2

Rotating-disk flow studies

This chapter will introduce, first of all, the basic equations govering rotating-disk flow. Then an overview of the rotating-disk flow following previous authours' studies since the derivation of the von Kármán (1921) similarity solution for an infinite disk rotating in otherwise quiscent fluid is described. Thus overview of recent studies of laminar-turbulent transition of the rotating-disk boundary-layer flow is discussed. Then application examples of the rotating-disk flow are introduced to specify the importance of this study for an industrial applications. Finally, the concepts of convective instability and absolute instability are discussed.

2.1. The governing equations

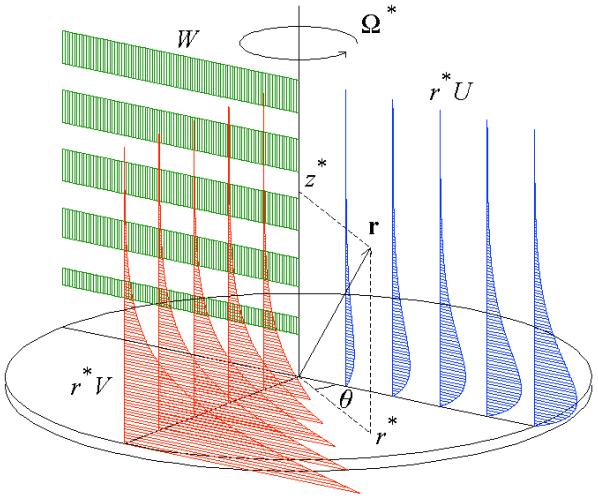

FIGURE 2.1. A sketch of the von Kármán boundary layer on a rotating-disk showing the mean velocity profiles (in a stationary laboratory frame).

The rotating-disk flow system is modelled in a cylindrical coordinate system as an infinite planar disk with a constant angular speed Ω^*. The position vector is given as $\mathbf{r} = (r^* \cos\theta, r^* \sin\theta, z^*)$. The instantaneous velocity vector is represented by $\mathbf{v} = (\tilde{u}^*, \tilde{v}^*, \tilde{w}^*)$. The rotation vector is given by $\boldsymbol{\omega} = (0, 0, \Omega^*)$. The continuity equation and Navier-Stokes equation (NSE) in a uniformly rotating co-ordinate system are written as

$$\nabla \cdot \mathbf{v} = 0, \tag{2.1}$$

$$\frac{\partial \mathbf{v}}{\partial t^*} + (\mathbf{v} \cdot \nabla)\mathbf{v} + 2\boldsymbol{\omega} \times \mathbf{v} + \boldsymbol{\omega} \times (\boldsymbol{\omega} \times \mathbf{r}) = -\frac{1}{\rho^*}\nabla \tilde{p}^* + \nu^* \nabla^2 \mathbf{v}, \tag{2.2}$$

where $2\boldsymbol{\omega} \times \mathbf{v}$ is the Coriolis acceleration term and $\boldsymbol{\omega} \times (\boldsymbol{\omega} \times \mathbf{r})$ is a centrifugal acceleration term, $\tilde{p}^*$ is an instantaneous pressure and ρ^* and ν^* are density and kinematic viscosity of a Newtonian fluid, respectively, and ∇ and ∇^2 are the gradient and Laplace operators respectively, in cylindrical coordinates. The continuity equation and the NSE can be decomposed radial, azimuthal and axial components and are written as

Continuity equation:

$$\frac{\partial \tilde{u}^*}{\partial r^*} + \frac{1}{r^*}\frac{\partial \tilde{v}^*}{\partial \theta} + \frac{\partial \tilde{w}^*}{\partial z^*} + \frac{\tilde{u}^*}{r^*} = 0, \tag{2.3}$$

Radial component of NSE:

$$\begin{aligned} &\frac{\partial \tilde{u}^*}{\partial t^*} + \left(\tilde{u}^*\frac{\partial \tilde{u}^*}{\partial r^*} + \frac{\tilde{v}^*}{r^*}\frac{\partial \tilde{u}^*}{\partial \theta} + \tilde{w}^*\frac{\partial \tilde{u}^*}{\partial z^*}\right) - \frac{\tilde{v}^{*2}}{r^*} - 2\tilde{v}^*\Omega^* - r^*\Omega^{*2} \\ &= -\frac{1}{\rho^*}\frac{\partial \tilde{p}^*}{\partial r^*} + \nu^*\left[\left(\frac{\partial^2 \tilde{u}^*}{\partial r^{*2}} + \frac{1}{r^{*2}}\frac{\partial^2 \tilde{u}^*}{\partial \theta^2} + \frac{\partial^2 \tilde{u}^*}{\partial z^{*2}}\right) + \frac{1}{r^*}\frac{\partial \tilde{u}^*}{\partial r^*} - \frac{\tilde{u}^*}{r^{*2}} - \frac{2}{r^{*2}}\frac{\partial \tilde{v}^*}{\partial \theta}\right], \end{aligned} \tag{2.4}$$

Azimuthal component of NSE:

$$\begin{aligned} &\frac{\partial \tilde{v}^*}{\partial t^*} + \left(\tilde{u}^*\frac{\partial \tilde{v}^*}{\partial r^*} + \frac{\tilde{v}^*}{r^*}\frac{\partial \tilde{v}^*}{\partial \theta} + \tilde{w}^*\frac{\partial \tilde{v}^*}{\partial z^*}\right) + \frac{\tilde{u}^*\tilde{v}^*}{r^*} + 2\tilde{u}^*\Omega^* \\ &= -\frac{1}{\rho^* r^*}\frac{\partial \tilde{p}^*}{\partial \theta} + \nu^*\left[\left(\frac{\partial^2 \tilde{v}^*}{\partial r^{*2}} + \frac{1}{r^{*2}}\frac{\partial^2 \tilde{v}^*}{\partial \theta^2} + \frac{\partial^2 \tilde{v}^*}{\partial z^{*2}}\right) + \frac{1}{r^*}\frac{\partial \tilde{v}^*}{\partial r^*} - \frac{\tilde{v}^*}{r^{*2}} + \frac{2}{r^{*2}}\frac{\partial \tilde{u}^*}{\partial \theta}\right], \end{aligned} \tag{2.5}$$

Axial component of NSE:

$$\begin{aligned} &\frac{\partial \tilde{w}^*}{\partial t^*} + \left(\tilde{u}^*\frac{\partial \tilde{w}^*}{\partial r^*} + \frac{\tilde{v}^*}{r^*}\frac{\partial \tilde{w}^*}{\partial \theta} + \tilde{w}^*\frac{\partial \tilde{w}^*}{\partial z^*}\right) \\ &= -\frac{1}{\rho^*}\frac{\partial \tilde{p}^*}{\partial z^*} + \nu^*\left[\left(\frac{\partial^2 \tilde{w}^*}{\partial r^{*2}} + \frac{1}{r^{*2}}\frac{\partial^2 \tilde{w}^*}{\partial \theta^2} + \frac{\partial^2 \tilde{w}^*}{\partial z^{*2}}\right) + \frac{1}{r^*}\frac{\partial \tilde{w}^*}{\partial r^*}\right]. \end{aligned} \tag{2.6}$$

2.1.1. *Mean velocity profile*

The instantaneous velocity $(\tilde{u}^*, \tilde{v}^*, \tilde{w}^*)$ and instantaneous pressure $(\tilde{p}^*)$ are decomposed into mean (time-independent) and fluctuation (time-dependent) components, namely

$$\begin{aligned} \tilde{u}^* &= U^* + u^*, \\ \tilde{v}^* &= V^* + v^*, \\ \tilde{w}^* &= W^* + w^*, \\ \tilde{p}^* &= P^* + p^*, \end{aligned} \tag{2.7}$$

where U^*, V^*, W^* are the mean radial, azimuthal and axial velocities, P^* is the mean pressure, u^*, v^*, w^* are fluctuating velocities in the radial, azimuthal and axial directions, and p^* is the fluctuating pressure. This operation is called Reynolds decomposition. Kármán (1921) derived an exact axi-symmetric similarity solution of the Navier-Stokes equation for the (time-independent) base flow. Then velocity and pressure similarity variables are defined by

$$U(z) = \frac{U^*}{r^*\Omega^*},\ V(z) = \frac{V^*}{r^*\Omega^*},\ W(z) = \frac{W^*}{(\nu^*\Omega^*)^{1/2}},\ P(z) = \frac{P^*}{\rho^*\nu^*\Omega^*}, \tag{2.8}$$

where U, V, W are nondimensional radial, azimuthal and axial mean velocity components, P is the nondimensional mean pressure. z is the wall normal position from the disk surface normalized by the characteristic length $L^* = (\nu^*/\Omega^*)^{1/2}$, namely written as

$$z = z^*/L^*. \tag{2.9}$$

The mean basic flow equations are derived from equations (2.3–2.6), with time-independence and axi-symmetry, which yields nonlinear ordinary differential equations written as:

$$2U + W' = 0, \tag{2.10}$$

$$U^2 - V^2 + U'W - U'' = 0, \tag{2.11}$$

$$2UV + V'W - V'' = 0, \tag{2.12}$$

$$P' + WW' - W'' = 0, \tag{2.13}$$

where the prime denotes differentiation with respect to z. The boundary conditions on a rotating-disk flow are no-slip conditions at the wall, and no radial or azimuthal velocity at $z = \infty$, so in the laboratory frame they become:

$$\begin{aligned} &U(0) = 0,\ V(0) = 1,\ W(0) = 0, \\ &U(\infty) = 0,\ V(\infty) = 0. \end{aligned} \tag{2.14}$$

The solutions of the differential equations in equations (2.10–2.13) are plotted in figure 2.2. And the flow direction between azimuthal and radial components is also plotted in figure 2.3.

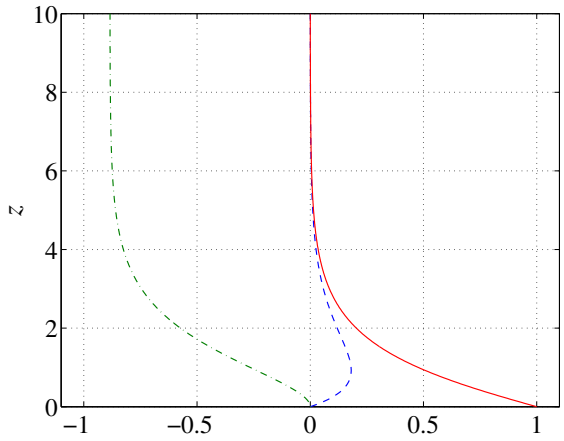

FIGURE 2.2. Laminar mean velocity profiles U (dash line), V (solid line) and W (chain line), respectively, in a stationary frame.

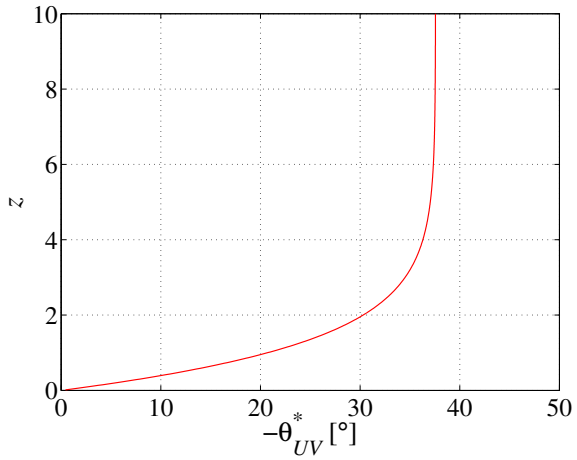

FIGURE 2.3. A laminar mean velocity angle profile of U and V.

2.1.2. *Reynolds averaged equations*

To derive the governing equations for turbulent flow over the rotating disk, Reynolds averaged continuity equation and Navier-Stokes equations (RANS) are derived from equations (2.3–2.6) with some assumptions. The detail of these derivations are described in Apendix A. To derive Reynolds averaged continuity equation, the decomposed velocity and pressure components given in equation (2.7) are substituted into equation (2.3), and time averages taken. Then derivaties with respect to the θ direction are neglected due to the axisymmetry of the mean flow. Therefore, the Reynolds averaged continuity equation becomes

$$\frac{\partial U^*}{\partial r^*} + \frac{\partial W^*}{\partial z^*} + \frac{U^*}{r^*} = 0. \tag{2.15}$$

The RANS equations are derived by substituting equation (2.7) into equation (2.4), equation (2.5) and equation (2.6) and taking time averages (denoted with an overscore). With the usual assumptions and assuming axisymmetry, the resulting RANS equations for the incompressible turbulent rotating-disk boundary-layer flow are given as

Radial component:

$$\begin{aligned} U^*\frac{\partial U^*}{\partial r^*} + W^*\frac{\partial U^*}{\partial z^*} - \frac{V^{*2}}{r} - 2V^*\Omega^* \\ = -\frac{1}{\rho^*}\frac{\partial P^*}{\partial r^*} + r^*\Omega^{*2} + \frac{1}{\rho^*}\frac{\partial}{\partial z^*}\left(\mu^*\frac{\partial U^*}{\partial z^*} - \rho^*\overline{u^*w^*}\right), \end{aligned} \tag{2.16}$$

Azimuthal component:

$$\begin{aligned} U^*\frac{\partial V^*}{\partial r^*} + W^*\frac{\partial V^*}{\partial z^*} + \frac{U^*V^*}{r^*} + 2U^*\Omega^* \\ = \frac{1}{\rho^*}\frac{\partial}{\partial z^*}\left(\mu^*\frac{\partial V^*}{\partial z^*} - \rho^*\overline{v^*w^*}\right), \end{aligned} \tag{2.17}$$

Axial component:

$$\frac{\partial \overline{w^*w^*}}{\partial z^*} = -\frac{1}{\rho^*}\frac{\partial P^*}{\partial z^*}. \tag{2.18}$$

2.2. Overview of previous studies

2.2.1. *Instabilities and laminar-turbulent transition process*

The laminar boundary-layer flow on the rotating disk has a three-dimensional profile with an inflection point in the radial direction and the exact similarity solution, which corresponds to the von Kármán similarity solution (1921) for an infinite disk rotating in an otherwise quiescent fluid. The instability and transition on the rotating-disk flow has been investigated since Theodorsen & Regier (1944) and Smith (1947) who noticed fluctuations in the boundary layer on the rotating disk using a hot-wire probe. Local stability analysis[1] (e.g. Lingwood 1995*a*) reveals that the flow can be inviscidly unstable and the critical Reynolds number (R_{CC}) for the onset of instability of the stationary mode, i.e. for disturbances that are fixed with respect to the rotating disk, is about $R_{CC} = 290$. This inviscidly unstable mode is called Type I. There is another unstable mode which is called Type II and is due to viscous effect. However for Type II stationary disturbances have smaller growth rates. Travelling disturbances can also be unstable. Hussain *et al.* (2011) showed growth rates of travelling disturbances with different frequencies. The maximum growth rates were observed for a mode travelling slowly with respect to the disk and growing at a rate larger than the stationary mode. Note also that disturbances travelling faster than the disk can have a critical Reynolds number for Type II that is lower than that for Type I. However, flow visualisation of the rotating-disk flow, e.g. by Kohama (1984), shows 31 or 32 stationary spiral vortices. The predominance of the stationary disturbances observed in experiments may be because of unavoidable roughness(es) on the surface that cause repeatable excitation of the stationry mode rather than travelling modes.

Early studies of laminar-turbulent transition of the rotating-disk flow had only considered convective instability (e.g. Huerre & Monkewitz 1990). Convective instability is descrived, for example, the linear impulse response goes to zero at infinite time at the excited position, while the disturbunce grows as it is convected downstream.

More recently the work done by Lingwood (1995*a*, 1997*a*) using Briggs' method (Briggs 1964) found that for certaing travelling waves above $R_{CA} = 507$ the flow becomes absolutely unstable.[2] This is caused by a stable upstream-travelling mode, henceforth called Type III, coaliscing with an unstable downstream travelling Type I mode. Here R_{CA} is the critical Reynolds number

[1] In order to render the perturbation equations separable, variations in R with respect to, r are neglected and this results in a 'local' stability analysis, which is often referred to as a 'parallel-flow' approximation (as it is for other boundary-layer flows) even though for the rotating-disk laminar boundary layer the boundary-layer thickness is in fact constant.

[2] Absolute instability is where the linear impulse response goes to infinity at infinite time at the excited position.

for onset of local absolute instability. Furthermore, she revealed the absolute instability of the rotating-disk flow is an inviscid mechanism and suggested that the absolute instability triggers nonlinearity what is the start of the laminar-turbulent transition process. By introducing impulsive excitation to the rotating-disk boundary-layer flow, Lingwood (1996) confirmed experimentally the absolute instability (above about $R = 507$) by tracking the trajectory of the excited wavepacket. Furthermore, she showed the onset of nonlinearity appeared at Reynolds numbers above 502 and below 514, see Lingwood (1995*b*) and the development of the laminar-turbulent transition process from there, resulting in a fully turbulent flow at about $R = 600 - 650$. She performed these experiments with a 'clean' disk to minimize the excitation of stationary disturbances and the amplitude of the primary disturbance was small enough that the peak amplitude of disturbances were 3% of the local disk speed at $R = 500$ (smaller than Balachandar *et al.*'s (1992) threshold where the root-mean-square amplitude of the primary disturbance reaches about 9% at $R = 500$). Based on these results and because she did not see clear evidence of kinks in the timeseries indicative of secondary instabilities Lingwood (1996) stated "the stationary disturbances are sufficiently small, even close to the onset of transition, for the boundary layer stability to be governed by the mean velocity profiles rather than secondary instabilities".

Davies & Carpenter (2003) performed direct numerical simulations solving the linearized Navier-Stokes equations and suggested that the convective behaviour eventually dominates even for strongly locally absolutely unstable regions and concluded that the absolute instability does not produce a *linear* amplified global mode. Othman & Corke (2006) performed experiments similar to Lingwood (1996) but using a low-amplitude and a high-amplitude initial pulse-jet excitation to create the wavepacket disturbances in the boundary-layer flow. Contrary to Lingwood (1996) the trailing edge of the wavepacket did not become fixed at R_{CA} with the low amplitude initial disturbance, and that result agrees well with the linearlized DNS of Davies & Carpenter (2003). On the other hand, the amplitude of the wavepacket with the high-amplitude initial disturbance compares better with Lingwood's (1996) results although it is not certain that the trailing edge of the wavepacket becomes fixed at R_{CA}, which would be indicative of the absolute instability.

In contrast to Lingwood's (1996) experimental observation, Kobayashi *et al.* (1980), Kohama (1984) and Wilkinson & Malik (1985) observed signs associated with secondary instability at the final stage of laminar-turbulent transition, namely just before the turbulent breakdown region. Kobayashi *et al.* (1980) who performed the flow visualization on the rotating-disk flow captured "a new striped flow pattern originating along the axis of a spiral vortex". Kohama (1984) who also carried out the visualization study suggested "ring-like vortices which occur on the surfaces of each spiral vortices [sic]".

Reynolds number	The description
R	Local Reynolds number.
R_{CC}	Critical Reynolds number of Type I instability for stationary mode.
R_{CA}	Critical Reynolds number of absolute instability.
R_t	Transition Reynolds number.
R_{edge}	Edge Reynolds number.

TABLE 1. Descriptions of various Reynolds numbers.

Furthermore both Kobayashi *et al.* (1980) and Wilkinson & Malik (1985) observed kinked velocity fluctuations just before the turbulent breakdown region. Then Wilkinson & Malik (1985) concluded that "stationary, secondary instabilities between the primary vortices were observed". From a theoretical analysis Balachandar *et al.* (1992) suggested that the travelling secondary instability appears as a pair of counter-rotating vortices. Pier (2003) suggested that a *nonlinear* approach is required to explain the self-sustained behaviour of the rotating-disk flow. He suggested that the rotating-disk boundary layer has a primary nonlinear global mode fixed by the local absolute instability, found by Lingwood (1995*a*), which has itself a secondary absolute instability that triggers the transition to turbulence.

In addition to the studies described above, Healey (2010) suggested that the proximity of the edge of the disk to the transition region is important; an effect not captured by standard analyses, which assume an infinite disk radius. He recognized the scatter of experimentally-observed transition Reynolds number R_t reported by some previous authors who performed hot-wire measurements as shown in table 2. He argued that, based on investigations of the linearized complex Ginzburg-Landau equation, the transition Reynolds number should depend on the Reynolds number at the edge of the disk, R_{edge}, where $R_{edge} = r_d^*(\Omega^*/\nu^*)^{1/2}$, r_d^* is the actual radius of the disk, with the assumption that the transition to turbulence is related to the appearance of a steep-fronted nonlinear global mode. Figure 7(b) of Healey (2010) shows the variance of the experimentally-observed transition Reynolds number depending on the edge Reynolds number compared with his theoretical prediction.

As mentioned above, the exact nature of the laminar-turbulent transition process is not yet fully understood. In particular, the behaviour of the secondary instability and its relation to its primary absolute instability, and the effects of the edge Reynolds number and edge conditions of the disk should also be investigated.

Authors	R_t	Method
Theodorsen & Regier (1944)	557	Hot-wire
Gregory, Stuart & Walker (1955)	533	Visual, China-clay
Cobb & Saunders (1956)	490	Heat transfer
Gregory & Walker (1960)	524	Pressure probe
Chin & Litt (1972)	510	Mass transfer
Fedorov *et al.* (1976)	515	Visual, napthalene
Clarkson, Chin & Shacter (1980)	562	Visual, dye
Kobayashi, Kohama & Takamadate (1980)	566	Hot-wire
Malik, Wilkinson & Orszag (1981)	520	Hot-wire
Wilkinson & Malik (1985)	550	Hot-wire
Lingwood (1996)	508	Hot-wire
Othman & Corke (2006)	539	Hot-wire

TABLE 2. Experimental R_t (differently defined) given in previous studies.

2.2.2. *Turbulent boundary-layer flow*

In contrast to the many studies of the laminar-turbulent transition process, as mentioned in the previous section, experimental results of turbulent boundary-layer flow on a rotating disk are still limited (Littell & Eaton 1994), despite many industrial applications (e.g. rotor-stator systems (Arco *et al.* 2005)). The turbulent boundary layer on a rotating disk is three-dimensional due to the crossflow driven by the centrifugal force and at the most skewed position in the boundary layer the mean crossflow velocity component reaches 11% of the local disk velocity (e.g. Littell & Eaton 1994). The early work on the turbulent rotating-disk flow was done by Goldstein (1935) who did a torque measurement. Theodorsen & Regier (1944) measured the azimuthal turbulent velocity profile using a hot-wire probe up to $R = 2646$. The velocity profile agreed well with the 1/7 power law in the measurement range. Cham & Head (1969) performed turbulent radial and azimuthal velocity profile measurements using Pitot and entrainment measurement techniques and concluded that both of azimuthal and radial velocity profiles are well fitted by Thompson's (1965) two-dimensional family and Mager's (1952) cross flow expression, respectively. They also estimated the azimuthal local skin friction coefficient using a Clauser (1954) plot, resulting in "realistic" values. Erian & Tong (1971) performed experimental turbulent statistics measurements on a rotating-disk flow and concluded that "the eddy viscosity in the turbulent boundary layer generated by the disk rotation is substantially larger than that of the turbulent boundary layer over a flat plate". Littell & Eaton's (1994) azimuthal velocity profile normalized by an inner scale acquired by a conventional two-dimensional law

of the wall, shows that compared with the two-dimensional turbulent boundary layer the rotating-disk boundary layer lacks a wake component. They suggested that the reason for the absence of a wake region was not understood because for the two-dimensional turbulent boundary layer the wake would be missing if there was a streamwise favourable pressure gradient, but this could not explain the rotating-disk case where there is no azimuthal pressure gradient.

Inner variables (e.g. friction velocity) used in these previous are obtained by classical empirical methods. However, Nagib & Chauhan (2008) show that the von Kármán constant, κ, which is one of overlap coefficients for the logarithmic law in the turbulent boundary layer is no longer constant, but that it can change depending not only on Reynolds number but also on the flow systems (e.g. boundary layers, pipes and channels). To evaluate accurately the turbulent statistics normalized by the inner variables, measurement of these inner variables is required for the turbulent boundary layer on a rotating disk.

2.3. The application examples for a rotating-disk flow

The investigation of rotating-disk flow is useful not only for understanding crossflow instability as a fundamental element of three dimensional boundary layers but also for industrial flow applications with rotating configurations. Flows driven by rotating disks have constituted a major field of study in fluid mechanics since the twentieth century. The rotating-disk flow in this study is purely driven by a single rotating disk, however in more applied studies several geometrical configurations and flow conditions are taken into account.

Chemical vapour deposition (CVD) reactors often used in the semiconductor industry to deposite thin films of electrical and optical materials on substrates are one of the applications of the rotating-disk flow, see Hussain *et al.* (2011); Chen, K. Mortazavi (1986); Vanka *et al.* (2004). In the CVD reactor a disk-like rotor is mounted horizontally in the flow. A substrate placed on the disk-like supporter rotates to generate the homogeneous axial flow over the substrate to ged rid of any non-uniformity of the incident flow (Hussain *et al.* 2011). Then the flow containing the reactive molecules attaches to the substrate and homogeneous thin film is deposited. Hussain *et al.* (2011) investigated the instability of the boundary layer over a rotating disk in an enforced axial flow to model the flow situation inside CVD reactors. They found the relative importance of the type II modes increases with axial flow.

The flow between rotating disks enclosed by a stationary sidewall has similar geometry to rotor-stator configurations, and is therefore geometry that is related to many industrial applications. The review paper about stability, transition and turbulence in rotating cavities written by Arco *et al.* (2005) describes this flow well showing that the flow instabilities with this configuration are strongly dependent on the aspect ratio of a diameter of the disk and height between two disks.

2.4. Convective instability and absolute instability

The concept of convective and absolute instability was introduced in the study of plasma physics by Briggs (1964).

Convective and absolute instability both relate to growth of disturbances in space and time and are distinguished by the different linear impulse response given at a certain spatial location. Figure 2.4 shows a sketch of impulse responses at nondimensional time $t = t_1$ for different instability conditions, where the linear impulse is introduced at a nondimensional position $x_s = 0$ and at $t = 0$. Figure 2.4(a) shows a stable condition; the introduced impulce decays in time and at $t = t_1$ the sytem reverts back to the initial condition. Figure 2.4(b) shows the behaviour of the linear impulse in a convective unstable region; the introduced impulse is exponentially amplified within the chain lines as the resulting wavepacket convects downstream. At infinite time the system reverts back to the initial condition at the location where initial impulse was introduced. Figure 2.4(c) shows the response in an absolutely unstable region; the introduced impulse is exponentially amplified within the chain lines at the introduced location. At a infinite time the system has a growing response at the location where the initial impulse was introduced.

These differences between convective instability and absolute instability shown in figure 2.4 can also be described mathmatically. A general dispersion relation is given (Schmid & Henningson 2001) as

$$D(\alpha, \omega; R) = 0, \tag{2.19}$$

where α is the wave number of the streamwise direction and ω is the frequency, and both are in general complex for the necessary spatio-temporal analysis R is the control parameter, namely Reynolds number here. Combining equation (2.19) with fluctuations $v(x, t)$ into the linear system satisfies the following condition:

$$D\left(-i\frac{\partial}{\partial x}, i\frac{\partial}{\partial x}\right) v(x, t) = 0, \tag{2.20}$$

where x is the streamwise position, $i = \sqrt{-1}$ is the imaginary unit. To investigate the response to a linear impulse into the linear system, the Green's function $G(x, t)$ is introduced into equation (2.20) with the linear impulse introduced as a Kronecker delta functions $\delta(x)\delta(t)$ so that equation (2.20) satisfies

$$D\left(-i\frac{\partial}{\partial x}, i\frac{\partial}{\partial x}\right) G(x, t) = \delta(x)\delta(t). \tag{2.21}$$

Then the response $G(x, t)$ to the linear impulse $\delta(x)\delta(t)$ is defined as follows

to distinguish between linearly stable and linearly unstable and between convectively unstable and absolutely unstable responses. The system is linearly stable if

$$\lim_{t\to\infty} G(x,t) = 0 \qquad \text{along all rays} \quad \frac{x}{t} = \text{constant}. \tag{2.22}$$

On the otherhand, the system is linearly unstable if

$$\lim_{t\to\infty} G(x,t) \to \infty \qquad \text{along at least one ray} \quad \frac{x}{t} = \text{constant}. \tag{2.23}$$

If the system is linearly unstable, the convective instability and absolute instability are distinguished mathematically as follows. The system is convectively unstable if

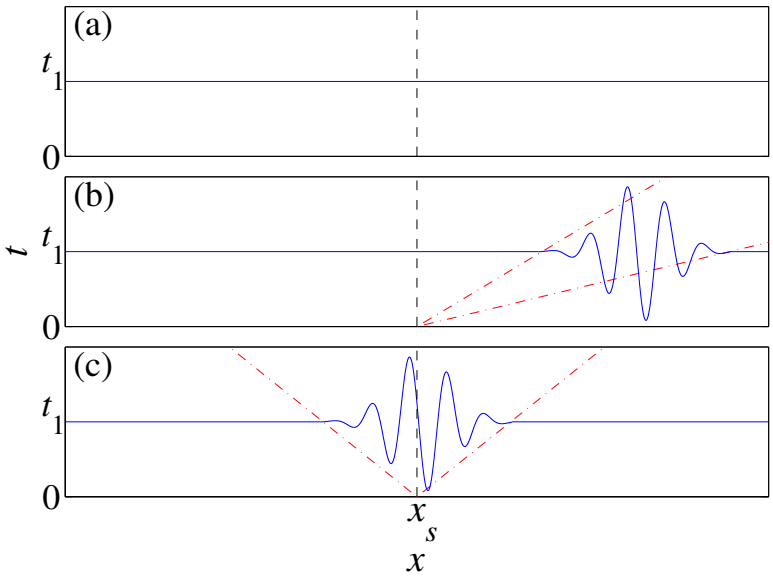

FIGURE 2.4. The concept of a linear impulse response to distinguish between convective and absolute instability in the $x-t$ plane: (a) stable, (b) convectively unstable, (c) absolutely unstable. The linear impulse is introduced at $x = x_s$ at $t = 0$ for all cases.

$$\lim_{t\to\infty} G(x,t) = 0 \qquad \text{along the ray} \quad \frac{x}{t} = 0. \tag{2.24}$$

The system is absolutely unstable if

$$\lim_{t\to\infty} G(x,t) \to \infty \qquad \text{along the ray} \quad \frac{x}{t} = 0. \tag{2.25}$$

These definitions are compatible with the sketches of the growth of the impulse in time and space shown in figure 2.4.

CHAPTER 3

Experimental methods

3.1. Experimental set-up of rotating-disk system

In this chapter, first of all, the experimental apparatus used in this study is described in some detail. Secondly, the measurement procedure of the fluid velocity by hot-wire anemometry is introduced and the typical calibration result is shown. Thirdly the measurement procedures of other relevant quantities are explained.

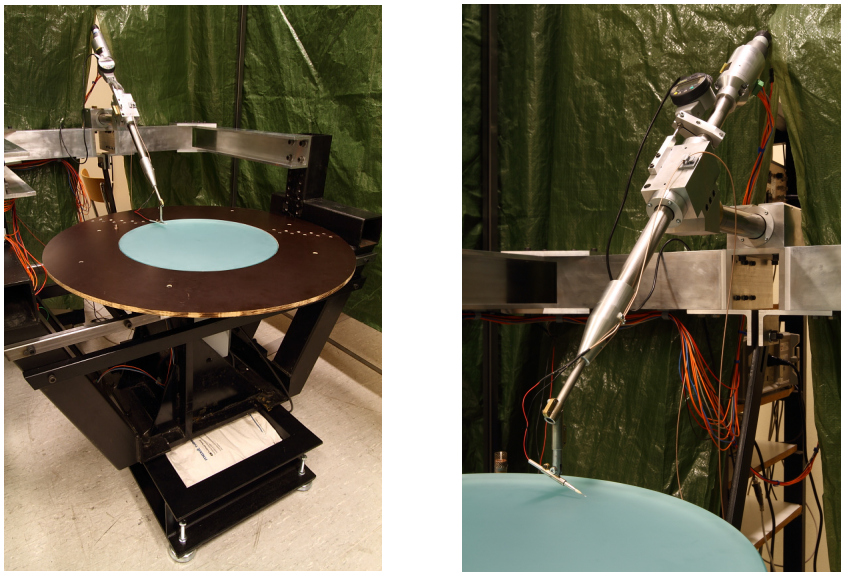

(a) (b)

FIGURE 3.1. (a) The experimental set-up of the rotating disk with plate edge condition. (b) The horizontal and inclined traverses and mounted hot-wire over the disk with open edge condition.

3.1.1. *Rotating apparatus*

The rotating disk experimental set-up is a modified version of the one used by Lingwood (1996), see figure 3.1. In the present study a float glass is selected as a surface material of the rotating disk. The detail of the glass disk is stated in the following section. The glass disk is connected to the aluminum alloy disk constricted by 8 aluminum components. The iron disk with diameter of 270 mm is an adaptor to connect between alluminum alloy disk and a vertical shaft which is mounted vertically on a shaft driven by a d.c. servo-motor (Mavilor MS6). The d.c. servo-motor to operate the rotating disk is controlled by a main motor control inverter (Infranor SMVE 1510). These components of the rotating objects are sustained by an air-bearing spindle operated by pressurized air with 5.5 bar supplied by an air compressor through an air filter (HPC, DomnickHunter AO-0013G) and air dryer (KAESER KMM3 Compressed Air Dryer). Then this air bearing makes the operation with lower acoustic noise and vibration possible to the rotating system compared with a ball bearing. This system helps to bring in low initial noise environment into flow which is baisically refered to an instability measurement. The rotating system is supported by a basement box made of steel that is filled with sandbags. The total weight of the system is approx 250 kg.

3.1.2. *Glass disk*

Lingwood (1996) used an aluminum alloy disk that was polished by a single-crystal diamond cutting tool as a surface of the rotating system. However the new float glass plate polished to get near optical quality is prepared for this experimental work instead of the aluminum alloy disk and it has an advantage that it is harder to make scratches on the surface than for metal materials. This selection is also proper in hot-wire anemometry point of view to limit heat conduction effect close to the disk wall that the surface absorbs the heat of hot-wire and the higher velocity speed than actual value is observed. The diameter of the glass disk D^* is 474 mm to mount on the preveious used alluminuim alloy disk which has same diameter. At the edge of the disk the glass disk is ground down approximately 1.5 mm with a 45° angle. This is why the actual radius of this glass is $r_d^* = 233.5$ mm. The thickness of the glass is 24 mm.

The glass disk is required to have an as small imbalance and roughness as possible to avoid the possibility that enough large initial disturbance excited by them causes the bypass transition before the appearance of the absolute instability, namely the flow changes to turbulence in the completry convective route. Then the surface of the glass disk used in this study is polished and the imbalance measurement by mechanical test indicator is shown in figure 3.2. The figure 3.2 shows the azimuthal imbalance variation and the radial imbalance variation is neglected because it is hard to measure by the mechanical test

indicator. The maximum imbalance is observed at the edge of the disk and it is maximum 10 μm. The typical surface roughness is less than 1 μm.

To avoid the break of the glass disk during the operation, the maximum operation rotational speed is estimated by the following procedure. The relation between the failure stress σ_f^* and the maximum angular velocity, Ω_{max}^*, of the rotating disk (Ashby 2005; Lingwood 1995*b*) is given as

$$\frac{D^*}{2}\Omega_{max}^* = \left(\frac{8\sigma_f^*}{S_f \rho_{glass}^* (3+\nu_{Po})}\right)^{1/2}, \tag{3.1}$$

where ν_{Po} is Poisson's ratio, which has an approximately constant value of $1/3$ for all solids and S_f is an appropriate safety factor so that $S_f = 10$ is selected in this study. As the result, the maximum rotational speed of the glass disk is given using parameters in table. 1 as $\Omega_{max}^* = 2553$ rpm.

3.1.3. *Edge conditions*

To investigate the effect on the transition process caused by the disk edge condition, different conditions have been considered. Figure 3.3 shows the three

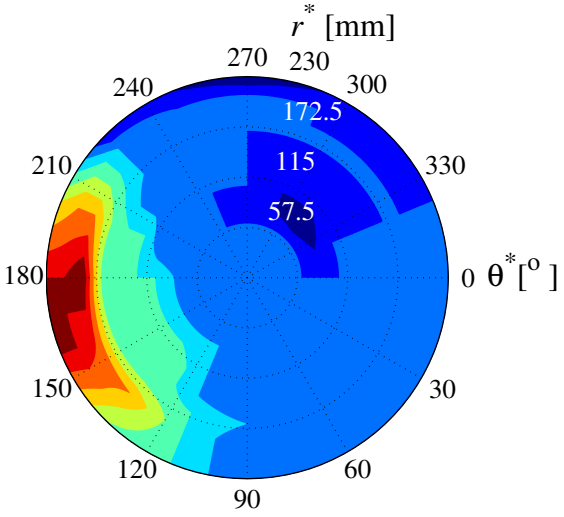

FIGURE 3.2. The azimuthal imbalance measured by a mechanical test indicator up to $r^* = 230$ mm. The colour contour indicates the surface height variation ΔI from the reference position (-2 μm (Blue) $< \Delta I <$ +7 μm (Red)) with 1 μm step.

σ_f^* [MPa]	ν_{Po}	ρ_{glass}^* [kg/m^3]
41	0.23	2.53×10^3

TABLE 1. Float glass parameters, where σ_f^* is the failure stress, ν_{Po} is the Poisson's ratio and ρ_{glass}^* is the density of the glass (*Source: http://www.industrialglasstech.com/pdf/soda limeproperties.pdf*).

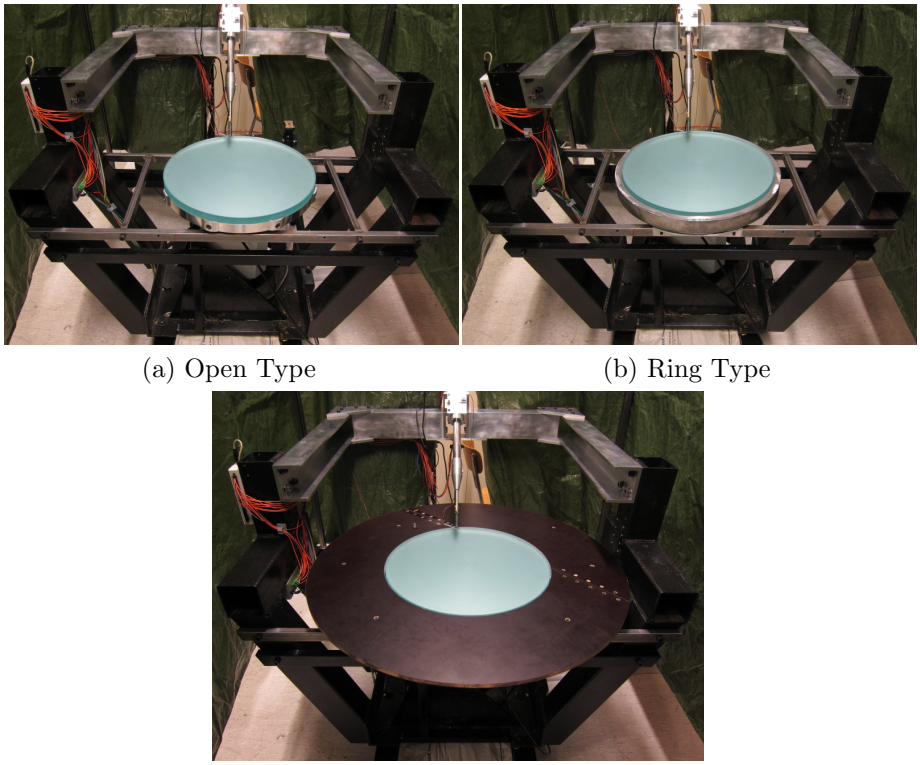

(a) Open Type (b) Ring Type

(c) Plate Type

FIGURE 3.3. Three edge conditions.

edge conditions. Figure 3.3(a) shows the 'open type', which has no extended plate or cover, figure 3.3(b) shows the 'ring type', where there is a steel ring mounted below the surface of the disk covering eight aluminum clamps fixing the glass disk to the aluminum-alloy disk. These components on the vertical edge of the glass disk generate a disturbances field with eight oscillations per

rotation of the disk as measured in the laboratory frame of reference. The ring is mounted around them to eliminate their contribution to the flow disturbance field. The ring itself does not rotate and the horizontal gap between the ring and glass disk is less than 1 mm. The edge of the glass disk is still exposed in a similar way to the open-type edge condition because the top of the ring is located 11 mm vertically below the disk surface. The third case, figure 3.3(c) is called 'plate type', which consists of a non-rotational extended annular plate made of wood with an outside diameter of 900 mm mounted around the glass disk. This extended plate eliminates the effects of the eight aluminum fixing components and also reduces the effects of noise coming from the air bearing and DC-servo motor. The horizontal gap between the disk and plate is less than 1 mm and vertically the disk surface and plate are approximately flush. These differences of the edge conditions to the laminar-turbulent transition process on the rotating-disk flow are discussed in paper 2.

3.1.4. *Traverse system*

A traverse system with two axes is connected to a basement steel box through aluminum and steel beams (see figure 3.1(a)). One of the traverse moves in the horizontal (radial) direction, and the other traverse is mounted on the horizontal traverse at a 45° inclination not to disturb the axial flow which approaches the rotating-disk from above. The horizontal traverse and inclined traverse are operated by absolute encorders (AVAGO AEAS-7000 and Mitsutoyo ID-C125B) and d.c. motors (micro motors E192.24.67 and RH158 510:1), respectively. These traverses archieved resolution of 5 μm for horizontal traverse and 3 μm for inclined traverse, respectively. They can operate all the way to the radius of the glass disk for the horizontal direction and beyond the boundary layer thickness of the rotating-disk flow for the vertical direction. At the edge of the inclined traverse a hot-wire holder directed so that the sensor is radial oriented and hence is predominately sensitive to the azimuthal velocity component. The traverse system is operated by the computer sampling signal wtih the software of LabVIEW8.6 through a controller board (National Instruments USB-6216).

3.2. Measurement techniques

3.2.1. *Hot-wire anemometry*

A hot-wire probe operational with a constant temperature anemometer (CTA) is used to measure the fluid velocity. The advantage of hot-wire anemometry compared to the other methods (e.g. Laser Doppler Velocimetry (LDV) or Particle Image Velocimetry (PIV)) is that it can sample flow velocity at a small localised position with high temporal resolution. In the present study, hot-wire probes with a single sensor made of platinum, with a diameter of 5 μm and 1 mm (laminar-turbulent transition measurement) and 1 μm and 0.3 mm

(turbulence measurement) are prepared, respectively, which are operated by CTA system (DANTEC StreamLine) with an overheat ratio (α_R) of 0.8, where it is defined as

$$\alpha_R = \frac{R^*(T_h^*) - R^*(T_{ref}^*)}{R^*(T_{ref}^*)}, \tag{3.2}$$

where $R^*(T_h^*)$ is the resistance of the sensor at the operation temperature of T_h^* and $R^*(T_{ref}^*)$ is the resistance of the sensor at the reference ambient temperature of T_{ref}^*. The typical example of the probe used in laminar-turbulent transition measurement is shown in figure 3.4(a). The sensing element of the hot-wire is oriented in the radial direction (figure 3.4(b)), making it mainly sensitive to the azimuthal velocity. A low pass filter with 30 kHz (laminar-turbulent transition measurement) or 100 kHz turbulent measurement) is applied to the CTA circuit. The output voltage from the CTA is digitalized using a 16-bit A/D converter (National Instruments USB-6216) at a specific sampling rate and sampling time and recorded by the same computer on the software of LabVIEW8.6.

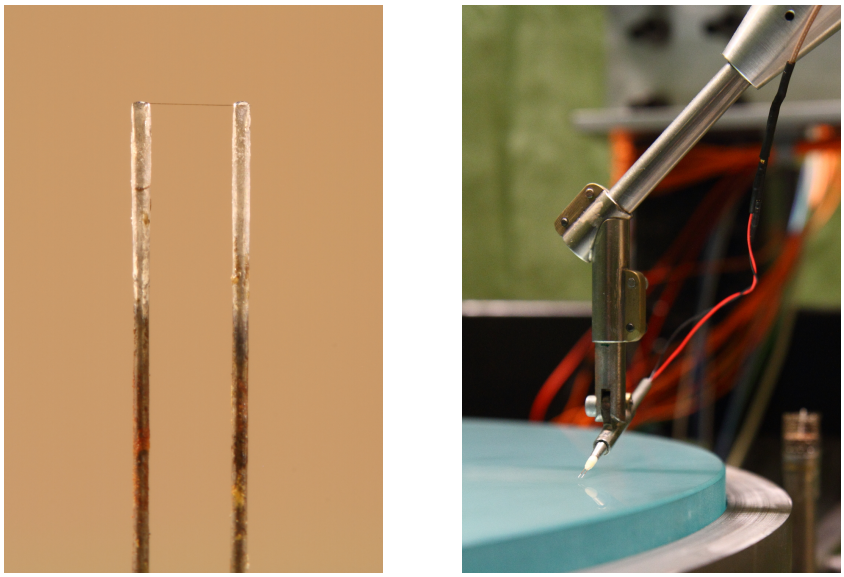

(a) (b)

FIGURE 3.4. Hot-wire setup. (a) The typical edge of the hot-wire probe used in laminar-turbulent transition measurement. (b) The hot-wire probe mounted on the traverse through an fixing adapter. The hot-wire probe is oriented to the azimuthal direction.

3.2.2. *Hot-wire calibration*

Here the hot-wire calibration method for instability and laminar-turbulent transition measurement is stated. The calibration for turbulent boundary-layer flow is discussed the detail in Paper 4.

The calibration of the hot-wire probe is generally performed in the free-stream with a reference velocity meter (e.g. Prandtl tube). However this procedure can be problem for the rotating-disk boundary layer measurement, because, first of all, the boundary layer of the rotating-disk flow does not have a free-stream region. Therefore another calibration method is performed for this study which is comparing the laminar velocity profile. This calibration requires the absolute wall-normal position from the wall of the hot-wire sensitive area. Then the height of the hot-wire sensitive area is determined by the photograph taken with a precision gauge block with 1.000 mm thickness. The typical set-up to determine the hot-wire position is shown in figure 3.5. The reference precision gauge block is put next to the hot-wire probe. The height of the hot-wire sensitive area and the gauge block is captured from the front by a micro lens (Nikon Micro-Nikkor AF 200mm f/4 D ED) and a camera (Canon EOS 7D) through a mirror located between its optical path. A typical photograph of the wall position determination is shown in figure 3.6. In Fig 3.6 1 pixel of the image is equivalent to 2.4 μm. By this method, the probe height from the wall is determined with an accuracy of $10 - 15$ μm. This error is caused mainly by resolution of the micro lens and quality of the mirror in the path which makes the image blur.

In hot-wire anemometry CTA outputs in principle the correct voltage related to fluid velocity if the physical properties of flow field are constant during the operation. However the measurements in this study observed maximum 1 °C temperature deviation basically depending on a rotational speed of a d.c. servo-motor. To compensate this temperature variance in hot-wire anemometry the output voltage is corrected by the following equation (e.g. Bruun 1995):

$$E^{*2}\left(T^*_{ref}\right) = E^{*2}\left(T^*\right)\left(1 - \frac{T^* - T^*_{ref}}{\alpha_R/\alpha_{el}}\right)^{-1}, \tag{3.3}$$

where $E^*(T^*_{ref})$ is a corrected output voltage from CTA, T^*_{ref} is a reference ambient temperature, namely an ambient temperature in hot-wire calibration, $E^*(T^*)$ is the output voltage in the measurement, T^* is an ambient temperature in the measurement and α_{el} is temperature coeficient of resistivity, which is $\alpha_{el} = 0.0038\ K^{-1}$ for platinum (Bruun 1995).

The hot-wire calibration is performed using a azimuthal laminar velocity profile by varying rotational speed, radial position and axial height. Figure 3.7 shows typical calibration results with laminar velocity profile. The calibrated

FIGURE 3.5. The typical hot-wire calibration set-up. The hot-wire sensitive area with a precision gauge block put next to the hot-wire probe is captured by a digital camera with a micro lens through the mirror put in the optical path.

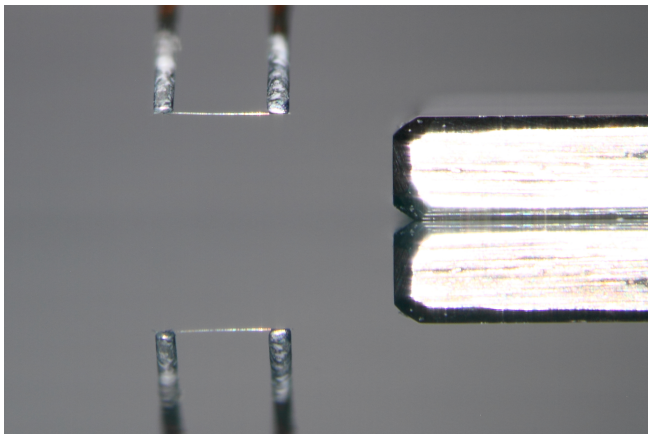

FIGURE 3.6. Photograph showing the hot-wire probe for an instability measurement during the wall position determination using a precision gauge block with 1.000 mm thickness. The above half-plane shows the real objects and the objects below half-plane are due to reflections on the glass surface.

data points are fitted by modified King's law (for better accuracy at low velocities, see Johansson & Alfredsson 1982) given as

$$V^* = k_1(E^{*2} - E_0^{*2})^{1/n} + k_2 E^* - E_0^{*1/2}, \tag{3.4}$$

where E^* and E_0^* are the mean anemometer output voltages at mean velocities V^* and zero, respectively, and $k_{1,2}$ and n are constants to be determined by a linear least-squares fit of the calibration data. Figure 3.8 shows the deviation of the calibration data points from the fitted equation (3.4). The deviations are within ± 1.5 % except at low speed region ($V^* \leqq 0.5$ m/sec). The effect of a radial velocity component on the hot-wire reading depends on the rotational speed and axial position, see figure 2.3. However figure 3.8 shows that its effect is negligible because the deviations of calibration data points from theoretical laminar profile in different rotational speeds are small. The axial velocity component is also negligible.

3.2.3. *Rotational speed of disk*

The rotational speed of the disk Ω^* is measured by photo-micro sensor (EE-SX 498). A brass disk with 30 slits at regular intervals in the azimuthal direction is mounted below the iron disk. The slits of the brass disk is sandwiched by the photo-micro sensor, then the sensor outputs the corresponding voltage (4 or 0 V) which depends whether the slit is located between the sensor or not. The frequency of the output voltage from the sensor is recorded with 80MHz sample clock timebase (National Instruments USB-6216) and converted to the rotational speed. This photo-micro sensor is able to measure the rotational speed up to 3000 rpm. The measured rotational speed of the disk is shown in figure 3.9. It shows that the disk rotates in steady rotational speed within ± 1.5 rpm.

3.2.4. *Ambient temperature and pressure*

The ambient temperature is measured by a platinum resistance thermometer (PT100). The accuracy of this sensor is checked by a mercury thermometer with 0.01°C resolution shown in figure 3.10. The deviations of the PT100 used in present study from the mercury thermometer is ± 0.15°C in the measurement range.

The kinematic viscosity ν^* of the fluid is given as

$$\nu^* = \frac{\mu^*}{\rho^*}, \tag{3.5}$$

where μ^* is the viscosity of fluid and ρ^* is the density. Here μ^* is calculated

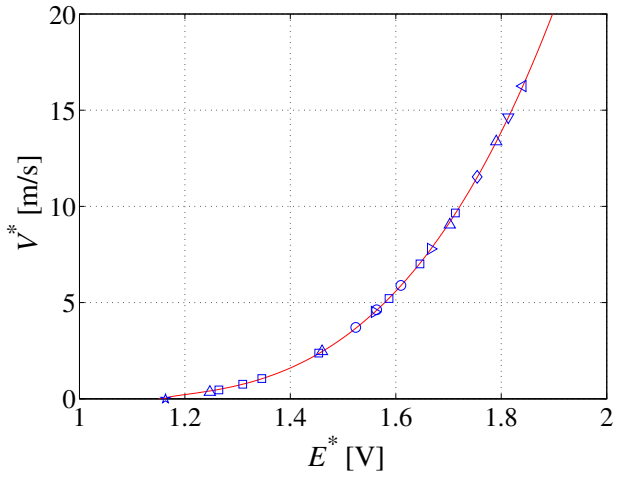

FIGURE 3.7. Hot-wire calibration using the laminar velocity profile varying the rotational speed and the normal height. The symbols indicate Ω^*=0 rpm ($\star$), 300 rpm ($\circ$), 500 rpm ($\square$), 600 rpm ($\diamond$), 700 rpm ($\triangle$), 770 rpm ($\triangledown$), 860 rpm ($\triangleleft$). The solid line shows the modified King's law fitting.

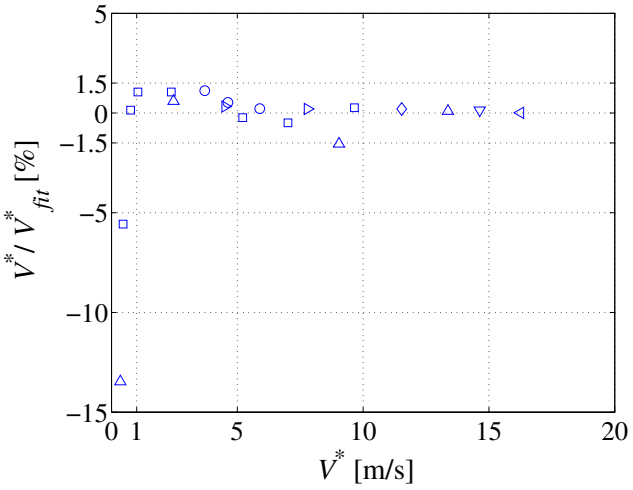

FIGURE 3.8. Deviations of calibration data points from the modified King's law fitting (V^*_{fit}). The symbols are the same as in figure 3.7.

using Sutherland law which is written as

$$\mu^* = \frac{1.4578 \times 10^{-6} \times T^{*3/2}}{T^* + 110.4}, \tag{3.6}$$

where T^* is a atmospheric temperature measured by the PT100 in Kelvin. The ρ^* for dry air is calculated using gas law which is written as

$$\rho^* = \frac{P^*_{atm}}{287.0 \times T^*}, \tag{3.7}$$

where P^*_{atm} is an atmospheric pressure in Pascal unit measured by a precision barometer.

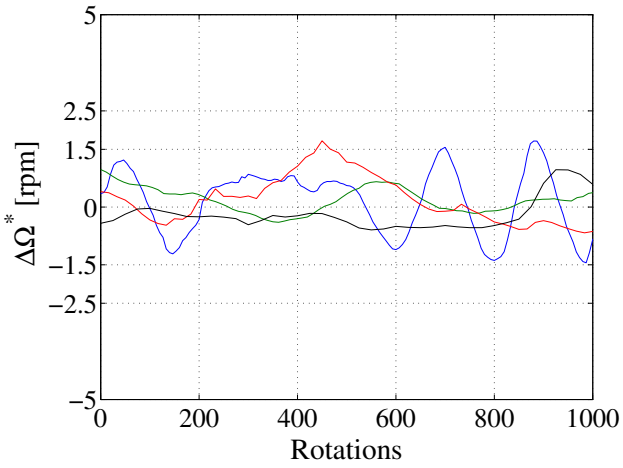

FIGURE 3.9. Deviations $\Delta\Omega^*$ rpm of the rotational speeds from the target rotational speeds in revolutions per minite. Target rotational speeds are 400 rpm (Blue), 700 rpm (Green), 1000 rpm (Red), 1500 rpm (Black), respectively.

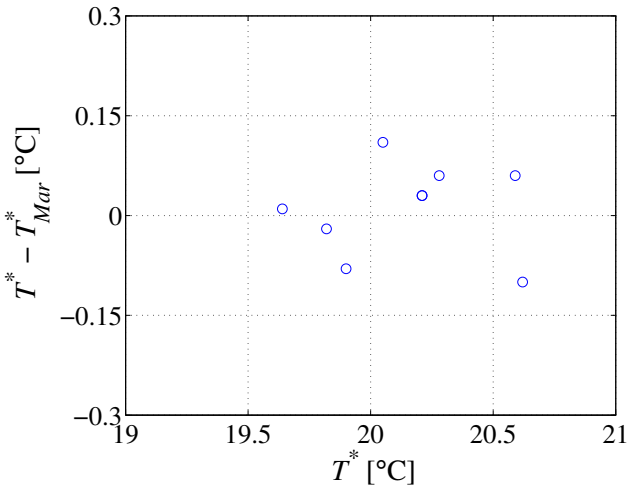

FIGURE 3.10. The temperature difference between calibrated PT100 temperature (T^*) and a precision mercury thermometer temperature (T^*_{Mar}) with 0.01°C step.

CHAPTER 4

Main contribution and conclusions

The following chapter summarizes the main contributions and conclusions from the papers constituting Part II of the thesis. For details on the results the reader is referred to the appended papers.

4.1. Laminar-turbulent transition process of the a rotating-disk boundary-layer flow.

- To investigate laminar-turbulent transition process of the rotating-disk flow azimuthal velocities are measured using a hot-wire probe which is calibrated using the laminar mean velocity profile. The measured mean azimuthal velocity profile at $R = 430 - 510$ corresponds well to its theoretical laminar profile except far away from the disk where the smallness of the azimuthal velocity makes the hot-wire measurements inaccurate. Lingwood (1995*a*) showed there is a local absolute above $R_{CA} = 507$, and suggested that this triggers nonlinearity behaviour. Then the present results show the onset of nonlinearity at $R = 510$ in the frequency spectrum as a harmonic of the primary vortices. The laminar-turbulent transition observed in the present study includes the effects not only of convective instability but also absolute instability.

- The growth of azimuthal fluctuation velocities captures its exponential growth up to $R = 580$. The slope of the exponential growth for $475 < R < 530$ corresponds approximately to the maximum spatial growth rate for stationary linear disturbances, see e.g. figure 6a in Hussain *et al.* (2011). The change in slope at around $R = 545$ could correspond to Viaud *et al.*'s so-called 'secondary front'. If so, then the present results may represent the first experimental validation of Viaud *et al.*'s (2011) DNS results and Pier's (2003) theoretical predictions of absolute instability of the primary global instability.

- To give a better understanding of the laminar-transition on the rotating-disk flow, probability density function (PDF) maps of azimuthal fluctuation velocity normalized by the local disk speed are presented. The PDF map measured at $z = 1.3$ over a range of Reynolds nubers dramatically

shows the change in distribution at $R = 550$ from exponential growth to a strongly skewed distribution. This change in PDF corresponds to the change of the slope of the disturbances growth. At around $R = 600$, the skewed PDF starts to disappear and the positive deviation of v has its maximum. The almost symmetric PDF above $R = 650$ indicates that the flow has reached a fully-developed turbulent state. These characteristics are not obvious in the spectral distributions.

- The application of PDF maps to velocity-profile measurements reveals the structure normal to the wall. In particular, at $R = 570$ peaks in the PDF may be associated with a secondary instability.

- Effects that the edge of the disk may have on laminar-turbulent transition have been investigated. Healey (2010) suggested, using the linearized complex Ginzburg-Landau equation, that the transition Reynolds number for the rotating-disk flow can be affected by the Reynolds number at the edge of the disk. He compared his suggestion with previous experimental results, which seemed to confirm his hypothesis. In this study three different edge conditions are considered and the results do not show such a behaviour in the measurement range; the differences in transition Reynolds numbers stated by previous authors are explained by the different definitions of the transition Reynolds number used in each case, rather than the effect of the edge Reynolds number (or edge condition).

- The secondary instability and turbulent breakdown of the rotating-disk flow are investigated using hot-wire anemometry. The kinked azimuthal velocity fluctuations associated with secondary instability are observed in single-realization timeseries at the final stage of the laminar-turbulent transition. It is found that the appearance of kinked timeseries becomes less apparent at certain wall-normal heights. On the other hand, ensemble-averaged fluctuation-velocity timeseries do not seem to feature kinks, indicating that the secondary instability is a travelling wave.

- The turbulent breakdown of the stationary mode has been investigated as a function of Reynolds number. It is found that the exponential growth shown by ensemble-averaged velocity fluctuations saturates at $R = 550$, plateaus for $R = 580 - 585$, and is followed by the turbulent breakdown of the stationary mode beyond that Reynolds number. To investigate more details of the stationary mode, normalized peak amplitudes of each stationary vortex are plotted as a function of Reynolds number. Each stationary vortex grows exponentially but with different amplitudes up to $R = 550$, showing a convective behaviour. However

the turbulent breakdown of each stationary vortex seems to be independent of its amplitude, which suggests that the turbulent breakdown process is not due to its convective behaviour but due to the appearance of the travelling secondary instability observed at $R = 570$.

- Based on the almost constant transition Reynolds number reported in the literature, the amplitude independence of turbulent breakdown of stationary vortex and the appearance of the travelling secondary instability at the final stage of the laminar-turbulent transition, we hypothesise that the secondary instability could be triggered by the primary absolute instability (Lingwood 1995*a*) and could be absolute unstable itself as suggested by Pier (2003).

4.2. Turbulent boundary-layer flow on a rotating disk.

- The turbulent boundary layer on the rotating disk has been studied and compared with two-dimensional flat-plate turbulent boundary layer with resopect to the mean-flow distributions as well as the higher moments.

- A methodology to determine the wall shear stress was developed, including a new idea to calibrate the hot-wire sensor against the laminar profile and extrapolating to higher velocities, a procedure that could be tested *a posteriori*.

- The results show that the statistics in the near-wall region are similar to the two-dimensional boundary layer, whereas the outer regions differ.

- The spectral map of the streamwise/azimuthal velocity show clear differences between the two cases, possibly because of the three-dimensional character of the rotating-disk boundary layer, which may change the inclination of the near wall structures with respect to the hot wire.

CHAPTER 5

Papers and authors' contributions

Paper 1

A new way to describe the transition characteristics of a rotating-disk boundary-layer flow
Shintaro Imayama (SI), P. Henrik Alfredsson (HAL) & R. J. Lingwood (RL).
Phys. Fluids **24**, 031701.

The laminar-turbulent transition of the rotating-disk flow has been investigated. The original apparatus was borrowed from the University of Cambridge Department of Engineering and was modified and put into operation by SI. The experimental investigations were performed by SI under the supervision of HAL and RL, and the writing was jointly done by SI, HAL and RL. Part of these results have been presented at EUROMECH Colloquium 525 Instabilities and transition in three-dimensional flows with rotation, 21 – 23 June 2011, Lyon, France.

Paper 2

An experimental study of edge effects on rotating-disk transition
Shintaro Imayama (SI), P. Henrik Alfredsson (HAL) & R. J. Lingwood (RL).

The effects of the finite radius of the disk on the laminar-turbulent transition of the rotating-disk flow have been investigated experimentally. The experimental investigations were performed by SI using the same facility used in Paper 1 under supervision of HAL and RL, and the writing was jointly done by SI, HAL and RL. Some of these results have been prese nted at the Annual Meeting of the American Physical Society's Division of Fluid Dynamics, 20 – 22 November 2011, Baltimore, Maryland, USA.

Paper 3

Secondary instability and turbulent breakdown of the rotating-disk flow
Shintaro Imayama (SI).

This paper focusses on the transition process and especially the role of secondary instability on the primary stationary vortices, through separating the stationary and travelling modes by comparison of ensemble-averaged and single-realization measurements of the fluctuating velocity.

Paper 4

An experimental study of a rotating-disk turbulent boundary-layer flow Shintaro Imayama (SI), R. J. Lingwood (RL) & P. Henrik Alfredsson (HAL).

The turbulent boundary layer on the rotating disk flow has been investigated. The azimuthal friction velocity is determined using hot-wire measurement directly and turbulence statistics normalized by the inner scales are represented. The experiments were performed by SI using the same facility used in Paper 1 under the supervision of RL and HAL, and the writing was jointly done by SI, RL and HAL. Some of these results have been presented at EUROMECH Colloquium 525 Instabilities and transition in three-dimensional flows with rotation, 21 – 23 June 2011, Lyon, France.

Acknowledgements

This research has been supported by the Swedish Research Council (VR) and Linné FLOW Centre at KTH. The main rotating apparatus is on long-term loan from the University of Cambridge Department of Engineering to KTH Mechanics. Marcus Wallenberg Laboratory for sound and vibration research (MWL) in Department of Aeronautical and Vehicle Engineering at KTH provides support through use of their flow instruments (constant temperature anemometry (CTA) and vibration sensors).

First of all I am really grateful to my main supervisor Prof. Henrik Alfredsson not only for accepting me as his graduate student but also for teaching me how a researcher should be.

Thanks also to my co-supervisor Prof. Rebecca Lingwood for discussing instabilities on a rotating-disk flow and for teaching me great knowledge of the instabilities. Ferthermore I appreciate her for teaching me how a paper should be written.

I also thank the late Dr Tim Nickels who arranged the loan of the experimental apparatus from the University of Cambridge Department of Engineering to KTH.

Many thanks to Docent Jens H. M. Fransson and Docent Fredrik Lundell for discussions about flow instabilities and teaching me.

Thanks also to Dr Ramis Örlü for always helping me and providing a lot of advice.

Many thanks to Joakim Karlström and Göran Rådberg for making and assembling the rotating-disk apparatus. Their suggestions when I have a problem with the apparatus have helped me enormously.

I wish to thank Alexander, Alexandre, Antonio, Bengt, Emma, Fredrik, Johan, Julie, Karl, Lailai, Malin, Malte, Markus, Mathias, Michail, Nils, Olle, Renzo, Shahab, Sohrab, Sissy and Tomas among others for a nice atmosphere in the office.

Finally, I appreciate my parents supporting me and permitting me to choose my own path.

References

Arco, E. D., Serre, E. & Bontoux, P. 2005 *Stability, transition and turbulence in rotating cavities*. WIT Press.

Ashby, M. F. 2005 *Materials Selection in Mechanical Design*, 3rd edn. Elsevier.

Balachandar, S., Streett, C. L. & Malik, M. R. 1992 Secondary instability in rotating-disk flow. *J. Fluid Mech.* **242**, 323–347.

Brady, J. 1987 On rotating disk flow. *J. Fluid Mech.* **175**, 363–394.

Briggs, R. 1964 *Electron-stream interaction with plasmas*. MIT Press.

Bruun, H. 1995 *Hot-wire anemometry Principles and signal analysis*. New York, USA: Oxford University Press Inc.

Cham, T.-S. & Head, M. R. 1969 Turbulent boundary-layer flow on a rotating disk. *J. Fluid Mech.* **37**, 129–147.

Chen, K. Mortazavi, A. R. 1986 An analytical study of the Chemical Vapor Deposition (CVD) processes in a rotating pedestal reactor. *J. Cryst. Growth* **77**, 199–208.

Chin, D.-T. & Litt, M. 1972 An electrochemical study of flow instability on a rotating disk. *J. Fluid Mech.* **54**, 613–625.

Clarkson, M. H., Chin, S. C. & Shacter, P. 1980 Flow visualization of inflexional instabilities on a rotating disk. *AIAA Paper* 80–0279.

Clauser, F. H. 1954 Turbulent boundary layers in adverse pressure gradients. *AIAA J.* **21**, 91–108.

Cobb, E. C. & Saunders, O. A. 1956 Heat transfer from a rotating disk. *P. Roy. Soc. Lond. A. Mat.* **236**, 343–351.

Davies, C. & Carpenter, P. W. 2003 Global behaviour corresponding to the absolute instability of the rotating-disc boundary layer. *J. Fluid Mech.* **486**, 287–329.

Erian, F. & Tong, Y. 1971 Turbulent Flow Due to a Rotating Disk. *Phys. Fluids* **14**, 2588–2591.

Fedorov, B., Plavnik, G., Prokhorov, I. & Zhukhovitskii, L. 1976 Transitional flow conditions on a rotating disk. *J. Eng. Phys. Therm.* **31**, 1448–1453.

Goldstein, S. 1935 On the resistance to the rotation of a disc immersed in a fluid. *Proc. Camb. Phil. Soc.* **2**, 232–241.

Gregory, N., Stuart, J. & Walker, W. S. 1955 On the stability of three-dimensional boundary layers with application to the flow due to a rotating disk. *Phil. Trans. R. Soc. Lond.* **248**, 155–199.

Gregory, N. & Walker, W. S. 1960 Experiments on the effect of suction on the flow due to a rotating disk. *J. Fluid Mech.* **9**, 225–234.

Healey, J. J. 2010 Model for unstable global modes in the rotating-disk boundary layer. *J. Fluid Mech.* **663**, 148–159.

Hsu, H. P. 2002 *Vector Analysis (in Japanese language)*, 1st edn. Morikita.

Huerre, P. & Monkewitz, P. A. 1990 Local and global instabilities in spatially developing flows. *Annu. Rev. Fluid Mech.* **22**, 473–537.

Hussain, Z., Garrett, S. J. & Stephen, S. O. 2011 The instability of the boundary layer over a disk rotating in an enforced axial flow. *Phys. Fluids* **23**, 114108.

Johansson, A. V. & Alfredsson, P. H. 1982 On the structure of turbulent channel flow. *J. Fluid Mech.* **122**, 295–314.

von Kármán, T. 1921 Üuber laminare und turbulent Reibung. *Z. Angew. Math. Mech.* **1**, 233–252.

Kobayashi, R., Kohama, Y. & Takamadate, C. 1980 Spiral vortices in boundary layer transition regime on a rotating disk. *Acta Mech.* **35**, 71–82.

Kohama, Y. 1984 Study on boundary layer transition of a rotating disk. *Acta Mech.* **50**, 193–199.

Kundu, P. K. & Cohen, I. M. 2008 *Fluid Mechanics*, forth edn. Elsevier.

Lingwood, R. J. 1995*a* Absolute instability of the boundary layer on a rotating disk. *J. Fluid Mech.* **299**, 17–33.

Lingwood, R. J. 1995*b* Stability and Transition of the Boundary Layer on a Rotating Disk. Phd thesis, Cambridge Unniversity.

Lingwood, R. J. 1996 An experimental study of absolute instability of the rotating-disk boundary-layer flow. *J. Fluid Mech.* **314**, 373–405.

Lingwood, R. J. 1997*a* Absolute instability of the Ekman layer and related rotating flows. *J. Fluid Mech.* **331**, 405–428.

Lingwood, R. J. 1997*b* On the impulse response for swept boundary-layer flows. *J. Fluid Mech.* **344**, 317–334.

Littell, H. S. & Eaton, J. K. 1994 Turbulence characteristics of the boundary layer on a rotating disk. *J. Fluid Mech.* **266**, 175–207.

Mager, A. 1952 Generalisation of boundary layer momentum-integral equations to three-dimensional flows including those of rotating system. *NACA Rep. 1067* .

Malik, M. R., Wilkinson, S. P. & Orszag, S. A. 1981 Instability and transition in rotating disk flow. *AIAA J.* **19**, 1131–1138.

Nagib, H. M. & Chauhan, K. a. 2008 Variations of von Kármán coefficient in canonical flows. *Phys. Fluids* **20**, 101518.

Othman, H. & Corke, T. C. 2006 Experimental investigation of absolute instability of a rotating-disk boundary layer. *J. Fluid Mech.* **565**, 63–94.

Pier, B. 2003 Finite-amplitude crossflow vortices, secondary instability and transition in the rotating-disk boundary layer. *J. Fluid Mech.* **487**, 315–343.

Schmid, P. J. & Henningson, D. S. 2001 *Stability and Transition in Shear Flows*. New York, USA: Springer.

Smith, N. 1947 *Exploratory investigation of laminar-boundary-layer oscillations on a rotating disk*. National Advisory Committee for Aeronautics.

Theodorsen, T. & Regier, A. 1944 Experiments on drag of revolving disks, cylinders and streamline rods at high speeds. *NACA Rep. 793* .

Thompson, B. G. J. 1965 A new two-parameter family of mean velocity profiles for incompressible turbulent boundary layers on smooth walls. *Aero. Res. Coun. R. & M. 3463* .

Vanka, S., Luo, G. & Glumac, N. 2004 Parametric effects on thin film growth and uniformity in an atmospheric pressure impinging jet CVD reactor. *J. Cryst. Growth* **267**, 22–34.

Viaud, B., Serre, E. & Chomaz, J.-M. 2011 Transition to turbulence through steep global-modes cascade in an open rotating cavity. *J. Fluid Mech.* **688**, 493–506.

Wilkinson, S. P. & Malik, M. R. 1985 Stability experiments in the flow over a rotating disk. *AIAA J.* **23**, 588–595.

APPENDIX A

Derivations of governing equations

A.1. Introduction

This appendix shows the derivation in detail of the governing equations for the incompressible rotating disk flow in cylindrical coordinates (Cham & Head 1969; Hsu 2002; Kundu & Cohen 2008). First general definitions of the cylindrical coordinates, the continuity equation and Navier-Stokes equations (NSE) are derived. Secondly taking a Reynolds decomposition and ensemble average, Reynolds Averaged Navier-Stokes equation (RANS) is derived. Finally making some assumptions about the magnitude of various terms the RANS for turbulent flow on the rotating-disk is derived. The dimensional mark ' * ' used in the introduction parts and papers of this thesis is taken away in the appendix.

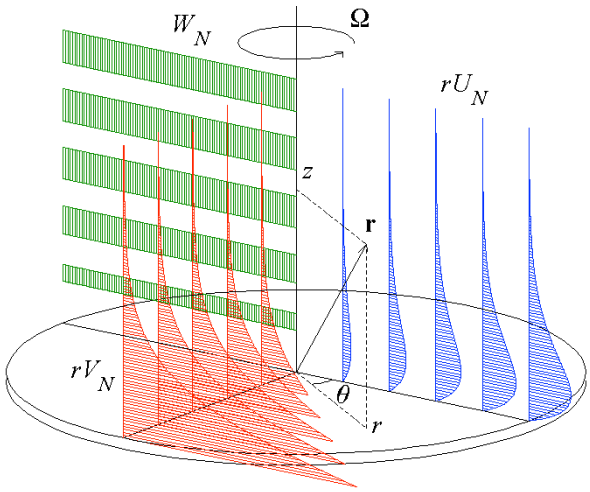

FIGURE A.1. A sketch of the von Kármán boundary layer on a rotating disk showing the mean velocity profiles (in a stationary laboratory frame), where $U_N = U/(r\Omega)$, $V_N = V/(r\Omega)$, $W_N = W/(\nu\Omega)^{1/2}$.

A.2. Cylindrical frame system in a rotating-disk flow

The system of incompressible rotating-disk flow is modeled as an infinite disk rotating at a constant speed Ω in cylindrical coordinate frame. Figure A.1 shows a sketch of the rotating-disk flow system. The position vector $\mathbf{r}$, velocity vector $\mathbf{v}$ and rotation vector $\boldsymbol{\omega}$ are given as

$$\mathbf{r} = \begin{pmatrix} r\cos\theta \\ r\sin\theta \\ z \end{pmatrix}, \tag{A.1}$$

$$\mathbf{v} = \begin{pmatrix} \tilde{u} \\ \tilde{v} \\ \tilde{w} \end{pmatrix}, \tag{A.2}$$

$$\boldsymbol{\omega} = \begin{pmatrix} 0 \\ 0 \\ \Omega \end{pmatrix}, \tag{A.3}$$

where r is the radius, θ is the angle and z is a wall normal coordinate, $\tilde{u}, \tilde{v}, \tilde{w}$ are radial, azimuthal and axial velocity components respectively, and Ω is the constant angular rotational speed of the disk.

To confirm the independence relation between the orthogonal coordinate system and the cylindrical frame system, a Jacobian matrix of positions in both coordinate systems can be written as

$$\begin{aligned} J = \frac{\partial(x,y,z)}{\partial(r,\theta,z)} &= \begin{vmatrix} \partial_r x & \partial_\theta x & \partial_z x \\ \partial_r y & \partial_\theta y & \partial_z y \\ \partial_r z & \partial_\theta z & \partial_z z \end{vmatrix} \\ &= \begin{vmatrix} \cos\theta & -r\sin\theta & 0 \\ \sin\theta & r\cos\theta & 0 \\ 0 & 0 & 1 \end{vmatrix} \\ &= r\left(\cos^2\theta + \sin^2\theta\right) = r \neq 0 \text{ (except } r = 0), \end{aligned} \tag{A.4}$$

where (x, y, z) is a position vector in the orthogonal coordinate system and $\partial_r, \partial_\theta, \partial_z$ are derivatives in the radial, azimuthal and axial directions, respectively. The relation of the position vector between the orthogonal coordinate system and the cylindrical coordinate system is written as

$$x = r\cos\theta,\ y = r\sin\theta,\ z = z. \tag{A.5}$$

The Jacobian matrix is nonzero except $r = 0$, which indicates that the positions in orthogonal coordinate system and cylindrical coordinate system have one-on-one relations except at $r = 0$.

A.3. Continuity equation

The divergence operator ∇ is in the cylindrical coordinate system written as

$$\nabla = \frac{1}{h_r h_\theta h_z} \begin{pmatrix} \partial_r(h_\theta h_z) \\ \partial_\theta(h_z h_r) \\ \partial_z(h_r h_\theta) \end{pmatrix} \tag{A.6}$$

where h_r, h_θ, h_z are given as

$$\begin{aligned} h_r &= \left|\frac{\partial \mathbf{r}}{\partial r}\right| = \left(\cos^2\theta + \sin^2\theta\right)^{1/2} = 1, \\ h_\theta &= \left|\frac{\partial \mathbf{r}}{\partial \theta}\right| = \left[(-r\sin\theta)^2 + (r\cos\theta)^2\right]^{1/2} = r, \\ h_z &= \left|\frac{\partial \mathbf{r}}{\partial z}\right| = 1. \end{aligned} \tag{A.7}$$

Then the divergence of the velocity vector is

$$\nabla \cdot \mathbf{v} = \frac{1}{r}\frac{\partial(r\tilde{u})}{\partial r} + \frac{1}{r}\frac{\partial \tilde{v}}{\partial \theta} + \frac{\partial \tilde{w}}{\partial z}. \tag{A.8}$$

The continuity equation in incompressible flow is

$$\nabla \cdot \mathbf{v} = 0. \tag{A.9}$$

Then equation (A.2) and equation (A.6) are substituted into equation (A.9), giving

$$\frac{\partial \tilde{u}}{\partial r} + \frac{1}{r}\frac{\partial \tilde{v}}{\partial \theta} + \frac{\partial \tilde{w}}{\partial z} + \frac{\tilde{u}}{r} = 0. \tag{A.10}$$

A.4. Navier-Stokes equation (NSE)

The Navier-Stokes equation (NSE) in a uniformly rotating co-ordinate system is written as

$$\underbrace{\frac{\partial \mathbf{v}}{\partial t} + (\mathbf{v}\cdot\nabla)\mathbf{v}}_{①} + \underbrace{2\boldsymbol{\omega}\times\mathbf{v}}_{②} + \underbrace{\boldsymbol{\omega}\times(\boldsymbol{\omega}\times\mathbf{r})}_{③} = \underbrace{-\frac{1}{\rho}\nabla p}_{④} + \underbrace{\nu\nabla^2\mathbf{v}}_{⑤}, \tag{A.11}$$

where ① is the material differential term, where $(\mathbf{v}\cdot\nabla)\mathbf{v}$ is defined as

$$(\mathbf{v}\cdot\nabla)\mathbf{v} = \left(\tilde{u}\frac{\partial}{\partial r} + \frac{\tilde{v}}{r}\frac{\partial}{\partial \theta} + \tilde{w}\frac{\partial}{\partial z}\right)\mathbf{v} + \frac{1}{r}\begin{pmatrix} -\tilde{v}\tilde{v} \\ \tilde{u}\tilde{v} \\ 0 \end{pmatrix}, \tag{A.12}$$

the Coriolis force term (②) is

$$2\boldsymbol{\omega} \times \mathbf{v} = 2 \begin{pmatrix} 0 \\ 0 \\ \Omega \end{pmatrix} \times \begin{pmatrix} \tilde{u} \\ \tilde{v} \\ \tilde{w} \end{pmatrix} = \begin{pmatrix} -2\tilde{v}\Omega \\ 2\tilde{u}\Omega \\ 0 \end{pmatrix}, \tag{A.13}$$

the centrifugal force term (③) is

$$\boldsymbol{\omega} \times (\boldsymbol{\omega} \times \mathbf{r}) = -\Omega^2 \begin{pmatrix} r \\ 0 \\ 0 \end{pmatrix}, \tag{A.14}$$

the pressure term (④) is

$$-\frac{1}{\rho}\nabla\tilde{p} = -\frac{1}{\rho} \begin{pmatrix} \partial_r\tilde{p} \\ (\partial_\theta\tilde{p})/r \\ \partial_z\tilde{p} \end{pmatrix}, \tag{A.15}$$

and viscous term (⑤) is

$$\nu\nabla^2\mathbf{v} = \nu \left[\begin{pmatrix} \nabla^2\tilde{u} \\ \nabla^2\tilde{v} \\ \nabla^2\tilde{w} \end{pmatrix} + \frac{1}{r^2} \begin{pmatrix} -\tilde{u} - 2\partial_\theta\tilde{v} \\ -\tilde{v} + 2\partial_\theta\tilde{u} \\ 0 \end{pmatrix} \right], \tag{A.16}$$

respectively, where ρ is a density, $\tilde{p}$ is a pressure and ν is the kinematic viscosity and the Laplace operator ∇^2 in a cylindrical coordinate system is defined as

$$\nabla^2 = \frac{\partial^2}{\partial r^2} + \frac{1}{r^2}\frac{\partial^2}{\partial\theta^2} + \frac{\partial^2}{\partial z^2} + \frac{1}{r}\frac{\partial}{\partial r}. \tag{A.17}$$

Therefore the viscous term can be written

$$\nu\nabla^2\mathbf{v} = \nu \left[\left(\frac{\partial^2}{\partial r^2} + \frac{1}{r^2}\frac{\partial^2}{\partial\theta^2} + \frac{\partial^2}{\partial z^2} \right) \begin{pmatrix} \tilde{u} \\ \tilde{v} \\ \tilde{w} \end{pmatrix} + \frac{1}{r}\frac{\partial}{\partial r} \begin{pmatrix} \tilde{u} \\ \tilde{v} \\ \tilde{w} \end{pmatrix} + \frac{1}{r^2} \begin{pmatrix} -\tilde{u} - 2\partial_\theta\tilde{v} \\ -\tilde{v} + 2\partial_\theta\tilde{u} \\ 0 \end{pmatrix} \right]. \tag{A.18}$$

Then in a cylindrical coordinate system,the three components of the Navier-Stokes equations become

Radial component:

$$\begin{aligned}&\frac{\partial \tilde{u}}{\partial t}+\left(\tilde{u}\frac{\partial \tilde{u}}{\partial r}+\frac{\tilde{v}}{r}\frac{\partial \tilde{u}}{\partial \theta}+\tilde{w}\frac{\partial \tilde{u}}{\partial z}\right)-\frac{\tilde{v}\tilde{v}}{r}-2\tilde{v}\Omega-r\Omega^2\\&=-\frac{1}{\rho}\frac{\partial \tilde{p}}{\partial r}+\nu\left[\left(\frac{\partial^2 \tilde{u}}{\partial r^2}+\frac{1}{r^2}\frac{\partial^2 \tilde{u}}{\partial \theta^2}+\frac{\partial^2 \tilde{u}}{\partial z^2}\right)+\frac{1}{r}\frac{\partial \tilde{u}}{\partial r}-\frac{\tilde{u}}{r^2}-\frac{2}{r^2}\frac{\partial \tilde{v}}{\partial \theta}\right],\end{aligned} \tag{A.19}$$

Azimuthal component:

$$\begin{aligned}&\frac{\partial \tilde{v}}{\partial t}+\left(\tilde{u}\frac{\partial \tilde{v}}{\partial r}+\frac{\tilde{v}}{r}\frac{\partial \tilde{v}}{\partial \theta}+\tilde{w}\frac{\partial \tilde{v}}{\partial z}\right)+\frac{\tilde{u}\tilde{v}}{r}+2\tilde{u}\Omega\\&=-\frac{1}{\rho r}\frac{\partial \tilde{p}}{\partial \theta}+\nu\left[\left(\frac{\partial^2 \tilde{v}}{\partial r^2}+\frac{1}{r^2}\frac{\partial^2 \tilde{v}}{\partial \theta^2}+\frac{\partial^2 \tilde{v}}{\partial z^2}\right)+\frac{1}{r}\frac{\partial \tilde{v}}{\partial r}-\frac{\tilde{v}}{r^2}+\frac{2}{r^2}\frac{\partial \tilde{u}}{\partial \theta}\right],\end{aligned} \tag{A.20}$$

Axial component:

$$\begin{aligned}&\frac{\partial \tilde{w}}{\partial t}+\left(\tilde{u}\frac{\partial \tilde{w}}{\partial r}+\frac{\tilde{v}}{r}\frac{\partial \tilde{w}}{\partial \theta}+\tilde{w}\frac{\partial \tilde{w}}{\partial z}\right)\\&=-\frac{1}{\rho}\frac{\partial \tilde{p}}{\partial z}+\nu\left[\left(\frac{\partial^2 \tilde{w}}{\partial r^2}+\frac{1}{r^2}\frac{\partial^2 \tilde{w}}{\partial \theta^2}+\frac{\partial^2 \tilde{w}}{\partial z^2}\right)+\frac{1}{r}\frac{\partial \tilde{w}}{\partial r}\right].\end{aligned} \tag{A.21}$$

A.5. Reynolds average

In this section the Reynolds averaged continuity equation and Navier-Stokes equations (RANS) are derived, respectively. The instantaneous velocity $(\tilde{u}, \tilde{v}, \tilde{w})$ and instantaneous pressure $(\tilde{p})$ are decomposed in their mean and fluctuations (time-dependence), through an operation called Reynolds decomposition, giving

$$\begin{aligned}\tilde{u}&=U+u,\\\tilde{v}&=V+v,\\\tilde{w}&=W+w,\\\tilde{p}&=P+p,\end{aligned} \tag{A.22}$$

where U, V, W, P are mean components of the radial, azimuthal and axial velocities and pressure, and u, v, w, p are fluctuation components of radial, azimuthal and axial velocities and pressure, respectively.

A.5.1. *Reynolds averaged continuity equation*

The continuity equation is given from equation (A.10) as

$$\frac{\partial \tilde{u}}{\partial r} + \frac{1}{r}\frac{\partial \tilde{v}}{\partial \theta} + \frac{\partial \tilde{w}}{\partial z} + \frac{\tilde{u}}{r} = 0. \tag{A.23}$$

The decomposed components (equation (A.22)) are substituted into equation (A.23), whereafter an ensemble averages is taken here (denoted with an overscore), resulting in

$$\overline{\frac{\partial U}{\partial r}} + \cancel{\overline{\frac{1}{r}\frac{\partial u}{\partial r}}} + \cancel{\overline{\frac{1}{r}\frac{\partial V}{\partial \theta}}} + \cancel{\overline{\frac{1}{r}\frac{\partial v}{\partial \theta}}} + \overline{\frac{\partial W}{\partial z}} + \cancel{\overline{\frac{\partial w}{\partial z}}} + \overline{\frac{U}{r}} + \cancel{\overline{\frac{u}{r}}} = 0. \tag{A.24}$$

The derivation with respect to the θ direction is neglected due to that the mean flow is independent of the azimuthal direction. Therefore, the Reynolds averaged continuity equation becomes

$$\frac{\partial U}{\partial r} + \frac{\partial W}{\partial z} + \frac{U}{r} = 0. \tag{A.25}$$

A.5.2. *The radial component of the RANS*

The radial component of NSE the is given by equation (A.19) and decomposed components (equation (A.22)) are substituted into equation (A.19). Then the left-hand side (LHS) of equation (A.19) becomes

$$\begin{aligned}
\text{LHS(A.19)} = \overline{\frac{\partial U}{\partial t}} + \cancel{\overline{\frac{\partial u}{\partial t}}} + \overline{U\frac{\partial U}{\partial r}} + \cancel{\overline{u\frac{\partial U}{\partial r}}} + \cancel{\overline{U\frac{\partial u}{\partial r}}} + \overline{u\frac{\partial u}{\partial r}} \\
+ \overline{\frac{V}{r}\frac{\partial U}{\partial \theta}} + \cancel{\overline{\frac{v}{r}\frac{\partial U}{\partial \theta}}} + \cancel{\overline{\frac{V}{r}\frac{\partial u}{\partial \theta}}} + \overline{\frac{v}{r}\frac{\partial u}{\partial \theta}} \\
+ \overline{W\frac{\partial U}{\partial z}} + \cancel{\overline{w\frac{\partial U}{\partial z}}} + \cancel{\overline{W\frac{\partial u}{\partial z}}} + \overline{w\frac{\partial u}{\partial z}} \\
- \overline{\frac{V^2}{r}} - \cancel{2\overline{\frac{Vv}{r}}} - \overline{\frac{vv}{r}} - \overline{2V\Omega} - \cancel{\overline{2v\Omega}} - \overline{r\Omega^2} \\
= \frac{\partial U}{\partial t} + U\frac{\partial U}{\partial r} + \frac{V}{r}\frac{\partial U}{\partial r} + W\frac{\partial U}{\partial z} + \underbrace{\overline{u\frac{\partial u}{\partial r}} + \overline{\frac{v}{r}\frac{\partial u}{\partial \theta}} + \overline{w\frac{\partial u}{\partial z}}}_{A_r} \\
- \frac{V^2}{r} - \frac{\overline{vv}}{r} - 2V\Omega - r\Omega^2,
\end{aligned} \tag{A.26}$$

where A_r is

$$
\begin{aligned}
A_r &= \overline{\frac{\partial uu}{\partial r}} - \overline{u\frac{\partial u}{\partial r}} + \overline{\frac{1}{r}\frac{\partial uv}{\partial \theta}} - \overline{\frac{u}{r}\frac{\partial v}{\partial \theta}} + \overline{\frac{\partial uw}{\partial z}} - \overline{u\frac{\partial w}{\partial z}} \\
&= \overline{\frac{\partial uu}{\partial r}} + \overline{\frac{1}{r}\frac{\partial uv}{\partial \theta}} + \overline{\frac{\partial uw}{\partial z}} - \overline{u\underbrace{\left(\frac{\partial u}{\partial r} + \frac{1}{r}\frac{\partial v}{\partial \theta} + \frac{\partial w}{\partial z}\right)}_{=-u/r}} \\
&= \frac{\partial \overline{uu}}{\partial r} + \frac{1}{r}\frac{\partial \overline{uv}}{\partial \theta} + \frac{\partial \overline{uw}}{\partial z} + \frac{\overline{uu}}{r}.
\end{aligned}
\tag{A.27}
$$

The right-hand side (RHS) of equation (A.19) becomes

$$
\begin{aligned}
\mathrm{RHS(A.19)} = &-\overline{\frac{1}{\rho}\frac{\partial P}{\partial r}} - \cancel{\overline{\frac{1}{\rho}\frac{\partial p}{\partial r}}} + \nu\Bigg[\overline{\frac{\partial^2 U}{\partial r^2}} + \cancel{\overline{\frac{\partial^2 u}{\partial r^2}}} + \overline{\frac{1}{r^2}\frac{\partial^2 U}{\partial \theta^2}} + \cancel{\overline{\frac{1}{r^2}\frac{\partial^2 u}{\partial \theta^2}}} \\
&+ \overline{\frac{\partial^2 U}{\partial z^2}} + \cancel{\overline{\frac{\partial^2 u}{\partial z^2}}} + \overline{\frac{1}{r}\frac{\partial U}{\partial r}} + \cancel{\overline{\frac{1}{r}\frac{\partial u}{\partial r}}} - \overline{\frac{U}{r^2}} - \cancel{\overline{\frac{u}{r^2}}} - \overline{\frac{2}{r^2}\frac{\partial V}{\partial \theta}} - \cancel{\overline{\frac{2}{r^2}\frac{\partial v}{\partial \theta}}}\Bigg] \\
= &-\frac{1}{\rho}\frac{\partial P}{\partial r} + \nu\left[\frac{\partial^2 U}{\partial r^2} + \frac{1}{r^2}\frac{\partial^2 U}{\partial \theta^2} + \frac{\partial^2 U}{\partial z^2} + \frac{1}{r}\frac{\partial U}{\partial r} - \frac{U}{r^2} - \frac{2}{r^2}\frac{\partial V}{\partial \theta}\right].
\end{aligned}
\tag{A.28}
$$

Then the RANS of the radial component is given as

$$
\begin{aligned}
&\frac{\partial U}{\partial t} + U\frac{\partial U}{\partial r} + \frac{V}{r}\frac{\partial U}{\partial \theta} + W\frac{\partial U}{\partial z} + \frac{\partial \overline{uu}}{\partial r} + \frac{1}{r}\frac{\partial \overline{uv}}{\partial \theta} + \frac{\partial \overline{uw}}{\partial z} \\
&\qquad + \frac{\overline{uu}}{r} - \frac{V^2}{r} - \frac{\overline{vv}}{r} - 2V\Omega - r\Omega^2 \\
&= -\frac{1}{\rho}\frac{\partial P}{\partial r} + \nu\left[\frac{\partial^2 U}{\partial r^2} + \frac{1}{r^2}\frac{\partial^2 U}{\partial \theta^2} + \frac{\partial^2 U}{\partial z^2} + \frac{1}{r}\frac{\partial U}{\partial r} - \frac{U}{r^2} - \frac{2}{r^2}\frac{\partial V}{\partial \theta}\right].
\end{aligned}
\tag{A.29}
$$

A.5.3. *The azimuthal component of the RANS*

The azimuthal component of the NSE is given from equation (A.20) and decomposed components from equation (A.22) are substituted into equation (A.20). Then the LHS of equation (A.20) becomes

$$
\begin{aligned}
\text{LHS(A.20)} = \overline{\frac{\partial V}{\partial t}} + \cancel{\overline{\frac{\partial p}{\partial t}}} + \overline{U\frac{\partial V}{\partial r}} + \cancel{\overline{u\frac{\partial V}{\partial r}}} + \cancel{\overline{U\frac{\partial v}{\partial r}}} + \overline{u\frac{\partial v}{\partial r}} \\
+ \overline{\frac{V}{r}\frac{\partial V}{\partial \theta}} + \cancel{\overline{\frac{v}{r}\frac{\partial V}{\partial \theta}}} + \cancel{\overline{\frac{V}{r}\frac{\partial v}{\partial \theta}}} + \overline{\frac{v}{r}\frac{\partial v}{\partial \theta}} \\
+ \overline{W\frac{\partial V}{\partial z}} + \cancel{\overline{w\frac{\partial V}{\partial z}}} + \cancel{\overline{W\frac{\partial v}{\partial z}}} + \overline{w\frac{\partial v}{\partial z}} \\
+ \overline{\frac{UV}{r}} + \cancel{\overline{\frac{Uv}{r}}} + \cancel{\overline{\frac{uV}{r}}} + \overline{\frac{uv}{r}} + \overline{2U\Omega} + \cancel{\overline{2u\Omega}} \\
= \frac{\partial V}{\partial t} + U\frac{\partial V}{\partial r} + \frac{V}{r}\frac{\partial V}{\partial \theta} + W\frac{\partial V}{\partial z} + \underbrace{\overline{u\frac{\partial v}{\partial r}} + \overline{\frac{v}{r}\frac{\partial v}{\partial \theta}} + \overline{w\frac{\partial v}{\partial z}}}_{A_\theta} \\
+ \frac{UV}{r} + \frac{\overline{uv}}{r} + 2U\Omega,
\end{aligned}
\tag{A.30}
$$

where A_θ is

$$
\begin{aligned}
A_\theta &= \overline{\frac{\partial uv}{\partial r}} - \overline{v\frac{\partial u}{\partial r}} + \overline{\frac{1}{r}\frac{\partial vv}{\partial \theta}} - \overline{\frac{v}{r}\frac{\partial v}{\partial \theta}} + \overline{\frac{\partial vw}{\partial z}} - \overline{v\frac{\partial w}{\partial z}} \\
&= \overline{\frac{\partial uv}{\partial r}} + \overline{\frac{1}{r}\frac{\partial vv}{\partial \theta}} + \overline{\frac{\partial vw}{\partial z}} - \overline{v\underbrace{\left(\frac{\partial u}{\partial r} + \frac{1}{r}\frac{\partial v}{\partial \theta} + \frac{\partial w}{\partial z}\right)}_{=-u/r}} \\
&= \frac{\partial \overline{uv}}{\partial r} + \frac{1}{r}\frac{\partial \overline{vv}}{\partial \theta} + \frac{\partial \overline{vw}}{\partial z} + \frac{\overline{uv}}{r}.
\end{aligned}
\tag{A.31}
$$

The RHS of equation (A.20) becomes

$$
\begin{aligned}
\text{RHS(A.20)} &= -\overline{\frac{1}{\rho r}\frac{\partial P}{\partial \theta}} - \cancel{\overline{\frac{1}{\rho r}\frac{\partial p}{\partial \theta}}} + \nu\left[\overline{\frac{\partial^2 V}{\partial r^2}} + \cancel{\overline{\frac{\partial^2 v}{\partial r^2}}} + \overline{\frac{1}{r^2}\frac{\partial^2 V}{\partial \theta^2}} + \cancel{\overline{\frac{1}{r^2}\frac{\partial^2 v}{\partial \theta^2}}}\right. \\
&\quad \left. + \overline{\frac{\partial^2 V}{\partial z^2}} + \cancel{\overline{\frac{\partial^2 v}{\partial z^2}}} + \overline{\frac{1}{r}\frac{\partial V}{\partial r}} + \cancel{\overline{\frac{1}{r}\frac{\partial v}{\partial r}}} - \overline{\frac{V}{r^2}} - \cancel{\overline{\frac{v}{r^2}}} + \overline{\frac{2}{r^2}\frac{\partial U}{\partial \theta}} + \cancel{\overline{\frac{2}{r^2}\frac{\partial u}{\partial \theta}}}\right] \\
&= -\frac{1}{\rho r}\frac{\partial P}{\partial \theta} + \nu\left[\frac{\partial^2 V}{\partial r^2} + \frac{1}{r^2}\frac{\partial^2 V}{\partial \theta^2} + \frac{\partial^2 V}{\partial z^2} + \frac{1}{r}\frac{\partial V}{\partial r} - \frac{V}{r^2} + \frac{2}{r^2}\frac{\partial U}{\partial \theta}\right]
\end{aligned}
\tag{A.32}
$$

Then the RANS of the azimuthal component is written as

$$\frac{\partial V}{\partial t}+U\frac{\partial V}{\partial r}+\frac{V}{r}\frac{\partial V}{\partial \theta}+W\frac{\partial V}{\partial z}+\frac{\partial \overline{uv}}{\partial r}+\frac{1}{r}\frac{\partial \overline{vv}}{\partial \theta}+\frac{\partial \overline{vw}}{\partial z} + \frac{UV}{r}+2\frac{\overline{uv}}{r}+2U\Omega = -\frac{1}{\rho r}\frac{\partial P}{\partial \theta}+\nu\left[\frac{\partial^2 V}{\partial r^2}+\frac{1}{r^2}\frac{\partial^2 V}{\partial \theta^2}+\frac{\partial^2 V}{\partial z^2}+\frac{1}{r}\frac{\partial V}{\partial r}-\frac{V}{r^2}+\frac{2}{r^2}\frac{\partial U}{\partial \theta}\right]. \tag{A.33}$$

A.5.4. *The axial component of the RANS*

The axial direction of the NSE is given from equation (A.21) and decomposed components from equation (A.22) are substituted into equation (A.21). Then the LHS of equation (A.21) is given as

$$\begin{aligned}\mathrm{LHS(A.21)} &= \overline{\frac{\partial W}{\partial t}}+\cancel{\overline{\frac{\partial w}{\partial t}}}+\overline{U\frac{\partial W}{\partial r}}+\cancel{\overline{u\frac{\partial W}{\partial r}}}+\cancel{\overline{U\frac{\partial w}{\partial r}}}+\overline{u\frac{\partial w}{\partial r}} \\ &\quad+\overline{\frac{V}{r}\frac{\partial W}{\partial \theta}}+\cancel{\overline{\frac{v}{r}\frac{\partial W}{\partial \theta}}}+\cancel{\overline{\frac{V}{r}\frac{\partial w}{\partial \theta}}}+\overline{\frac{v}{r}\frac{\partial w}{\partial \theta}} \\ &\quad+\overline{W\frac{\partial W}{\partial z}}+\cancel{\overline{w\frac{\partial W}{\partial z}}}+\cancel{\overline{W\frac{\partial w}{\partial z}}}+\overline{w\frac{\partial w}{\partial z}} \\ &= \frac{\partial W}{\partial t}+U\frac{\partial W}{\partial r}+\frac{V}{r}\frac{\partial W}{\partial \theta}+W\frac{\partial W}{\partial z}+\underbrace{\overline{u\frac{\partial w}{\partial r}}+\overline{\frac{v}{r}\frac{\partial w}{\partial \theta}}+\overline{w\frac{\partial w}{\partial z}}}_{A_z},\end{aligned} \tag{A.34}$$

where A_z is

$$\begin{aligned}A_z &= \overline{\frac{\partial uw}{\partial r}}-\overline{w\frac{\partial u}{\partial r}}+\overline{\frac{1}{r}\frac{\partial vw}{\partial \theta}}-\overline{\frac{w}{r}\frac{\partial v}{\partial \theta}}+\overline{\frac{\partial ww}{\partial z}}-\overline{w\frac{\partial w}{\partial z}} \\ &= \overline{\frac{\partial uw}{\partial r}}+\overline{\frac{1}{r}\frac{\partial vw}{\partial \theta}}+\overline{\frac{\partial ww}{\partial z}}-\overline{w\underbrace{\left(\frac{\partial u}{\partial r}+\frac{1}{r}\frac{\partial v}{\partial \theta}+\frac{\partial w}{\partial z}\right)}_{=-u/r}} \\ &= \frac{\partial \overline{uw}}{\partial r}+\frac{1}{r}\frac{\partial \overline{vw}}{\partial \theta}+\frac{\partial \overline{ww}}{\partial z}+\frac{\overline{uw}}{r}.\end{aligned} \tag{A.35}$$

The RHS of equation (A.21) becomes

$$\begin{aligned}\mathrm{RHS(A.21)} &= -\overline{\frac{1}{\rho}\frac{\partial P}{\partial z}} - \cancel{\overline{\frac{1}{\rho}\frac{\partial p}{\partial z}}} + \nu\left[\overline{\frac{\partial^2 W}{\partial r^2}} + \cancel{\overline{\frac{\partial^2 w}{\partial r^2}}} + \overline{\frac{1}{r^2}\frac{\partial^2 W}{\partial \theta^2}} + \cancel{\overline{\frac{1}{r^2}\frac{\partial^2 w}{\partial \theta^2}}}\right.\\ &\quad \left. + \overline{\frac{\partial^2 W}{\partial z^2}} + \cancel{\overline{\frac{\partial^2 w}{\partial z^2}}} + \overline{\frac{1}{r}\frac{\partial W}{\partial r}} + \cancel{\overline{\frac{1}{r}\frac{\partial w}{\partial r}}}\right] \\ &= -\frac{1}{\rho}\frac{\partial P}{\partial z} + \nu\left[\frac{\partial^2 W}{\partial r^2} + \frac{1}{r^2}\frac{\partial^2 W}{\partial \theta^2} + \frac{\partial^2 W}{\partial z^2} + \frac{1}{r}\frac{\partial W}{\partial r}\right].\end{aligned} \tag{A.36}$$

Then the axial component of the RANS is written as

$$\begin{aligned}&\frac{\partial W}{\partial t} + U\frac{\partial W}{\partial r} + \frac{V}{r}\frac{\partial W}{\partial \theta} + W\frac{\partial W}{\partial z} + \frac{\partial \overline{uw}}{\partial r} + \frac{1}{r}\frac{\partial \overline{vw}}{\partial \theta} + \frac{\partial \overline{ww}}{\partial z} + \frac{\overline{uw}}{r} \\ &\qquad = -\frac{1}{\rho}\frac{\partial P}{\partial z} + \nu\left[\frac{\partial^2 W}{\partial r^2} + \frac{1}{r^2}\frac{\partial^2 W}{\partial \theta^2} + \frac{\partial^2 W}{\partial z^2} + \frac{1}{r}\frac{\partial W}{\partial r}\right].\end{aligned} \tag{A.37}$$

A.5.5. *RANS for incompressible turbulent rotating-disk flow*

RANS for incompressible turbulent rotating-disk flow are derived applying the boundary-layer approximation and some other assumptions. The order of each term is estimated as $r \sim L$, $z \sim \delta$, U and $V \sim V'$, $W \sim (\delta/L)V'$, u, v and $w \sim v'$, $V \sim r\Omega$, namely $\Omega \sim V'/L$ and $P \sim \rho V'^2$, where L is characteristic length, δ is boundary layer thickness, V' is characteristic mean velocity and v' is characteristic fluctuation velocity.

The assumptions for incompressible turbulent rotating-disk flow are:

- ASM1. Steady flow: $\partial/\partial t = 0$,
- ASM2. Axisymmetry: $\partial/\partial \theta = 0$,
- ASM3. Boundary layer approximation: $L \gg \delta$,
- ASM4. A fluid element is convected with a velocity $\mathcal{O}(V')$. In the two time scale of convection $\Delta t_{\mathrm{convection}}$ and diffusion $\Delta t_{\mathrm{diffusion}}$ are defined as

  $$\Delta t_{\mathrm{convection}} \sim L/V', \quad \Delta t_{\mathrm{diffusion}} \sim \delta^2/\nu,$$

  respectively. In the boundary layer both of $\Delta t_{\mathrm{convection}}$ and $\Delta t_{\mathrm{diffusion}}$ are assumed to be of similar size, suck that

  $$\Delta t_{\mathrm{convection}} \sim \Delta t_{\mathrm{diffusion}},$$

  giving

  $$L/V' \sim \delta^2/\nu.$$

These assumpotions are applied to equations (A.29), (A.33) and (A.37), resulting

Radial component (equation (A.29)):

$$\overset{101}{\cancel{\frac{\partial U}{\partial t}}} + U\overset{102}{\frac{\partial U}{\partial r}} + \overset{103}{\cancel{\frac{V}{r}\frac{\partial U}{\partial \theta}}} + W\overset{104}{\frac{\partial U}{\partial z}} + \overset{105}{\cancel{\frac{\partial \overline{uu}}{\partial r}}} + \overset{106}{\cancel{\frac{1}{r}\frac{\partial \overline{uv}}{\partial \theta}}} + \overset{107}{\frac{\partial \overline{uw}}{\partial z}} + \overset{108}{\cancel{\frac{\overline{uu}}{r}}} - \overset{109}{\frac{V^2}{r}} - \overset{110}{\cancel{\frac{\overline{vv}}{r}}} - \overset{111}{2V\Omega} - \overset{112}{r\Omega^2}$$
$$= -\overset{113}{\frac{1}{\rho}\frac{\partial P}{\partial r}} + \nu\left[\overset{114}{\cancel{\frac{\partial^2 U}{\partial r^2}}} + \overset{115}{\cancel{\frac{1}{r^2}\frac{\partial^2 U}{\partial \theta^2}}} + \overset{116}{\frac{\partial^2 U}{\partial z^2}} + \overset{117}{\cancel{\frac{1}{r}\frac{\partial U}{\partial r}}} - \overset{118}{\cancel{\frac{U}{r^2}}} - \overset{119}{\cancel{\frac{2}{r^2}\frac{\partial V}{\partial \theta}}}\right], \tag{A.38}$$

Azimuthal component (equation (A.33)):

$$\overset{201}{\cancel{\frac{\partial V}{\partial t}}} + U\overset{202}{\frac{\partial V}{\partial r}} + \overset{203}{\cancel{\frac{V}{r}\frac{\partial V}{\partial \theta}}} + W\overset{204}{\frac{\partial V}{\partial z}} + \overset{205}{\cancel{\frac{\partial \overline{uv}}{\partial r}}} + \overset{206}{\cancel{\frac{1}{r}\frac{\partial \overline{vv}}{\partial \theta}}} + \overset{207}{\frac{\partial \overline{vw}}{\partial z}} + \overset{208}{\frac{UV}{r}} + \overset{209}{\cancel{2\frac{\overline{uv}}{r}}} + \overset{210}{2U\Omega}$$
$$= -\overset{211}{\cancel{\frac{1}{\rho r}\frac{\partial P}{\partial \theta}}} + \nu\left[\overset{212}{\cancel{\frac{\partial^2 V}{\partial r^2}}} + \overset{213}{\cancel{\frac{1}{r^2}\frac{\partial^2 V}{\partial \theta^2}}} + \overset{214}{\frac{\partial^2 V}{\partial z^2}} + \overset{215}{\cancel{\frac{1}{r}\frac{\partial V}{\partial r}}} - \overset{216}{\cancel{\frac{V}{r^2}}} + \overset{217}{\cancel{\frac{2}{r^2}\frac{\partial U}{\partial \theta}}}\right], \tag{A.39}$$

Axial component (equation (A.37)):

$$\overset{301}{\cancel{\frac{\partial W}{\partial t}}} + \overset{302}{\cancel{U\frac{\partial W}{\partial r}}} + \overset{303}{\cancel{\frac{V}{r}\frac{\partial W}{\partial \theta}}} + \overset{304}{\cancel{W\frac{\partial W}{\partial z}}} + \overset{305}{\cancel{\frac{\partial \overline{uw}}{\partial r}}} + \overset{306}{\cancel{\frac{1}{r}\frac{\partial \overline{vw}}{\partial \theta}}} + \overset{307}{\cancel{\frac{\partial \overline{ww}}{\partial z}}} + \overset{308}{\cancel{\frac{\overline{uw}}{r}}}$$
$$= -\overset{309}{\frac{1}{\rho}\frac{\partial P}{\partial z}} + \nu\left[\overset{310}{\cancel{\frac{\partial^2 W}{\partial r^2}}} + \overset{311}{\cancel{\frac{1}{r^2}\frac{\partial^2 W}{\partial \theta^2}}} + \overset{312}{\cancel{\frac{\partial^2 W}{\partial z^2}}} + \overset{313}{\cancel{\frac{1}{r}\frac{\partial W}{\partial r}}}\right]. \tag{A.40}$$

The following terms in equations (A.38), (A.39) and (A.40) are negligible:

- 101, 201, 301 due to ASM1,
- 103, 106, 115, 119, 203, 206, 211, 213, 217, 303, 306, 311 due to ASM2,
- 105, 108, 110 due to ASM3 which are smaller (δ/L) than 107,
- 114, 117, 118 due to ASM3 which are much smaller (δ^2/L^2) than 116,
- 205, 209 due to ASM3 which are smaller (δ/L) than 207,
- 212, 215, 216 due to ASM3 which are much smaller (δ^2/L^2) than 214,
- 302, 304, 312 due to ASM3 which are much smaller (δ^2/L^2) than 309,
- 310, 313 due to 3 which are much smaller (δ^2/L^2) than 312.

In summary, Reynolds averaged continuity equation and RANS for incompressible turbulent rotating-disk boundary-layer flow are written as

Reynolds averaged continuity equation:

$$\frac{\partial U}{\partial r} + \frac{\partial W}{\partial z} + \frac{U}{r} = 0, \tag{A.41}$$

The radial component of the RANS:

$$U\frac{\partial U}{\partial r} + W\frac{\partial U}{\partial z} - \frac{V^2}{r} - 2V\Omega = -\frac{1}{\rho}\frac{\partial P}{\partial r} + r\Omega^2 + \frac{1}{\rho}\frac{\partial}{\partial z}\left(\mu\frac{\partial U}{\partial z} - \rho\overline{uw}\right), \tag{A.42}$$

The azimuthal component of the RANS:

$$U\frac{\partial V}{\partial r} + W\frac{\partial V}{\partial z} + \frac{UV}{r} + 2U\Omega = \frac{1}{\rho}\frac{\partial}{\partial z}\left(\mu\frac{\partial V}{\partial z} - \rho\overline{vw}\right), \tag{A.43}$$

The axial component of the RANS:

$$\frac{\partial \overline{ww}}{\partial z} = -\frac{1}{\rho}\frac{\partial P}{\partial z}. \tag{A.44}$$

The pressure and centrifugal force terms in equation (A.42) can be transformed as

$$\begin{aligned} -\frac{1}{\rho}\frac{\partial P}{\partial r} + r\Omega^2 &= -\frac{1}{\rho}\left(\frac{\partial P}{\partial r} - \rho r\Omega^2\right) \\ &= -\frac{1}{\rho}\frac{\partial}{\partial r}\left(P - \rho\frac{r^2}{2}\Omega^2\right) \\ &= -\frac{\partial}{\partial r}\left(\frac{P}{\rho} - \frac{1}{2}r^2\Omega^2\right). \end{aligned} \tag{A.45}$$

Equation (A.44) is integrated along the boundary layer, resulting

$$\rho\overline{ww} = -P + P_W, \tag{A.46}$$

where P_W is a wall static pressure. Thus the static pressure P in the turbulent boundary layer on the rotating disk is given as

$$P = P_W - \rho\overline{ww}. \tag{A.47}$$

Part II

Papers

1

Paper 1

A new way to describe the transition characteristics of a rotating-disk boundary-layer flow

By Shintaro Imayama[1], P. Henrik Alfredsson[1] & R. J. Lingwood[1,2]

[1]Linné FLOW Centre, KTH Mechanics, SE-100 44 Stockholm, Sweden
[2]University of Cambridge, Cambridge, CB23 8AQ, UK

Published in *Phys. Fluids* **24**, 031701, 2012

A new method of graphically representing the transition stages of a rotating-disk flow is presented. The probability density function (PDF) contour map of the fluctuating azimuthal disturbance velocity is used to show the characteristics of the boundary-layer flow over the rotating disk as a function of Reynolds numbers. Compared with the variation of the disturbance amplitude (rms) or spectral distribution, this map more clearly shows the changing flow characteristics through the laminar, transitional and turbulent regions. This method may also be useful to characterize the different stages in the transition process not only for the rotating-disk flow but also for other flows.

Experimental studies of the flow over a rotating disk show that the boundary-layer is susceptible to an instability that presents itself through the formation of stationary (in the rotating frame) vortices (see Gregory *et al.* 1955; Kohama 1984; Lingwood 1996; Corke *et al.* 2007). This primary instability can be predicted from linear theory; it is of cross-flow type, inviscid in nature and is a convective instability, and may also have a non-zero frequency, i.e. it can be traveling with respect to the disk. However, unless particular traveling modes are deliberately excited, it is the stationary mode that is observed in experiments because it is excited by unavoidable roughnesses on the disk surface. There is also another convectively unstable mode (a viscous mode due to Coriolis and streamline curvature effects), however, for this mode the stationary disturbances have smaller linear growth rates.

Lingwood (1995, 1997*a*) suggested that the onset of transition to turbulence of the rotating-disk boundary-layer is not due directly to the convective instability, but to an absolute instability which occurs above R=507. Here the Reynolds number is $R = r^*(\Omega^*/\nu^*)^{1/2}$, where r^* is the radius of the disk at the measurement position, Ω^* is the rotational speed of the disk, ν^* is the kinematic viscosity of the fluid and * denotes a dimensional quantity. By

introducing impulsive excitation to the rotating-disk boundary-layer flow, she confirmed experimentally the existence of the absolute instability (above about R=507) by tracking the trajectory of the excited wavepacket (Lingwood 1996). The transition process once triggered probably takes place through a secondary instability (Pier 2003; Kohama 1984).

It is the purpose of the present paper to introduce a PDF map of the azimuthal velocity fluctuations to elucidate the changing flow characteristics through the stable and unstable laminar-flow regions, through the transitional region into the fully turbulent region for the rotating-disk flow.

The experimental set-up is a modified version of the one used by Lingwood (1996), see figure 1. On the original aluminium-alloy disk a new disk made of glass with a thickness of 24 mm and a diameter of 474 mm has been mounted. The aluminum-alloy disk is connected to a DC-servo motor via a vertical shaft and a pressurized air bearing ensures that the vibrations of the disk are small. The surface of the glass disk is polished resulting in a surface roughness of less than 1 μm; the rotational imbalance is less than 10 μm at the edge of the glass disk. At the edge of the disk, a fixed wooden annular plate is positioned flush with the disk surface.

A hot-wire probe with a single sensor made of platinum, with a diameter of 5 μm and 1 mm in length, is operated by a constant-temperature anemometer (CTA) with an overheat ratio of 0.8. The sensing element of the hot-wire is

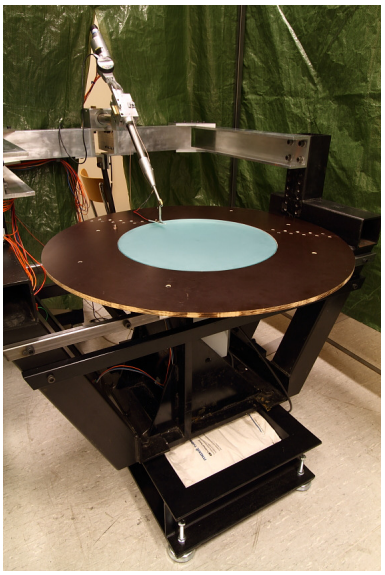

FIGURE 1. The experimental set-up of the rotating disk.

oriented in the radial direction, making it mainly sensitive to the azimuthal velocity. The signal from the CTA is digitized using a 16-bit A/D converter at a sampling rate of 720 data points per disk revolution during a 60 second sampling time. The hot-wire probe is mounted on a two-axis, remotely-controlled traverse mechanism at 45° to the vertical to limit disturbance of the incoming downward axial flow. The calibration of the hot wire is carried out on the rotating disk using the laminar profile and a modified King's law (for better accuracy at low velocities Johansson & Alfredsson 1982) is fitted to the calibration data.

The Reynolds number was varied using two methods: i) varying the rotational disk speed and keeping the probe at a fixed radial position; and ii) varying the radial position of the probe at a fixed rotational disk speed. The experimental conditions are shown in Table 1.

The measured azimuthal mean velocity (V^*) is plotted in figure 2. This corresponds to the azimuthal component of the von Kármán similarity solution for an infinite disk rotating in otherwise quiescent fluid, i.e. a Rossby number of $Ro = -1$, as defined, for example, by Lingwood & Garrett (2011). The measurements are performed at a fixed radius, and in this case the Reynolds number was changed by varying the rotational speed of the disk. The abscissa is the non-dimensional azimuthal velocity, $V = V^*/(r^*\Omega^*)$ and the vertical axis is the non-dimensional height from the wall ($z = z^*(\Omega^*/\nu^*)^{1/2}$). For Reynolds numbers in the range $R = 430 - 510$, the measured profiles correspond well to the theoretical laminar profile shown as a solid line, except far away from the disk where the smallness of the azimuthal velocity makes the hot-wire measurements inaccurate. Between $R = 510$ and $R = 550$ the nonlinear influence of

Case	R	r^*[mm]	Ω^*[rpm]	z
P01	430	198	690	0.4-16
P02	470	198	822	0.4-16
P03	490	198	890	0.4-16
P03	510	198	963	0.4-16
P04	530	198	1040	0.4-16
P05	550	198	1122	0.4-16
P06	570	198	1205	0.4-16
P07	590	198	1295	0.4-26
P08	610	198	1385	0.4-26
P09	630	198	1480	0.4-26
I01	360-700	116-226	1400	1.3

TABLE 1. Experimental conditions, where r^* and z represent the radial and axial positions of the probe, respectively.

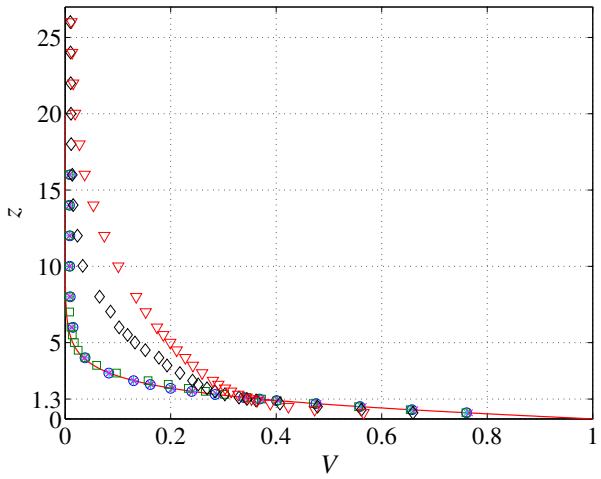

FIGURE 2. Mean azimuthal velocity profiles at R=430 ($\circ$), 470 ($*$), 510 ($\times$), 550 ($\square$), 590 ($\diamondsuit$), 630 ($\triangledown$). Solid line is the laminar theory profile.

the growing disturbances causes the mean azimuthal velocity to deviate from the theoretical laminar profile. With further increases in Reynolds number, this effect grows. At $R = 630$, the velocity profile has completely changed from the basic laminar one, giving a larger velocity gradient close to the wall and a dramatically increased boundary-layer thickness; both characteristics of the development of a turbulent boundary-layer.

The changes in the mean velocity are also reflected in the velocity-fluctuation profiles. Figure 3 shows the non-dimensional intensity of the azimuthal velocity fluctuation ($v_{rms} = v^*_{rms}/(r^*\Omega^*)$) plotted on a logarithmic scale against the wall-normal position. At $R = 430$ and 450, a maximum in v_{rms} is observed close to the disk due to the imbalance of the disk. This effect appears up to $z \approx 2$. At $R = 510$ the v_{rms} profile has developed a well-defined flow-induced maximum close to the wall. At higher Reynolds numbers the velocity-fluctuation profiles reflect the development of a turbulent boundary-layer.

Figure 4 shows the development of the disturbance spectrum measured at $z = 1.3$ for various R. The power spectral amplitudes $P(\omega^*)$ are calculated from the ensemble-averaged time series and are plotted against the non-dimensional quantity ω^*/Ω^*. Linear stability theory shows that the flow is convectively unstable to stationary disturbances above about $R = 290$ (Lingwood 1995). At $R = 430$ one can observe a broad peak centerd around $\omega^*/\Omega^* = 30$ in figure 4. The amplitude of this peak increases with Reynolds number and corresponds to previous experimental studies that show between 28 and 32 stationary vortices

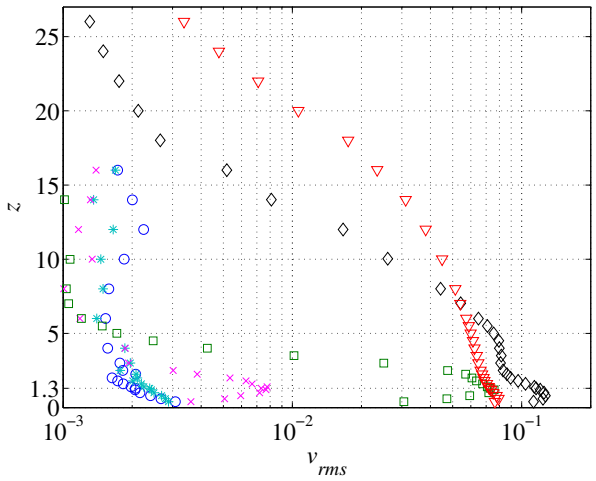

FIGURE 3. Profiles of v_{rms}. The symbols are the same as in figure 2.

(Gregory *et al.* 1955). Note that these stationary vortices are the result of the continuous excitation by unavoidable roughnesses fixed to the disk; it is known, however, from Lingwood (1995) that the azimuthal wavenumber at the onset of absolute instability of the rotating-disk flow (corresponding to a traveling disturbance) is 68. For $R = 510$ a harmonic of the basic frequency appears and at $R = 550$ at least five harmonics can be observed. The onset of nonlinearity is in accordance with the suggestion of Lingwood (1995, 1997*a*) that there is an absolute instability above $R = 507$ and its role is to trigger nonlinearity and the onset of transition despite the fact that the disturbance amplitude at $R \approx 510$ is quite small, less than 0.8% of the disk velocity. At $R = 590$ only the remnant of the primary peak remains with the remainder of the spectrum filled out; by $R = 630$ the spectrum reflects the turbulent nature of the boundary-layer.

In figure 5 the growth of the disturbances is shown from measurements of v_{rms} as a function of Reynolds number, where the Reynolds number was increased by moving the probe in the radial position (case I01 in Table 1). The measurements were made at a constant height $z = 1.3$ because, in the unstable region, the intensity of v_{rms} has a maximum around that position as suggested in figure 3. The data shown are both the directly measured signal, as well as filtered signals. At low R the noise level is high compared to the amplitude of the fluctuations, mainly due to the imbalance of the disk and vibration of the traverse, but through band-pass filtering around the basic frequency the noise level can be lowered by an order of magnitude. For $R \geq 495$ the signal is instead high-pass filtered in order not to exclude the harmonics that start to appear above this R. For the filtered signal an exponential growth, $v_{rms,filtered} \sim$

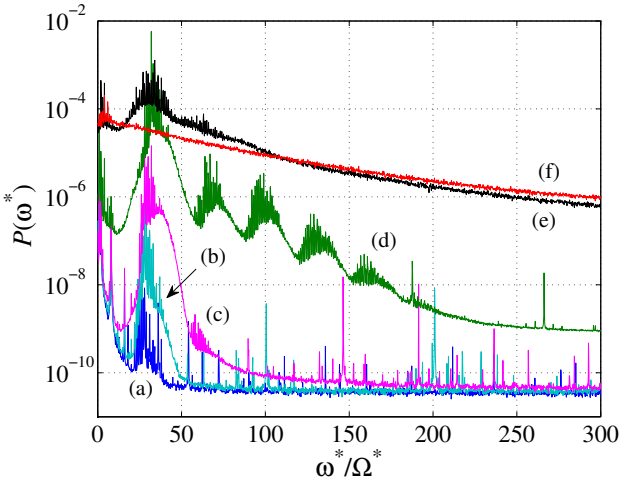

FIGURE 4. Fourier power spectra for ensemble-averaged time series measured at $z = 1.3$ at (a) $R = 430$, (b) $R = 470$, (c) $R = 510$, (d) $R = 550$, (e) $R = 590$, (f) $R = 630$.

$\exp(\alpha R)$, is observed in the region $475 < R < 530$, with $\alpha = 0.058$. This is in agreement with the maximum growth rate for stationary linear disturbances in this R range (see e.g. figure 6a in Hussain *et al.* (2011), note that for spatially growing disturbances α varies with R). Also beyond $R = 530$ there is exponential growth but with a smaller (~ 0.017) rate. Around $R = 580$ v_{rms} reaches a maximum value and thereafter it decreases to a constant level.

It is worth comparing figure 5 with figure 4 of Viaud *et al.* (2011) where the transition to turbulence of the disk boundary-layer flow in an open rotating cavity is described as a secondary instability of the global mode confirming via DNS the possibility of a direct transition mechanism for a real flow through a steep global-mode cascade. By comparison, the change in slope at around $R = 545$ in figure 5 could correspond to Viaud *et al.*'s so-called 'secondary front' where the secondary instability of the primary global mode sets in a little way downstream of the primary global mode, leading to a cascade of absolutely unstable secondary instabilities and transition to turbulence. If so, then the present results may represent the first experimental validation of Viaud *et al.*'s DNS results and Pier's (2003) theoretical predictions of absolute instability of the primary global instability.

The growth rate curve shown in figure 5 does not show any details of how the flow structures change during the transition process. We propose here a new way to present the flow data that makes it possible to gain a better insight into the different stages of the transition process. By plotting

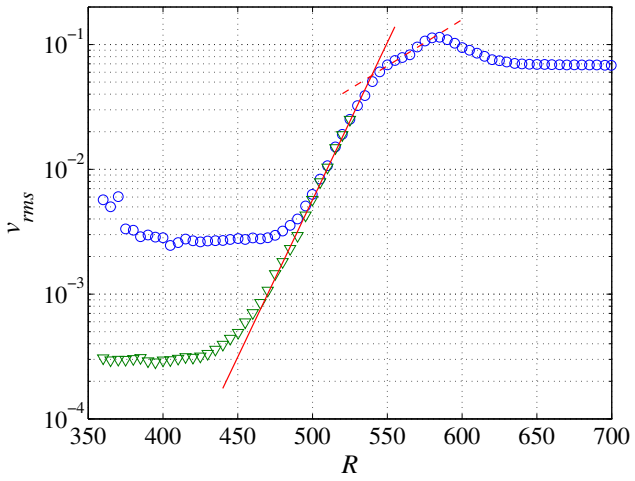

FIGURE 5. v_{rms} variance measured at $z = 1.3$ and a constant rotational speed $\Omega^* = 1400$ rpm. Solid and dashed lines are exponential fittings for each instability region given as $v_{rms} \sim \exp(\alpha R)$, where α is the growth rate. These coefficients for solid and dashed lines are $\alpha = 0.058$ and 0.017, respectively. Circles denote unfiltered signal, triangles show band-pass filtered signal ($17 < \omega^*/\Omega^* < 70$) below $R \leq 490$ and high-passed filtered signal ($17 < \omega^*/\Omega^*$) for $495 \leq R \leq 525$.

the probability density function (PDF) of the fluctuating signal, where the velocity is normalized with the wall velocity and the PDF amplitude with its maximum value, an interesting picture is obtained. Figure 6 shows the resulting color contour plot of the PDF for the same data as in figure5. Even a cursory glance of figure 6 gives a vivid impression of the changes in characteristics with Reynolds number and particularly at $R = 550$.

The PDF is narrow and almost constant up to $R = 475$ due to the background noise and low fluctuation level. At about $R = 475$, the plot is seen to spread exponentially, as also suggested by figure 5. But at $R = 550$, the structure of the PDF has changed dramatically and is strongly skewed. This Reynolds number corresponds to the point where the slope of the exponential growth of v_{rms} changes in figure 5. Figure 6, however, supplies more information compared with figure 5 with regard to the structure of the disturbances. At around $R = 600$, the skewed PDF starts to disappear and the positive deviation of v has its maximum. The almost symmetric PDF above $R = 650$ indicates that the flow has reached a fully developed turbulent state. These

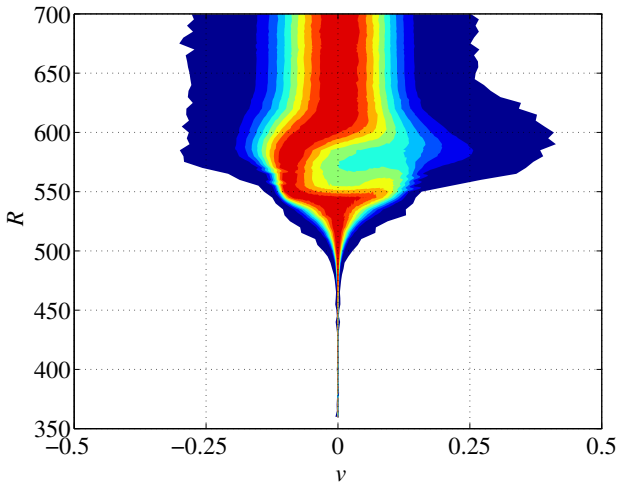

FIGURE 6. The PDF of the filtered instantaneous azimuthal fluctuation velocity v at z=1.3 normalized by the wall speed. Filled contours indicate 10, 20, 30, 40, 50, 60, 70, 80 and 90 % of the local PDF value.

characteristics are not obvious in the spectral distributions such as those in figure 4.

This PDF method is also useful to capture the structure normal to the wall associated with the instability. Figure 7 shows the same quantity as plotted in figure 6, but at fixed Reynolds numbers (increasing by 20 units in each subplot) giving the PDF structure normal to the wall. Below a Reynolds number of 530 the PDF is symmetric around the mean value across the boundary-layer, indicating that the disturbance is near linear below this Reynolds number. By $R = 550$ the PDF becomes strongly asymmetric and around in $z = 1.3$ (figure 7 e) a double peak has appeared marked with + in the figure. At $R = 570$ the picture is complicated further by the appearance of two double peaks, one around $z = 1$ and the other around $z = 2$. For even higher Reynolds numbers the maximum of the PDF again becomes centered around the mean value, which here is indicative of the flow becoming fully turbulent (Alfredsson *et al.* 2011).

In figure 7 an interesting phenomenon is captured at $R = 570$. Kohama (1984) suggested that the secondary instability of the stationary primary vortices (observed using smoke-flow visualization) takes the form of "ring-like vortices which occur on the surfaces of each spiral vortices [sic]". The two peaks in figure 7 (f) of the PDF around $z = 2.0 - 2.8$ may be a manifestation of the secondary instability observed by Kohama. From a theoretical analysis,

Balachandar *et al.* (1992) suggested that secondary vortices are centered over the saddle point of the primary cross-flow vortices. At the same R the position of the primary vortices change from $z = 1.3$ to $z = 1.0$, which explains why the strong skewed PDF is observed in figure 6 above $R = 550$. Figures 6 and 7 together illustrate the structure of the boundary-layer flow through the transition process, comparing well with Viaud *et al.*'s figure 3 showing the nonlinear evolution of an initial perturbation to a disordered state. While not conclusive at this stage, the results shown here support previous experimental (Kohama 1984), theoretical (Pier 2003; Balachandar *et al.* 1992) and numerical (Viaud *et al.* 2011) suggestions of a global nonlinear mode that is itself unstable to secondary perturbations.

As discussed in Lingwood (1997*b*) the maximum convective linear growth rate above $R = 507$ is much larger than the absolute growth rate but given sufficient time the amplitude of disturbances generated by the absolute instability will become large enough to cause nonlinearities and to fix the radial position of the onset of the transition process. As Huerre & Monkewitz (1990) suggested the nonlinear global mode resulting from a finite region of local absolute instability may be thought of as a highly repeatable "self-excited, low-amplitude *wavemaker*...., which acts as a source for the downstream instability wave(s). Furthermore, as discussed by Viaud *et al.* (2011), in a strongly nonlinear and weakly non-parallel regime, the presence of a finite region of absolute instability has been shown theoretically to be a sufficient condition for a nonlinear global mode with a steep front (a so-called 'elephant mode'), located at the upstream boundary (primary front) between local convective and absolute instability, and, further, when the global mode is itself absolutely unstable to local secondary perturbations the transition process is likely to be via the secondary instabilities a short distance downstream of the primary front (Kohama 1984; Pier 2003; Viaud *et al.* 2011).

To summarize, the present work shows a new way to describe the characteristics of a rotating-disk flow by introducing the PDF contour plot of the normalized fluctuation velocity (where the PDF at each z-position is normalized by its maximum value). The map is shown in figure 6 and if compared with spectral and rms distributions in figure 4 and figure 5 it shows the different stages more clearly. It is shown that the PDF can identify an exponentially growing instability, a secondary instability and also clearly shows the onset of the fully developed turbulent flow. In addition, this method is applied to the velocity profile measurements to capture the structure normal to the wall. PDF contour plots at each Reynolds number clearly show the disturbance structure, in particular, peaks in the PDF at $R = 570$ may be associated with a secondary instability. Moreover, the evidence presented herein may represent the first experimental validation of the suggested secondary absolute instability of the primary nonlinear (steep-fronted) global mode (Pier 2003; Viaud *et al.* 2011). As mentioned above, this PDF method may be useful not only for

rotating-disk flows (the so called BEK system of rotating boundary-layer flows Lingwood & Garrett 2011), but also for other transitional flows, for example other three-dimensional boundary-layers, such as those over swept wings, or even more conventional two-dimensional boundary-layer configurations.

This research is supported by the Swedish Research Council (VR) and KTH. We also acknowledge the help from the late Dr Tim Nickels in arranging the loan of the experimental apparatus from the University of Cambridge Department of Engineering to KTH. We also thank the referees for useful comments and for pointing out Viaud *et al.* (2011) to us.

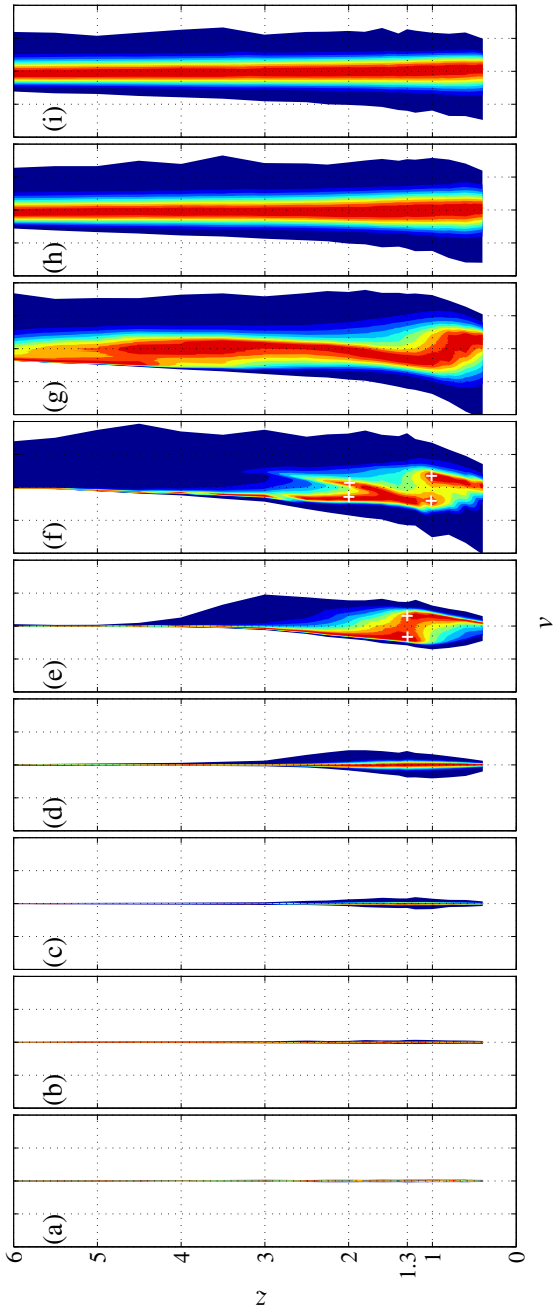

FIGURE 7. The PDF of the instantaneous azimuthal fluctuation velocity normalized by the wall speed to show the z-structure at (a) $R = 470$, (b) $R = 490$, (c) $R = 510$, (d) $R = 530$, (e) $R = 550$, (f) $R = 570$, (g) $R = 590$, (h) $R = 610$, (i) $R = 630$, namely cases P02 to P09 in Table 1. Filled contours indicate same as Fig 6. The range of the abscissa is -0.5 to +0.5 for all R. Note that in the free stream far above the disk, the positive values of v emanates from the high velocity fluid near the disk giving a positive skewness, i.e. the picture here is opposite to the one that would be observed for the flow over a stationary plate where the skewness is negative close to the boundary-layer edge. The white + signs in (e) and (f) show the position of the double peaks.

References

Alfredsson, P. H., Segalini, A. & Örlü, R. 2011 A new scaling for the streamwise turbulence intensity in wall-bounded turbulent flows and what it tells us about the outer peak. *Phys. Fluids* **23**, 041702.

Balachandar, S., Streett, C. L. & Malik, M. R. 1992 Secondary instability in rotating-disk flow. *J. Fluid Mech.* **242**, 323–347.

Corke, T. C., Matlis, E. H. & Othman, H. 2007 Transition to turbulence in rotating-disk boundary layersconvective and absolute instabilities. *J. Eng. Math.* **57**, 253–272.

Gregory, N., Stuart, J. & Walker, W. S. 1955 On the stability of three-dimensional boundary layers with application to the flow due to a rotating disk. *Phil. Trans. R. Soc. Lond.* **248**, 155–199.

Huerre, P. & Monkewitz, P. A. 1990 Local and global instabilities in spatially developing flows. *Annu. Rev. Fluid Mech.* **22**, 473–537.

Hussain, Z., Garrett, S. J. & Stephen, S. O. 2011 The instability of the boundary layer over a disk rotating in an enforced axial flow. *Phys. Fluids* **23**, 114108.

Johansson, A. V. & Alfredsson, P. H. 1982 On the structure of turbulent channel flow. *J. Fluid Mech.* **122**, 295–314.

Kohama, Y. 1984 Study on boundary layer transition of a rotating disk. *Acta Mech.* **50**, 193–199.

Lingwood, R. J. 1995 Absolute instability of the boundary layer on a rotating disk. *J. Fluid Mech.* **299**, 17–33.

Lingwood, R. J. 1996 An experimental study of absolute instability of the rotating-disk boundary-layer flow. *J. Fluid Mech.* **314**, 373–405.

Lingwood, R. J. 1997*a* Absolute instability of the Ekman layer and related rotating flows. *J. Fluid Mech.* **331**, 405–428.

Lingwood, R. J. 1997*b* On the Application of the Briggs' and Steepest-Descent Methods to a Boundary-Layer Flow. *Stud. Appl. Math.* **98**, 213–254.

Lingwood, R. J. & Garrett, S. J. 2011 The effects of surface mass flux on the instability of the BEK system of rotating boundary-layer flows. *Eur. J. Mech. B-Fluid.* **30**, 299–310.

Pier, B. 2003 Finite-amplitude crossflow vortices, secondary instability and transition in the rotating-disk boundary layer. *J. Fluid Mech.* **487**, 315–343.

Viaud, B., Serre, E. & Chomaz, J.-M. 2011 Transition to turbulence through steep global-modes cascade in an open rotating cavity. *J. Fluid Mech.* **688**, 493–506.

2

Paper 2

An Experimental Study of Edge Effects on Rotating-Disk Transition

By Shintaro Imayama[1], P. Henrik Alfredsson[1] & R. J. Lingwood[1,2]

[1]Linné FLOW Centre, KTH Mechanics, SE-100 44 Stockholm, Sweden
[2]University of Cambridge, Cambridge, CB23 8AQ, UK

To be submitted

The effects of the edge of the disk on laminar-turbulent transition of the rotating-disk boundary-layer flow are discussed. Healey (*J. Fluid. Mech.*, vol. 663, 2010, pp. 148-159) suggested, using the linearized complex Ginzburg-Landau equation, that the transition Reynolds number for the rotating-disk flow can be affected by the Reynolds number at the edge of the disk. He compared his theoretical work with experiments performed by various researchers, which seemed to confirm the suggested change in the transition Reynolds number dependent on the edge Reynolds number. However, our experimental results with varying edge Reynolds number and edge condition do not show such behaviour. We discuss the transition Reynolds number as defined by each of the cited authors, and suggest the variations are explained by the different definitions they use rather than the proximity of the edge of the disk to the transition region.

---

1. Introduction

We discuss an incompressible rotating-disk boundary-layer flow without any imposed flow. The laminar boundary layer established on a rotating-disk has a three-dimensional profile with an inflection point in the radial direction. For an infinite disk rotating in an otherwise quiescent fluid there is an exact similarity solution, first described by von Kármán (1921). The Rossby number for the von Kármán flow is $Ro = -1$, as defined, for example, by Lingwood & Garrett (2011). The instability and transition of the rotating-disk flow has been investigated starting with Theodorsen & Regier (1944) and Smith (1947) who noticed fluctuations in the boundary layer on the rotating disk using a hot-wire probe. Visualization studies performed by Gregory *et al.* (1955) and Kohama (1984) showed 28-32 stationary (in the rotating frame) vortices in the unstable region. Experiments by Kobayashi *et al.* (1980) and Malik *et al.* (1981) using hot-wire

anemometry both gave the Reynolds number for the onset of convective instability for stationary modes slightly below 300, where $R = r^*(\Omega^*/\nu^*)^{1/2}$, r^* is the radius of the disk at the measurement position, Ω^* is the rotational speed of the disk, ν^* is the kinematic viscosity of the fluid and * denotes a dimensional quantity. Local linear stability analyses (Lingwood 1995) also reveal this unstable region with two different modes: an inviscid instability mode, called Type I, caused by an inflection point in the radial velocity component, and a viscous instability mode, called Type II, caused by streamwise curvature and Coriolis effects. Type II stationary disturbances have smaller linear growth rates than Type I.

There are other stable modes, and one of these, henceforth called Type III, was shown by Lingwood (1995, 1997) to coalesce with Type I above $R_{CA} = 507$ for certain travelling waves. Here R_{CA} is the critical Reynolds number for onset of local absolute instability. The absolute instability is an inviscid mechanism and Lingwood (1995) suggested it had a role in triggering nonlinearity, related to the onset of transition to turbulence. By introducing impulsive excitation to the rotating-disk boundary-layer flow, she confirmed experimentally the absolute instability (above about $R = 507$) by tracking the trajectory of the excited wavepacket (Lingwood 1996) and showed the development of nonlinearity and the onset of the transition process from there, resulting in a fully turbulent flow about $R = 600 - 650$. Theodorsen & Regier (1944), Kobayashi *et al.* (1980) and Othman & Corke (2006) performed careful low-disturbance experiments, and gave transition Reynolds numbers in the range 539-566, numbers that are higher than the critical absolute Reynolds number. Davies & Carpenter (2003) performed direct numerical simulations solving the linearized Navier-Stokes equations and suggested that the convective behaviour eventually prevails even for strongly locally absolutely unstable regions and concluded that the absolute instability does not produce a *linear* amplified global mode.

Taking this point into account, Pier (2003) suggested that a *nonlinear* approach is required to explain the self-sustained behaviour of the rotating-disk flow. He suggested that the rotating-disk boundary layer has a primary nonlinear global mode fixed by the local absolute instability, predicted by Lingwood (1995), which has a secondary absolute instability that triggers the transition to turbulence. In fact Kohama (1984) did smoke-flow visualization that shows a secondary instability on the stationary *primary* vortices, which takes the form of "ring-like vortices that occur on the surfaces of each spiral vortices [sic]". Furthermore, Imayama *et al.* (2012) represented the vertical structure of the vortices that show signs of secondary instability at $R = 570$ just before the turbulent breakdown region. However, the behaviour of the secondary instability and also its relation to the primary absolute instability are not fully understood as yet.

Othman & Corke (2006) performed experiments similar to those of Lingwood (1996) but used both a low-amplitude and a high-amplitude initial pulse-jet excitation to create a wave-packet disturbance in the boundary-layer flow. Contrary to Lingwood (1996) the trailing edge of the wavepacket did not become fixed at R_{CA} with the low-amplitude initial disturbance, hence the results agree well with the linearized DNS of Davies & Carpenter (2003). On the other hand, the amplitude of the wavepacket with the high-amplitude initial disturbance compares better with the result of Lingwood (1996), although it is not certain that the trailing edge of the wavepacket becomes fixed at R_{CA}. However, Imayama *et al.* (2012) suggested that the change in slope at around $R = 545$ in disturbance growth (their figure 5) could correspond to the so-called 'secondary front' suggested by Viaud *et al.* (2011), leading to a cascade of absolutely unstable secondary instabilities and transition to turbulence. This observation by Imayama *et al.* (2012) is perhaps the first experimental validation of the theoretical predictions of absolute instability of the primary global instability by Pier (2003) and the corresponding DNS results of Viaud *et al.* (2011).

In addition to the studies described above, Healey (2010) suggested that the proximity of the edge of the disk to the transition region is important; an effect not captured by standard analyses assuming an infinite disk radius. He recognized the scatter of experimentally-observed transition Reynolds number R_t reported by previous authors as can be seen in table 1. He argued that, based on investigations of the linearized complex Ginzburg-Landau equation, the transition Reynolds number should depend on the Reynolds number at the edge of the disk, R_{edge}, where $R_{edge} = r_d^*(\Omega^*/\nu^*)^{1/2}$, r_d^* is the actual radius of the disk, with the assumption that the transition to turbulence is related to the appearance of a steep-fronted nonlinear global mode. Figure 7(b) of Healey (2010) shows the variation in the experimentally-observed transition Reynolds number depending on the edge Reynolds number compared with his theoretical prediction. In the present paper, we will discuss the effect of the edge of the disk on the instability and transition process based on experimental results. The study includes measurements of the flow with a range of edge Reynolds numbers and several different edge conditions. We observed no obvious effect of the proximity of the disk edge or of the nature of the edge condition on the transtion process. In addition, we suggest the scatter of the transition Reynolds number reported by previous authors is explained by their different definitions of what constitutes transition.

2. Experimental set-up and procedure

The experimental set-up is a modified version of the one used by Lingwood (1996). On the original aluminium-alloy disk a new disk made of glass with a thickness of 24 mm and a diameter of 474 mm has been mounted. At the edge of the disk the glass disk is ground down approximately 1.5 mm with a

Authors	R_t	Method
Theodorsen & Regier (1944)	557	Hot-wire
Gregory *et al.* (1955)	533	Visual, China-clay
Cobb & Saunders (1956)	490	Heat transfer
Gregory & Walker (1960)	524	Pressure probe
Chin & Litt (1972)	510	Mass transfer
Fedorov *et al.* (1976)	515	Visual, napthalene
Clarkson *et al.* (1980)	562	Visual, dye
Kobayashi *et al.* (1980)	566	Hot-wire
Malik *et al.* (1981)	520	Hot-wire
Wilkinson & Malik (1985)	550	Hot-wire
Lingwood (1996)	508	Hot-wire
Othman & Corke (2006)	539	Hot-wire

TABLE 1. Experimental R_t given in previous studies using various experimental techniques.

45° angle. This is why the actual radius of this glass is r_d^*=235.5 mm. The aluminum-alloy disk is connected to a DC-servo motor via a vertical shaft, and a pressurized air bearing ensures that the vibrations of the disk are small. The surface of the glass disk is polished resulting in a surface roughness of less than 1 μm; the rotational imbalance is less than 10 μm at the edge and smaller at the centre region of the glass disk

To investigate the effect on the transition process caused by the disk edge condition, different conditions have been considered. Figure 1 shows the three different edge conditions. Figure 1(a) shows the 'open type', which has no extended plate or cover, figure 1(b) shows the 'ring type', where there is a steel ring mounted below the surface of the disk covering eight aluminum clamps fixing the glass disk to the aluminum-alloy disk. These clamps, which are below the vertical edge of the glass disk, generate a disturbances field with eight oscillations per rotation of the disk if not covered. The ring is mounted around them to eliminate their contribution to the flow disturbance field. The ring itself does not rotate and the horizontal gap between the ring and glass disk is less than 1 mm. The edge of the glass disk is still exposed in a similar way to the open-type edge condition because the top of the ring is located 11 mm vertically below the disk surface. The third case, figure 1(c) is called 'plate type', which consists of a non-rotational extended annular plate made of wood with an outside diameter of 900 mm mounted around the glass disk. This extended plate eliminates the effects of the eight aluminum fixing components and also reduces the effects of noise coming from the air bearing and DC-servo

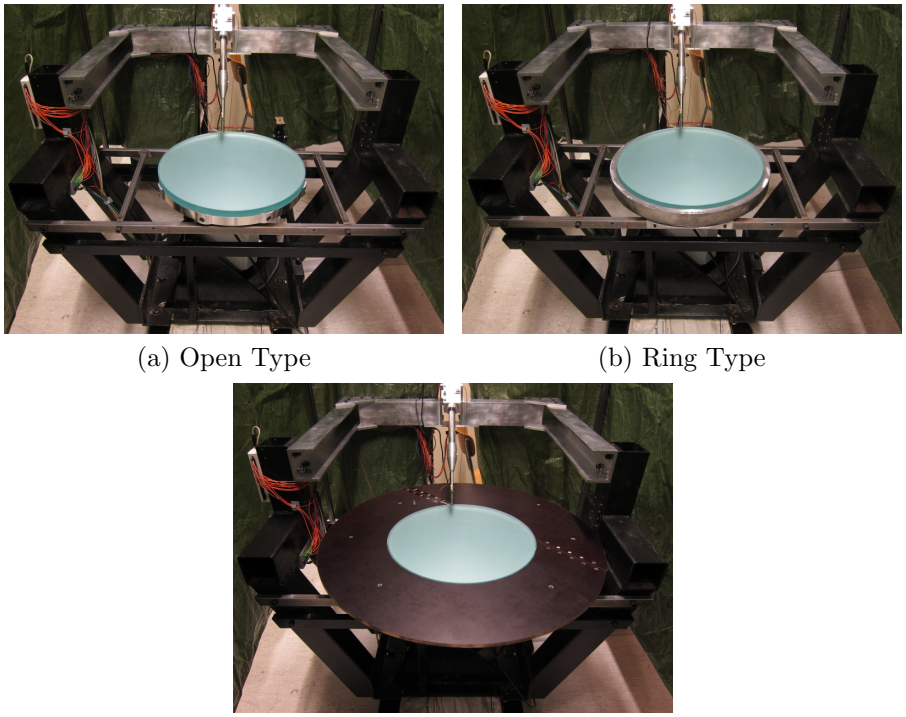

(a) Open Type (b) Ring Type

(c) Plate Type

FIGURE 1. Three edge conditions.

motor. The horizontal gap between the disk and plate is less than 1 mm and vertically the disk surface and plate are approximately flush.

A hot-wire probe with a single sensor made of platinum, with a diameter of 5 μm and 1 mm in length, is operated by a constant-temperature anemometer (CTA) with an overheat ratio of 0.8. The sensing element of the hot-wire is oriented in the radial direction, making it mainly sensitive to the azimuthal velocity. The signal from the CTA is digitized using a 16-bit A/D converter at a sampling rate of 720 data points per disk revolution during a 60 second sampling time. The hot-wire probe is mounted on a two-axis, remotely-controlled traverse mechanism at 45° to the vertical to limit disturbance of the incoming downward axial flow. The calibration of the hot wire is carried out on the rotating disk using the laminar profile and a modified (to obtain better accuracy at low velocities, see Johansson & Alfredsson 1982) King's law is fitted to the calibration data.

The experimental conditions are shown in table 2. The Reynolds number was varied using two methods: i) varying the rotational disk speed and keeping

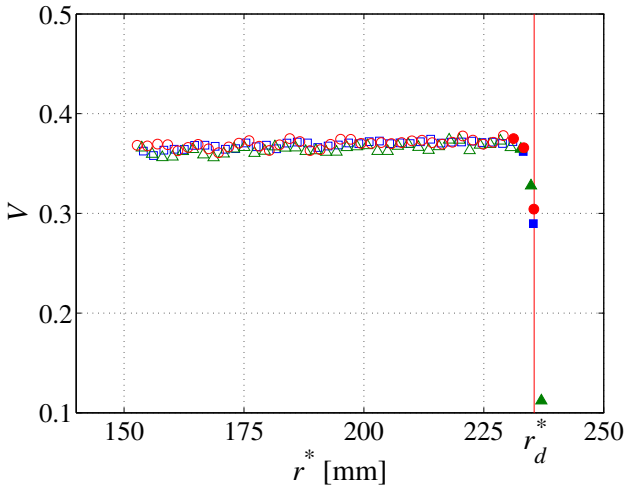

FIGURE 2. Mean velocity nomalized by wall velocity of IO01(□), IR01(△) and IP01(○) measured at $z = 1.3$ as function of r^*. The filled data points indicate removed data from the analysis, because V is reduced suddenly due to the proximity of the edge of the disk. The solid line shows the radius of the actual glass disk r_d^*.

the probe at a fixed radial position for the PO, PR, PP, IR00 cases; and ii) varying the radial position of the probe at a fixed rotational disk speed for other cases. The measurements were performed taking extreme care with the glass surface. Before rotating the disk, the surface of glass disk was cleaned with acetone and carefully checked that there were no visible dust particles on the surface. The Reynolds numbers for IO, IR and IP were changed every 5 ΔR across the measurement range, where ΔR is the unit Reynolds number. All measurements are in the laboratory frame rather than the disk's rotational frame.

For the IO, IR and IP cases, the Reynolds number was changed by varying the radius at which the measurements were taken. The maximum measurement Reynolds number for these cases does not reach the edge Reynolds number exactly shown in table 2, i.e. the maximum measurement Reynolds number in IO01 is 540 despite $R_{edge} = 551$. This is because the mean flow field is disturbed very close to the disk edge. Figure 2 shows normalized azimuthal velocity V at a constant height and each constant rotational speed. Within $3 - 4$ mm of the outer edge the normalized azimuthal velocity suddenly drops, and so data measured this close to the outer edge were removed from the following results and discussions.

Case	Edge	Mode	R	R_{edge}	r^*[mm]	Ω^*[rpm]	z
PO	Open	Speed	430-630	512-749	198	683-1465	0.4-16(26)
PR	Ring	Speed	430-630	511-749	198	675-1455	0.4-16(26)
PP	Plate	Speed	430-630	512-749	198	690-1480	0.4-16(26)
IR00	Plate	Speed	360-640	428-763	198	486-1542	1.3
IO01	Open	Radius	360-540	551	154-231	800	1.3
IO02	Open	Radius	360-565	577	147-231	865	1.3
IO03	Open	Radius	360-605	615	138-231	1000	1.3
IO04	Open	Radius	360-700	730	116-226	1400	1.3
IR01	Ring	Radius	360-540	552	154-231	800	1.3
IR02	Ring	Radius	360-565	576	147-231	860	1.3
IR03	Ring	Radius	360-605	615	138-232	982	1.3
IR04	Ring	Radius	360-700	729	116-226	1380	1.3
IP01	Plate	Radius	360-540	555	153-229	800	1.3
IP02	Plate	Radius	360-565	577	147-231	860	1.3
IP03	Plate	Radius	360-605	618	137-231	1000	1.3
IP04	Plate	Radius	360-700	731	116-226	1400	1.3

TABLE 2. Experimental conditions. "Edge" indicates three kinds of edge conditions, see figure 1. *Mode* indicates the Reynolds number change method (*Speed*: Reynolds number is changed by varying the rotational speed of the glass disk; *Radius*: Reynolds number is changed by varying the radius of the hot-wire position). Here, r^* is a local radius of the hot-wire and z is the normalized wall-normal position of the hot-wire, respectively.

3. Results

3.1. *Azimuthal Mean Velocity Profile*

The azimuthal mean velocity profiles with three different edge conditions are shown in figure 3. The Reynolds numbers for these velocity-profile measurements were changed by varing the rotational speeds, and these results correspond to cases PO, PR and PP with R_{edge} given by table 2. For Reynolds numbers in the range $R = 430 - 510$, the measured profiles correspond well to the theoretical laminar profile shown as a solid line for all edge conditions, except far away from the disk where the smallness of the azimuthal velocity makes the hot-wire measurements inaccurate. Between $R = 510$ and $R = 550$ the nonlinear influence of the growing disturbances causes the mean azimuthal velocity to deviate from the theoretical laminar profile for all three different

edge conditions, see small sections in figure 3. The plate type has larger deviations than the other two cases at $R = 550$ and $R = 590$. With further increases in Reynolds number, this effect grows. At $R = 630$, the velocity profile has completely changed from the basic laminar one, giving a larger velocity gradient close to the wall and a dramatically increased boundary-layer thickness; both characteristics of the development of a turbulent boundary layer.

3.2. *Azimuthal Fluctuation Velocity Profile*

In figure 4 the growth of disturbances v_{rms} is shown as a function of Reynolds number. The Reynolds number at the measurement position was changed by varying the radial position of the hot-wire for IO01-04, IR01-04 and IP01-04 (shown in table 2) holding the edge Reynolds number constant. Only for IR00 was the Reynolds number changed by varying the rotational speed of the disk so that the edge Reynolds number varied. The measurements were performed at a constant height $z = 1.3$. because, in the unstable region, the intensity of v_{rms} has a maximum around that position, see figure 3 in Imayama *et al.* (2012).

At low R we measured different background-noise levels depending on the edge conditions. In all cases, the experiments with the highest rotational speed (IO04, IR04, IP04) have the largest background-noise levels. This is due to higher levels of vibration of the traverse and disk at higher rotational speeds. On the other hand, the lowest background-noise levels are observed in IO03, IR03 and IP03. This is because compared with the measurements performed in cases IO01-02, IR01-02 and IP01-02 those started from smaller radial positions where the imbalance of the disk is smaller, and the rotational speeds are smaller than IO04, IR04 and IP04. All of measurements in open-type have larger background-noise levels compared with the ring-type and plate-type. This is because eight aluminium components connect the glass disk to the aluminum-alloy disk and these disturb the flow contributing to the background noise. In the ring-type and plate-type cases these eight aluminum components are masked by the ring cover and wooden annual plate, respectively, see figure 1.

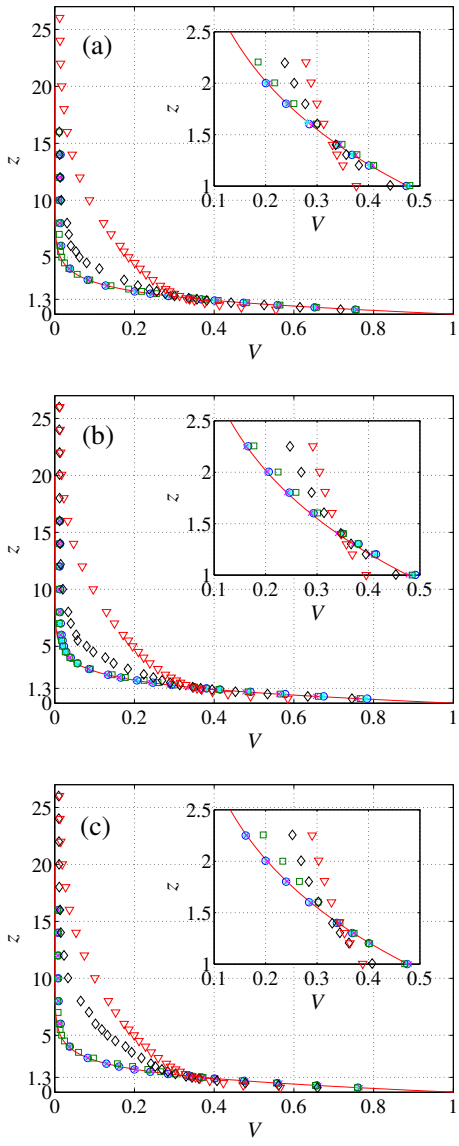

FIGURE 3. Mean azimuthal velocity profiles with three different edge conditions (PO case (a), PR case (b), PP case (c)) at R=430 ($\circ$), 470 ($*$), 510 ($\times$), 550 ($\square$), 590 ($\diamondsuit$), 630 ($\triangledown$). The solid line is the laminar theory profile. The small figures inside the main figures show magnified regions of the velocity profiles are affected by nonlinearity.

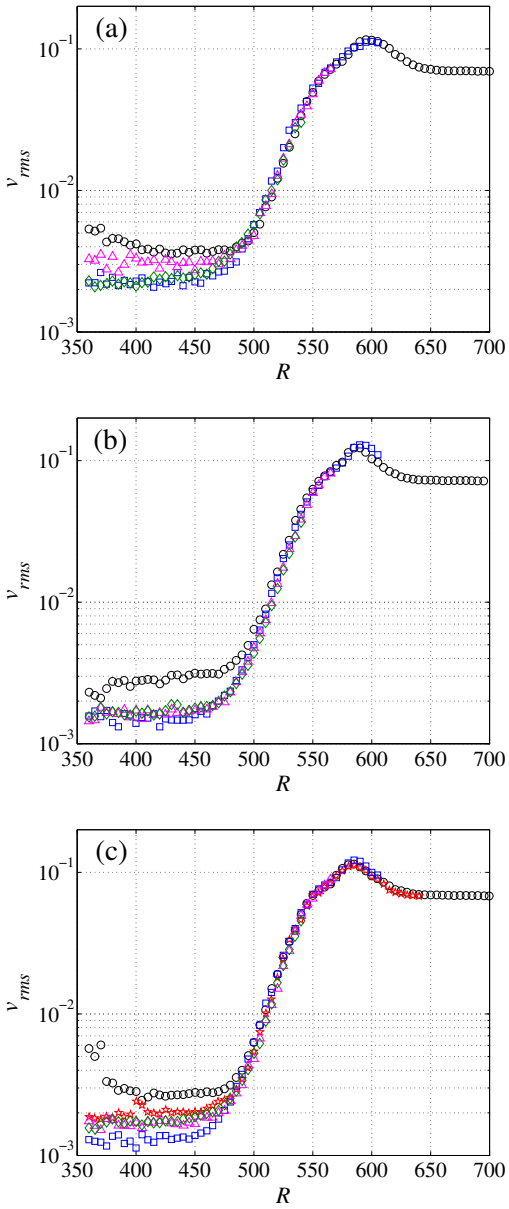

FIGURE 4. v_{rms} measured at $z = 1.3$ for various edge conditions (IO case (a), IR case (b), IP case (c)). The symbols indicate 00($\star$), 01($\diamond$), 02($\triangle$), 03($\square$), 04($\circ$) cases respectively, where 00-04 cases are described in table 2.

At $R \leq 480$ the background-noise level is relatively high compared with the amplitude of the fluctuations due to convective instability. But at $R > 480$ the flow disturbances start to exceed the background level and the exponential growth of v_{rms} is observed up to $R = 585 - 595$ for all edge conditions. These exponential growth regions match within 10 ΔR for all edge conditions and edge Reynolds numbers. The change of the exponential growth is observed at $R = 545 - 555$ which could be evidence of a "secondary front" as described by Viaud *et al.* (2011). These results suggest three things about the transition process of the rotating-disk boundary layer. First, the background disturbance source from outside the boundary layer does not affect the transition process significantly in these cases. Secondly differences in the edge conditions, namely whether there is a extended annual plate around the glass disk or not, also does not affect it. Third, the data with different edge Reynolds numbers match closely, which suggests the edge Reynolds number does not affect the transition process.

3.3. *Probability Density Function Profile*

To gain a better insight into the different stages of the transition process, in particular how the transition process progresses with increasing Reynolds number, Imayama *et al.* (2012) introduced a probability density function (PDF) map of the instantaneous fluctuation velocity normalized by the wall velocity and the PDF amplitude normalized with its maximum value in order to illustrate the process. Figure 5 shows the resulting colour contour plot of the PDF for the same data as in figure 4. The open, ring and plate types in figure 5 (a-c) represent the superposition of different edge conditions, namely IO01, IR01 and IP01 are used for $360 \leq R \leq 540$, IO02, IR02 and IP02 are used for $540 < R \leq 565$, IO03, IR03 and IP03 are used for $565 < R \leq 605$ and IO04, IR04 and IP04 are used for $605 < R \leq 700$. Figure 5 (d) shows the single plate-type (IR00) case. If the transition process were affected by the edge Reynolds number, then the superposition PDF map would include significant discontinuities. However, figure 4 indicates continuous and similar PDF trends as a function of the measurement Reynolds number. The ring-type case in figure 5 (b) has a slightly discontinuous region at $R = 605$, however the gap is less than 10 ΔR.

In figure 5 the PDF is narrow and constant at $R < 475$. The open-type case is slightly broader at low Reynolds number compared with the other edge conditions due to higher background-noise levels. At $R \geq 475$ the PDF spreads exponentially up to about $R = 550$ corresponding to the secondary front as shown figure 4. At $R = 550$, the structure of the PDF changes dramatically and becomes strongly skewed. This is indicative of secondary instability, as also shown by figure 7 in Imayama *et al.* (2012). At around $R = 600$, the skewed PDF starts to disappear and the positive deviation of v has its maximum. The almost symmetric PDF above $R = 650-660$ indicates that the flow has reached a fully developed turbulent state.

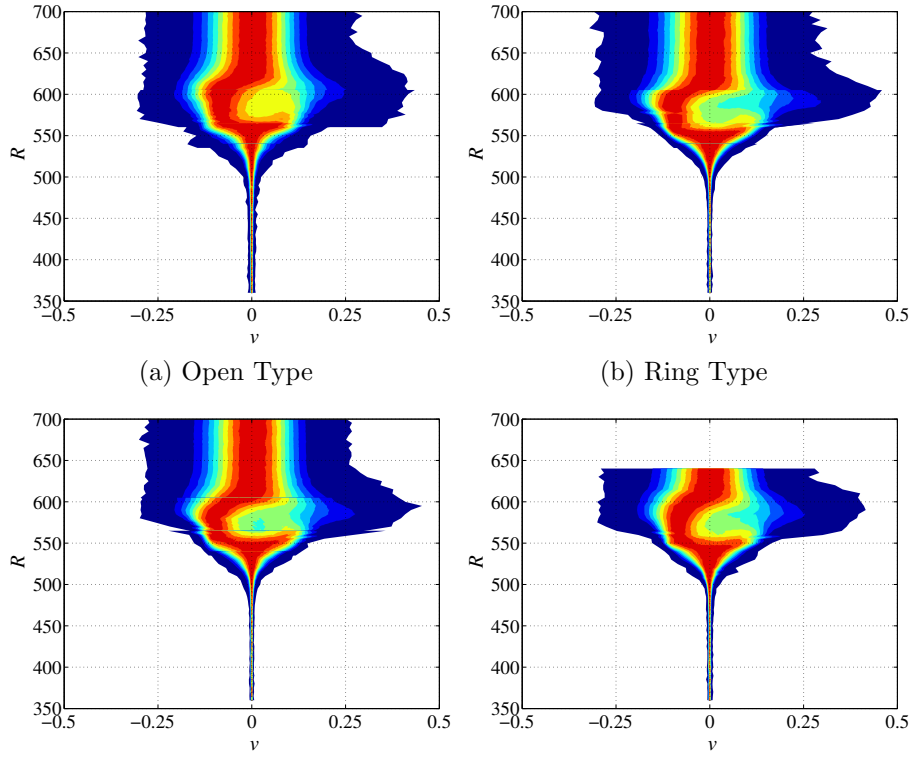

(a) Open Type (b) Ring Type

(c) Plate Type (d) Plate Type (IR00)

FIGURE 5. PDFs of the instantaneous azimuthal fluctuation velocity v at z=1.3 normalized by the wall speed with various edge conditions and the two different modes of changing the measurement Reynolds number, i.e. by varying radial position or by varying rotational speed. Filled contours indicate 10, 20, 30, 40, 50, 60, 70, 80 and 90 % of the local PDF value.

4. Discussion of results

The present results as shown in figure 4 and figure 5 show that the development of the flow is indepedent of the edge Reynolds number and edge conditions. We need then to consider the scatter of the transition Reynolds number reported by the previous authors and the result of Healey (2010) which proposes that the transition Reynolds number for the rotating-disk flow can be affected by the edge Reynolds number. Here, table 3 shows the transition Reynolds number in recent studies measured using a hot-wire probe listing the transition Reynolds numbers in ascending order. The previous authors used different definitions

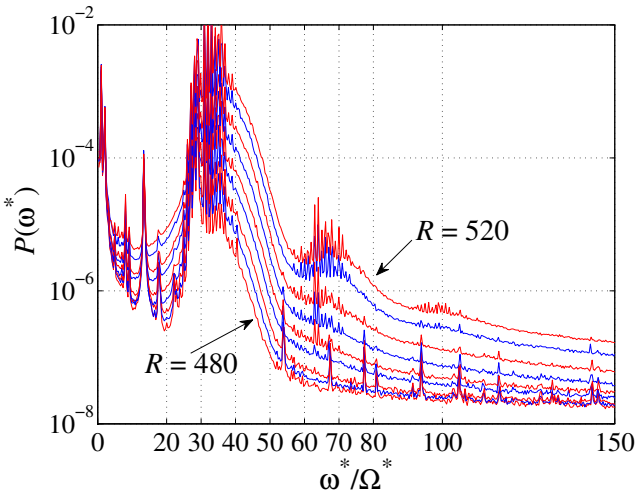

FIGURE 6. Ensemble-averaged spectrum $P(\omega^*)$ at 5 ΔR intervals between $R = 480$ and $R = 520$ measured at $z = 1.3$ (IP04).

for the transition Reynolds number, however, and the present data will be compared with each definition.

Lingwood (1995, 1997) suggested that the local absolute instability appears above $R = 507$ and that it triggers nonlinearity. Here, we define the 'transition Reynolds number', R_t, as the onset of nonlinearity where the amplitude of the harmonics of the primary vortices reaches 10^{-6} in terms of the ensemble-averaged power spectrum intensity of the azimuthal velocity.[1] Figure 6 shows an example of the transition Reynolds number definition of the ensemble-averaged power spectrum. At $R = 480$ the spectrum due to the primary vortices appears at around $\omega^*/\Omega^* = 31$ and the spectrum band for the primary vortices expands with increasing Reynolds number. This result corresponds to figure 6 in Malik *et al.* (1981) so that the number of vortices increases as a function of Reynolds number. The peak around $\omega^*/\Omega^* = 1$ is due to imbalance of the disk. At $R = 500$, nonlinearity starts to cause harmonics of the primary vortices to appear at around $\omega^*/\Omega^* = 63$. At $R = 510$, the amplitude of the harmonics reaches 10^{-6} in the power-spectrum scale. Thus, with this definition, the onset of the transition is suggested to be $R_t = 510$.

However Malik *et al.* (1981) use a different definition for the transition Reynolds number (520), namely that turbulent spots start to appear. We

[1] The power spectrum is defined as $P(\omega^*) = (2/N_{FFT}^2)|H(\omega^*)|^2$, where $H(\omega^*)$ is the discrete Fourier transform of the time series and the normalization factor is $N_{FFT} = 2048$, which is the number of data points in one period of each discrete Fourier transform in this study.

Authors	R_t	The definition
Lingwood (1996)	508	Onset of nonlinearity
Malik *et al.* (1981)	520	Appearance of turbulent spots
Othman & Corke (2006)	539	Onset of deformation of laminar profile
Wilkinson & Malik (1985)	550	Breakdown of the vortices
Kobayashi *et al.* (1980)	566	Entire loss of periodic velocity fluctuations

TABLE 3. Experimental R_t (as defined in the original studies) performed by previous authors using hot-wire measurements and listed in ascending order.

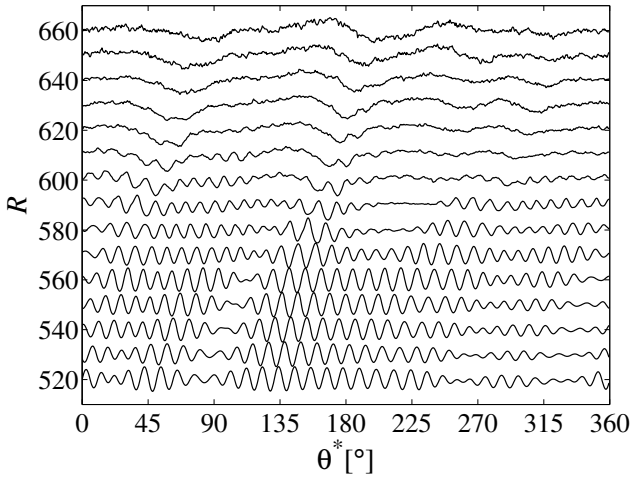

FIGURE 7. Ensemble-averaged timeseries of the azimuthal velocity at various measurement Reynolds numbers at $z = 1.3$ for Plate Type (IP04). The signals are normalized by the maximum peak-to-peak amplitude. Measurements are taken in the laboratory frame of reference.

sometimes observed wavepackets not only at $R = 520$ but over a range of $R < 550$ appearing non-periodically and non-repeatably. In our case, this may be due to dust falling from above and either being carried through the boundary layer without attaching or becoming attached to the surface, but in either case disturbing the flow inside the boundary layer and creating the wavepacket disturbance. At higher Reynolds numbers the wavepacket has turbulent characteristics but at $R = 520$ we found a very low probability of turbulent-spot

formation. We suggest that turbulent spots at around $R = 520$ are likely to be a result of large initial disturbances, e.g. falling dust, rather than a 'natural' part of the transition process and therefore that this definition of transition Reynolds number for the rotating-disk flow is inappropriate.

Othman & Corke (2006) define the transition Reynolds number as the onset of deformation of the laminar azimuthal velocity profile due to nonlinearity, giving $R_t = 539$. Here, figure 3 shows this behaviour between $R = 510$ and $R = 550$ for all edge conditions corresponding broadly to the result of Othman & Corke (2006).

Wilkinson & Malik (1985) and Kobayashi *et al.* (1980) gave higher values of the transition Reynolds number, namely 550 and 566, respectively. However, their definitions are related to the turbulent breakdown of the instability structures, and are defined as the onset of breakdown of the primary vortices and entire loss of periodicity, respectively.

Figure 7 shows ensemble-averaged timeseries of peak-normalized azimuthal velocity (averaged over 1000 revolutions) at 10 ΔR intervals. At $R = 520$ in figure 7 approximately 33 stationary oscillations are observed per rotation; these are the primary vortices, see figure 2 in Kohama (1984). Between $R = 520$ and $R = 560$ the amplitude of each primary vortex is not constant. This is because the disturbance field is a superposition created by a random distribution of unavoidable surface roughness. The breakdown of the stationary modes starts to appear in these ensemble-averaged timeseries at $R = 580, \theta^* = 190 - 230$ degrees. Note that single-realization time series would show the beginnings of breakdown at a lower Reynolds number but ensemble-averaged data show the last remnants of periodicity more easily. The stationary modes are shown here to lose all periodicity at $R = 620 - 630$. Our observed Reynolds number for the breakdown and the entire loss of periodicity is much larger than that of Wilkinson & Malik (1985) and Kobayashi *et al.* (1980).

Here, we show the effect of the edge Reynolds number on the transition Reynolds number in figure 8. The transition Reynolds numbers with different edge Reynolds number and edge conditions are plotted against the edge Reynolds number together with the prediction of of the edge effect by Healey (2010). Our results clearly show the lack of dependence of R_t on these edge conditions and edge Reynolds number, and suggest that Healey's (2010) prediction of a relationship between R_t and R_{edge} (verified by his figure 7(b) using others' values of R_t) is better explained by a recognition that different authors have used different definitions of R_t than by a physical phenomenon.

5. Conclusions

We performed an experimental study to investigate the laminar-turbulent transition process of a rotating-disk flow with different edge conditions and different edge Reynolds numbers. Three different edge conditions were studied and four

different edge Reynolds numbers with each edge condition. Figure 2 shows that there is a dramatic effect on the mean flow within about $3 - 4$ mm of the disk edge hence further measurements were not taken in this region. Figure 4 shows that R_{edge} has no significant effect on the transition process nor on R_t. The results with different edge conditions agree within 10 ΔR. Open type has the largest background noise level compared with the ring and plate types. This is because the eight aluminum components fixing the glass to the aluminum-alloy disk generate a disturbances field with eight oscillations per rotation of the disk. However, we observe that the varying background-noise levels in this study do not affect to the transition process (as suggested by figure 4). Furthermore, this result is reinforced by the PDF maps shown in figure 5, which graphically reveal the transition process described in Imayama *et al.* (2012). The PDF maps showing a superposition of measurements with the four different edge Reynolds numbers are continuous (with one small exception), which indicates that R_{edge} does not affect the transition process significantly.

We define the transition Reynolds number, R_t, as the onset of nonlinearity where the amplitude of harmonics of the primary vortices reach -6 in terms of the ensemble-averaged power spectrum intensity of azimuthal velocity, as shown in figure 6. The transition Reynolds number as a function of the edge Reynolds number is represented in figure 8, showing no dependence, a result that contradicts Healey (2010), where his figure 7(b) predicts R_t increases as R_{edge} approaches R_t. We obtained a transition Reynolds number (using our definition and measured across all the cases listed in figure 8) of $510 \leq R_t \leq 520$.

The onset of nonlinearity is highly repeatable, which is consistent with this nonlinearity not being significantly influenced by the background disturbance field but by the absolute instability found by Lingwood (1995). The variation in the transition Reynolds number reported by previous authors is discussed in § 4, and we suggest is largely a result of varying definitions rather than differing physical phenomena.

We are grateful to the Swedish Research Council (VR) and KTH for support of this research. We also thank the late Dr Tim Nickels who arranged the loan for the experimental apparatus from the University of Cambridge Department of Engineering to KTH.

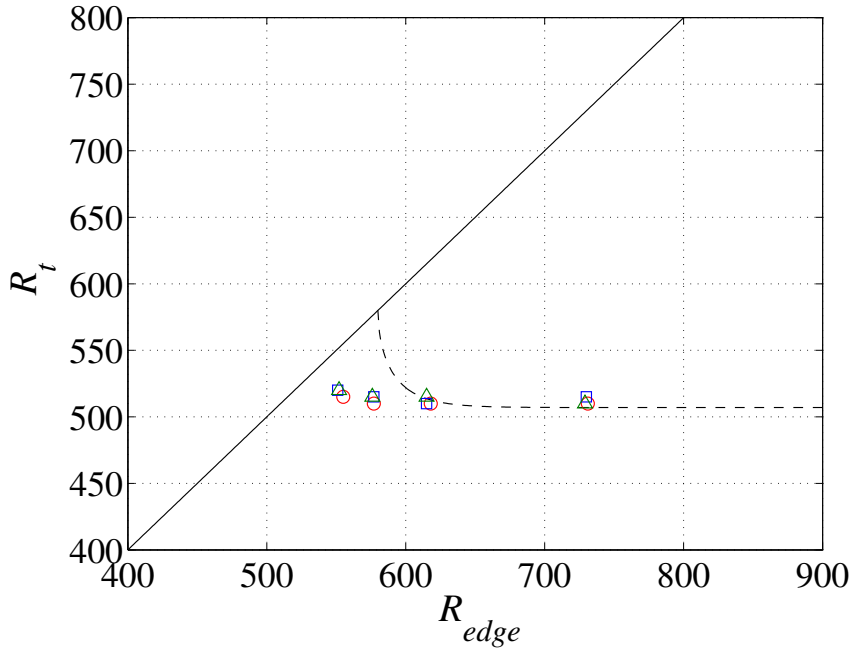

FIGURE 8. Dependence of R_t as defined here on the Reynolds number at the edge of the disk, R_{edge} with different edge conditions, Open type (□), Ring type (△), Plate type (○). Solid line and dashed line represent the boundary of the edge, i.e. where $R_t = R_{edge}$ and the edge effect suggested by a flow model using the linearized complex Ginzburg-Landau equation taken from Healey (2010), respectively.

References

Chin, D.-T. & Litt, M. 1972 An electrochemical study of flow instability on a rotating disk. *J. Fluid Mech.* **54**, 613–625.

Clarkson, M. H., Chin, S. C. & Shacter, P. 1980 Flow visualization of inflexional instabilities on a rotating disk.

Cobb, E. C. & Saunders, O. A. 1956 Heat transfer from a rotating disk. *P. Roy. Soc. Lond. A. Mat.* **236**, 343–351.

Davies, Christopher & Carpenter, Peter W. 2003 Global behaviour corresponding to the absolute instability of the rotating-disc boundary layer. *J. Fluid Mech.* **486**, 287–329.

Fedorov, B. I., Plavnik, G. Z., Prokhorov, I. V. & Zhukhovitskii, L. G. 1976 Transitional flow conditions on a rotating disk. *J. Eng. Phys. Therm.* **31**, 1448–1453.

Gregory, N., Stuart, J. T. & Walker, W. S. 1955 On the stability of three-dimensional boundary layers with application to the flow due to a rotating disk. *Phil. Trans. R. Soc. Lond.* **248**, 155–199.

Gregory, N & Walker, W. S. 1960 Experiments on the effect of suction on the flow due to a rotating disk. *J. Fluid Mech.* **9**, 225–234.

Healey, J. J. 2010 Model for unstable global modes in the rotating-disk boundary layer. *J. Fluid Mech.* **663**, 148–159.

Imayama, S., Alfredsson, P. H. & Lingwood, R. J. 2012 A new way to describe the transition characteristics of a rotating-disk boundary-layer flow. *Phys. Fluids* **24**, 031701.

Johansson, A. V. & Alfredsson, P. H. 1982 On the structure of turbulent channel flow. *J. Fluid Mech.* **122**, 295–314.

von Kármán, T. 1921 Über laminare und turbulent Reibung. *Z. Angew. Math. Mech.* **1**, 233–252.

Kobayashi, R., Kohama, Y. & Takamadate, C. 1980 Spiral vortices in boundary layer transition regime on a rotating disk. *Acta Mech.* **35**, 71–82.

Kohama, Y. 1984 Study on boundary layer transition of a rotating disk. *Acta Mech.* **50**, 193–199.

Lingwood, R. J. 1995 Absolute instability of the boundary layer on a rotating disk. *J. Fluid Mech.* **299**, 17–33.

Lingwood, R. J. 1996 An experimental study of absolute instability of the rotating-disk boundary-layer flow. *J. Fluid Mech.* **314**, 373–405.

Lingwood, R. J. 1997 Absolute instability of the Ekman layer and related rotating flows. *J. Fluid Mech.* **331**, 405–428.

Lingwood, R. J. & Garrett, S. J. 2011 The effects of surface mass flux on the instability of the BEK system of rotating boundary-layer flows. *Eur. J. Mech. B-Fluid.* **30**, 299–310.

Malik, M. R., Wilkinson, S. P. & Orszag, S. A. 1981 Instability and transition in rotating disk flow. *AIAA J.* **19**, 1131–1138.

Othman, H. & Corke, Thomas C. 2006 Experimental investigation of absolute instability of a rotating-disk boundary layer. *J. Fluid Mech.* **565**, 63–94.

Pier, B. 2003 Finite-amplitude crossflow vortices, secondary instability and transition in the rotating-disk boundary layer. *J. Fluid Mech.* **487**, 315–343.

Smith, N. H. 1947 Exploratory investigation of laminar-boundary-layer oscillations on a rotating disk. *NACA TN 1227* .

Theodorsen, T. & Regier, A.A. 1944 Experiments on drag of revolving disks, cylinders and streamline rods at high speeds. *NACA Rep. 793* .

Viaud, B., Serre, E. & Chomaz, J.-M. 2011 Transition to turbulence through steep global-modes cascade in an open rotating cavity. *J. Fluid Mech.* **688**, 493–506.

Wilkinson, S. P. & Malik, M. R. 1985 Stability experiments in the flow over a rotating disk. *AIAA J.* **23**, 588–595.

Paper 3

3

Secondary Instability and Turbulent Breakdown of the Rotating-Disk Flow

By Shintaro Imayama

Linné FLOW Centre, KTH Mechanics, SE-100 44 Stockholm, Sweden

Internal report

The laminar-turbulent transition of the rotating-disk flow is discussed. The exact nature of the laminar-turbulent transition process of the rotating-disk flow is still not well understood. This study has been performed experimentally using hot-wire anemometry across the laminar-turbulent transition region. The fluctuation velocity associated with a secondary instability is characterized as a 'kink' in single-realization timeseries just before the turbulent breakdown region. It is found that the appearance of kinked timeseries becomes less apparent at certain wall-normal heights. The amplitude of the ensemble-averaged timeseries of the fluctuation velocity, which are assumed to correspond to the stationary mode, varies azimuthally probably due to the superposition of multiple disturbance fields. However it seems that the turbulent breakdown of the stationary disturbances does not depend on their amplitude, but may depend on the appearance of a travelling secondary instability. Based on the almost constant transition Reynolds number reported in the literature, the hypothesis is discussed that the secondary instability could be triggered by the primary absolute instability (Lingwood, R.J., *J. Fluid Mech.* **299**, 17–23) and could be absolute unstablely itself.

---

1. Introduction

The laminar-turbulent transition of the rotating-disk flow is discussed. Von Kármán (1921) derived the exact similarity solution of the laminar boundary layer on a rotating disk flow that has a three-dimensional profile with an inflection point in the radial direction. The inflection point in the radial velocity profile satisfies Rayleigh's inflection-point criterion implying that this flow could be inviscidly unstable. Local stability analysis (e.g. Lingwood 1995*a*) shows that the critical Reynolds number of the stationary mode is about $R = 290$, where the Reynolds number is $R = r^*(\Omega^*/\nu^*)^{1/2}$. Here r^* is the radius of the disk at the measurement position, Ω^* is the rotational speed of the disk, ν^* is the kinematic viscosity of the fluid and * denotes a dimensional quantity. This inviscidly unstable mode is called Type I. The flow on the rotating disk is also

be unstable through a viscous mechanism which gives rise to so called Type II mode. However for this mode the stationary disturbances have smaller growth rates than Type I. The maximum growth rate from linear stability theory is for a disturbance travelling slowly relative to the disk rather than the stationary mode (Hussain *et al.* 2011). However as shown in many studies, 28 to 32 spiral vortices are observed, which are stationary in the rotating frame, (e.g. in the flow visualization of Kohama 1984). These are triggered by unavoidable fixed roughnesses on the disk surface which cause continuous, and perhaps larger, stationary excitation of the flow, and therefore the stationary disturbances tend to dominate the observed flow field rather than the travelling one.

Lingwood (1995*a*, 1997) found, using the Briggs's (1964) method with a local linear approximation, a change of instability mechanism from convective instability to absolute instability for certain travelling waves above $R_{CA} = 507$, where R_{CA} is a critical Reynolds number for the absolute instability. Lingwood (1995*b*) showed that the onset of nonlinearity appeared at Reynolds number above 502 and below 514. Furthermore Lingwood (1996) followed the development of the laminar-turbulent transition process from there, finding a fully turbulent flow about $R = 600 - 650$. She illustrated the process through time records of the velocity signal which showed sinusoidal signals up to the point where breakdown was observed without obvious signs in the hot-wire time series associated with secondary instability. Based on these results she stated that for her experiments "the stationary disturbances are sufficiently small, even close to the onset of transition, for the boundary layer stability to be governed by the mean velocity profiles rather than secondary instabilities".

In contrast to Lingwood's (1996) experimental observation, Kobayashi *et al.* (1980), Kohama (1984) and Wilkinson & Malik (1985) observed signs associated with secondary instability just before the turbulent-breakdown region. Kobayashi *et al.* (1980) who carried out the flow visualization on the rotating-disk flow captured "a new striped flow pattern originating along the axis of a spiral vortex". Kohama (1984) who also performed the visualiztion study suggested "ring-like vortices which occur on the surfaces of each spiral vortices [sic]". Furthermore both Kobayashi *et al.* (1980) and Wilkinson & Malik (1985) observed kinked velocity fluctuations at a final stage of the laminar-turbulent transition process. Then Wilkinson & Malik (1985) concluded that "stationary, secondary instabilities between the primary vortices were observed". From the theoretical point of view Balachandar *et al.* (1992) suggested that about 9% of the root-mean-square amplitude of the primary disturbances is required to trigger the secondary instability at $R = 500$ and that the travelling secondary instability appears as a pair of counter-rotating vortices. Lingwood (1996) on the other hand performed the experiments with 'clean' disk conditions resulting in low-amplitude initial stationary disturbances with a peak amplitude of only 3% of the local disk speed at $R = 500$.

Pier (2003) suggested that within a theoretical analysis a *nonlinear* approach is required to explain fully the self-sustained behaviour of the rotating-disk flow. He argued that the rotating-disk boundary layer has not only a primary nonlinear global mode fixed by the local absolute instability, found by Lingwood (1995*a*), but that a secondary absolute instability triggers the transition to turbulence. However, the behaviour of the secondary instability and also its relation to the primary absolute instability are not fully understood as yet.

Imayama *et al.* (2012) performed careful low-disturbance experiments with an unexcited (i.e. with no deliberate excitation) boundary-layer flow on the rotating disk and revealed, using the probability density function (PDF) of azimuthal fluctuation velocities, a wall-normal structure associated, it is suggested, with secondary instability above $R = 570$. This occurred despite the fact that the primary instability is quite small (about 0.6%) at $R = 500$. Furthermore the disturbance growth measurements by Imayama *et al.* (2012) show the onset of nonlinearity at $R = 510$ (associated it is assumed with the appearance of absolute instability) and subsequent laminar-turbulent transition with an exponential growth of disturbances resulting in fully-developed turbulence at $R = 650$. The change of the slope at $R = 545$ in the disturbance growth measurement in their figure 5 could correspond to what Viaud *et al.* (2011) calls a 'secondary front', leading to a cascade of absolutely unstable secondary instabilities and transition to turbulence. These results maybe indicate that even after the appearance of the absolute instability at aroun $R = 507$, the secondary instability has an important role in the turbulent breakdown of the rotating-disk flow.

The exact nature of the laminar-turbulent transition process on the rotating-disk flow is however still not well-understood. The aim of this study is to investigate experimentally the laminar-turbulent transition process including the effect of the absolute instability. In particular the behaviour of a secondary instability and turbulent transition will be discussed.

2. Experimental set-up

The experimental set-up is the same as the one used in Imayama *et al.* (2012). Table 1 shows the experimental conditions in the present work and PP01-PP09 and IP02 are identical data used in Imayama *et al.* (2012). The azimuhtal velocity measurements were performed by hot-wire anemometry. The detail of experimental method has been discussed in Imayama *et al.* (2012). IP01 is azimuthal velocity measurement as a function of Reynolds number performed at a constant height $z = 1.3$ as well as IP02 except the difference with the edge Reynolds number R_{edge}, where z is a non-dimensional height from the wall ($z = z^*(\Omega^*/\nu^*)^{1/2}$) and the R_{edge} is defined as $R_{edge} = r_d^*(\Omega^*/\nu^*)^{1/2}$, where r_d^* is an actual radius of glass disk.

Case	R	R_{edge}	r^*[mm]	Ω^*[rpm]	z
PP01	530	630	198	1040	0.4-16
PP02	550	654	198	1122	0.4-16
PP03	570	677	198	1205	0.4-16
PP04	590	702	198	1295	0.4-26
PP05	610	725	198	1385	0.4-26
PP06	630	749	198	1480	0.4-26
IP01	360-605	618	137-231	1000	1.3
IP02	360-700	731	116-226	1400	1.3

TABLE 1. Experimental conditions.

Case PP01-06 and IP02 are identical data used in Imayama *et al.* (2012). In PP01-06 cases a Reynolds number is changed by varying the rotational speed of the disk, on the other hand, in IP01-02 cases Reynolds number is changed by varying the radius of the hot-wire position. Here, r^* is a local radius of the hot-wire and z is the normalized wall-normal position of the hot-wire, respectively.

3. Results

3.1. *Azimuthal velocity time series*

Imayama *et al.* (2012) observed a wall normal structure of the instantaneous azimuthal fluctuation velocity profile that they associated with the secondary instability, Their observation was based on the variation in the wall normal direction of the probability density function (PDF) of the velocity fluctuations, which showed double peaks that appeared around $R = 550$. Both Kobayashi *et al.* (1980) and Wilkinson & Malik (1985) observed kinks on the sinuousoidal velocity fluctuations just before the turbulent breakdown region and suggested that this was a sign of the secondary instability. However Lingwood (1996) did not observe obvious kinks in her experiment and stated "nothing with the degree of periodicity observed by Wilkinson & Malik (1985)".

To investigate the different behaviour just before the turbulent breakdown region observed by previous authors, figure 1–6 show both single realizations and ensemble-averaged azimuthal velocity time series (averaged over approximately 1000 revolutions) measured at various wall normal heights and Reynolds numbers. Here v is an azimuthal fluctuation velocity (v^*) normalized by the local disk speed ($v = v^*/(r^*\Omega^*)$). The single realization time series contain both time-dependent and time-independent components, made up by both travelling and stationary waves, while the ensemble-averaged time series reveal only the stationary mode if long enough time series are used to form the ensemble-average. Typically the ensemble-average amplitude is smaller than that of the

single realizations, however for some single realizations the opposite is true (see e.g. figure 1(b)).

At $R = 530, 550$ no obvious periodic kinked fluctuation velocity is observed in both the single realization and ensemble averaged time series. Figure 4 in Imayama *et al.* (2012) shows the onset of nonlinearity in the spectrum at $R = 510$ may be triggered by absolute instability (Lingwood 1995*a*). At $R = 530$ it is hard to see the nonlinear effect in the both time series, while at $R = 550$ the distortion of single realizations starts to appear at $\theta^* = 135 - 270°, z = 0.6$, $\theta^* = 135 - 180°, z = 1.3$ and $\theta^* = 90 - 270°, z = 2.0$ where at least five harmonics of the basic frequency in the spectrum at $z = 1.3$, see figure 4 in Imayama *et al.* (2012). At $z = 3.0, R = 550$ skewed single realization and ensemble averaged time series can be observed due to roll up of higher velocity component from near wall region due to primary vortices. This skewed behaviour can be observed in PDF of the azimuthal velocity profile (see figure 7 in Imayama *et al.* 2012).

In figure 3 $R = 570$ and here the instantaneous signals show obvious different behaviour compared with the lower Reynolds number. The amplitude of single realization time series become larger than ensemble-averaged time series and kinked velocity fluctuations appear in single realization time series at all z. However at $z = 1.3$ the kinks are less apparent compared with other heights. Furthermore at $z = 2.0, 3.0$ the kinks are sitting 'backward' on the basic fluctuations, which is opposite to that at $z = 0.6, 1.0$ where they are sitting 'frontward'. Ensemble-averaged time series do not seem to have such kinks, indicating that the kinks are associated with secondary instability, and should be attributed to a travelling mode and not to a stationary one.

At $R = 590$, single realization time series start to have high-frequency components showing the onset of turbulent breakdown at all z and amplitude of the ensemble-averaged time series decreases compared with $R = 570$, a result of turbulent breakdown. The appearance of the kinked velocity signals and subsequent turbulent breakdown agree with previous authors' observations (Kobayashi *et al.* 1980; Wilkinson & Malik 1985).

At $R = 610$ high frequency components almost occupy in the single realizations time series at all z. On the other hand, low frequency components with approximately four oscillations in a revolution appeared in ensemble-averaged time series. Corke *et al.* (2007) suggested the growth of four stationary azimuthal oscillation in a revolution with the largest amplitude just upstream the turbulent transition. This appearance is also captured by flow visualization taken by Kobayashi *et al.* (1980). At $R = 630$ high frequency components are more distinct and amplitude of ensemble-averaged time series becomes smaller at all z resulting the flow changes to turbulence.

Figure 3 presents z dependence of the shape of kinked fluctuation velocity. The kinked velocity fluctuations observed by both Wilkinson & Malik (1985);

Kohama (1984) were measured at $z = 1.77$. Figure 7 shows the single realization azimuthal velocity time series measured at $z = 1.8, R = 570$ which is almost coincident with the wall normal height used by them, showing a similar kinked fluctuation velocity. Lingwood (1996) on the other hand measured at $z = 1.3$ where the kinks are less apparent. Based on these results, there was no clear observation of kinked velocity fluctuations by her may have been due to the measurement height at $z = 1.3$. Although Lingwood (1996) suggested that the laminar-turbulent transition did not appear to be governed by secondary instability but the mean velocity profiles and their absolute instability, a secondary instability may have triggered the turbulent breakdown consistent with the observation of Imayama *et al.* (2012).

However Wilkinson & Malik (1985) and Kobayashi *et al.* (1980) observed the appearance of breakdown of the vortices and the entire loss of periodic velocity fluctuation at much lower Reynolds number. Wilkinson & Malik (1985) observed the breakdown of the vortices at $R = 550$ and Kobayashi *et al.* (1980) presents the entire loss of periodic velocity fluctuation at $R = 566$. Furthermore figure 9 in Kobayashi *et al.* (1980) shows the kinked fluctuation azimuthal velocity at $R = 500$, indicating the possibility that the primary vortices trigger the secondary instability as suggested by Balachandar *et al.* (1992) due to a high initial disturbance environment, namely without absolute instability. However in the present study indications of the secondary instability appear at $R = 570$. The relationship between the various observations of secondary instability and the absolute instability (Lingwood 1995*a*) is still unknown although the shape of the kinked azimuthal fluctuation velocity seems to be similar in reported observations.

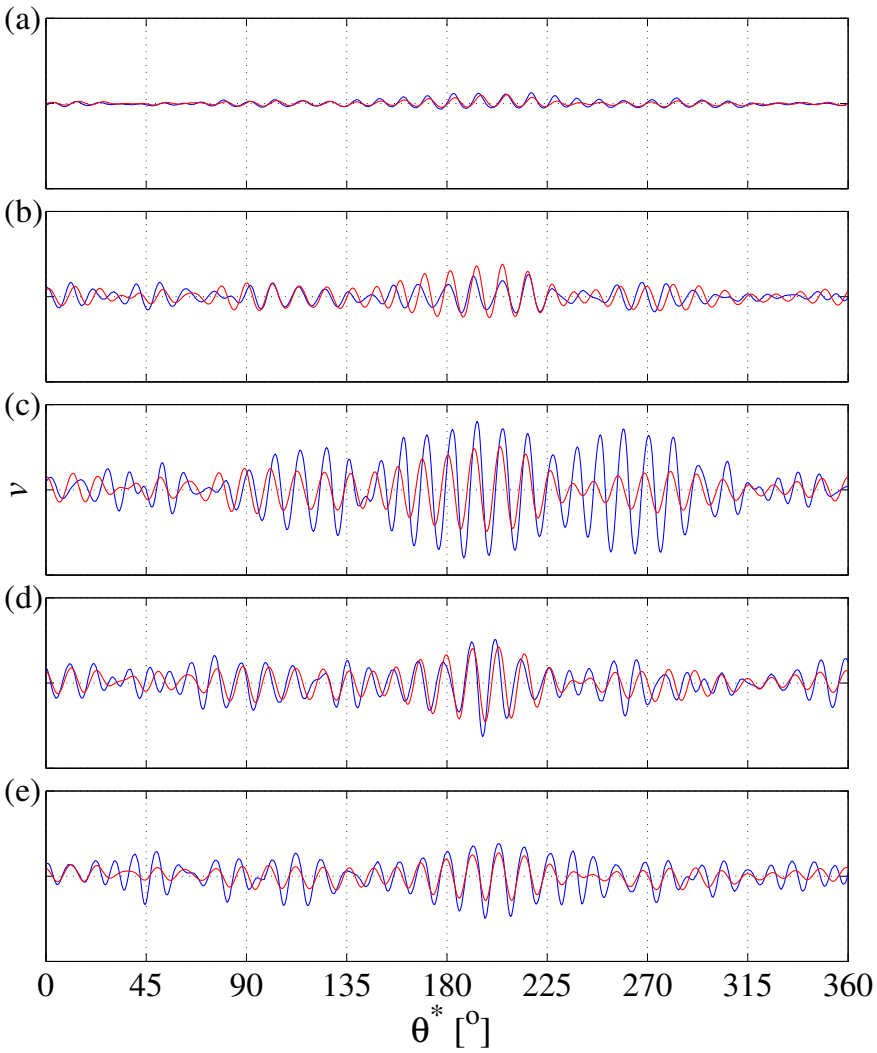

FIGURE 1. A single realization (blue) and ensemble-averaged (red) time series of azimuthal normalized fluctuation velocity at $R = 530$: (a) $z = 3.0$, (b) $z = 2.0$, (c) $z = 1.3$, (d) $z = 1.0$, (e) $z = 0.6$. The range of the ordinate is -0.1 to 0.1 with each 0.1 step for all z.

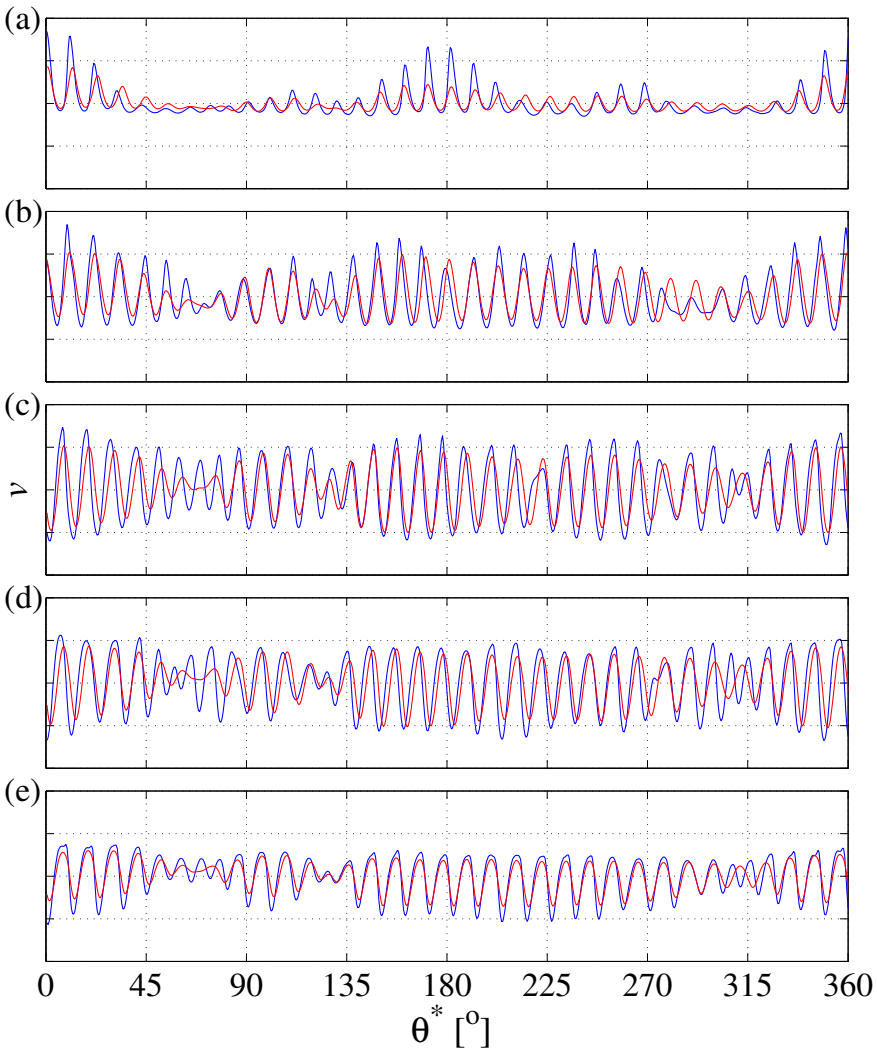

FIGURE 2. A single realization (blue) and ensemble-averaged (red) time series of azimuthal normalized fluctuation velocity at $R = 550$: (a) $z = 3.0$, (b) $z = 2.0$, (c) $z = 1.3$, (d) $z = 1.0$, (e) $z = 0.6$. The range of the ordinate is -0.2 to 0.2 with each 0.1 step for all z.

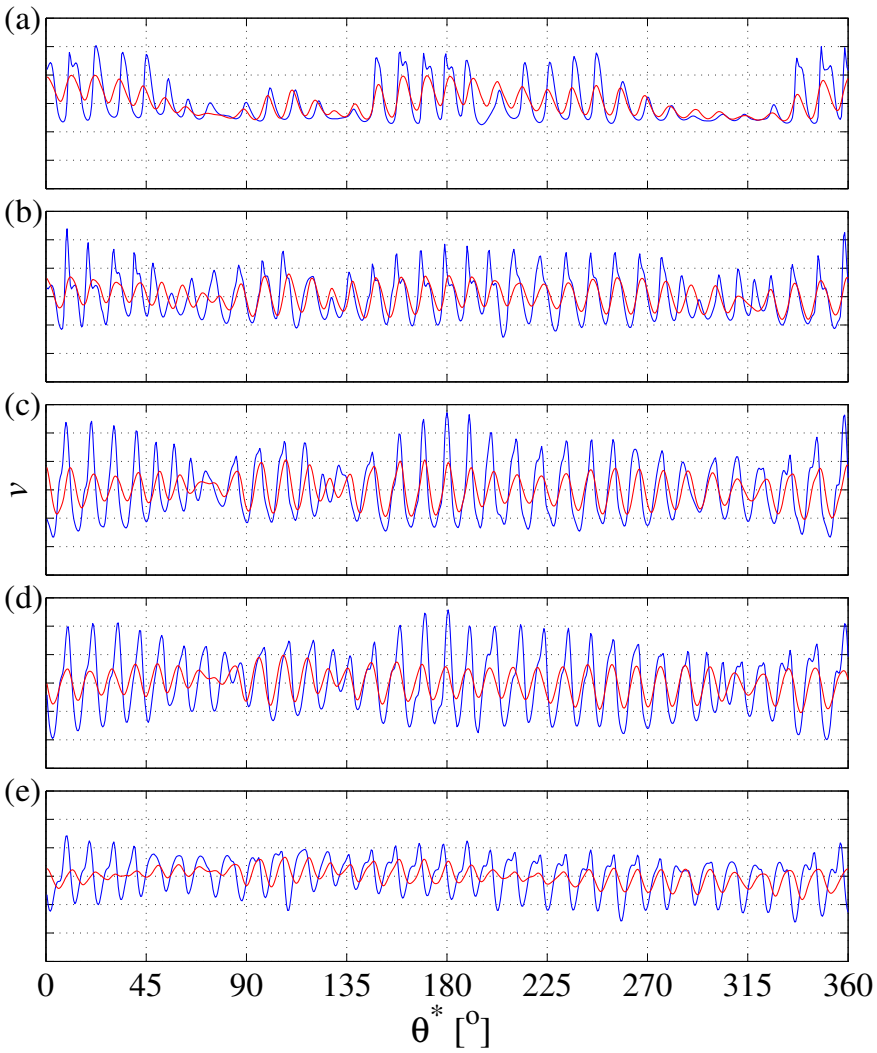

FIGURE 3. A single realization (blue) and ensemble-averaged (red) time series of azimuthal normalized fluctuation velocity at $R = 570$: (a) $z = 3.0$, (b) $z = 2.0$, (c) $z = 1.3$, (d) $z = 1.0$, (e) $z = 0.6$. The range of the ordinate is -0.3 to 0.3 with each 0.1 step for all z.

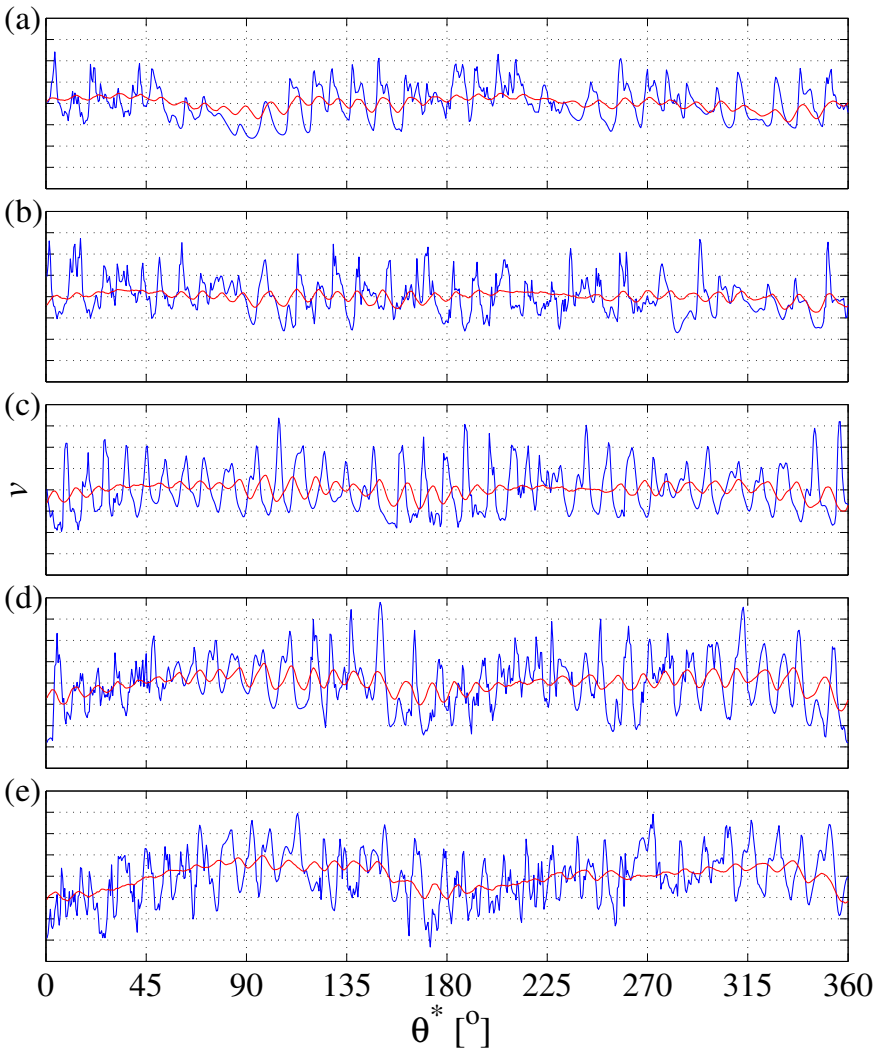

FIGURE 4. A single realization (blue) and ensemble-averaged (red) time series of azimuthal normalized fluctuation velocity at $R = 590$: (a) $z = 3.0$, (b) $z = 2.0$, (c) $z = 1.3$, (d) $z = 1.0$, (e) $z = 0.6$. The range of the ordinate is -0.4 to 0.4 with each 0.1 step for all z.

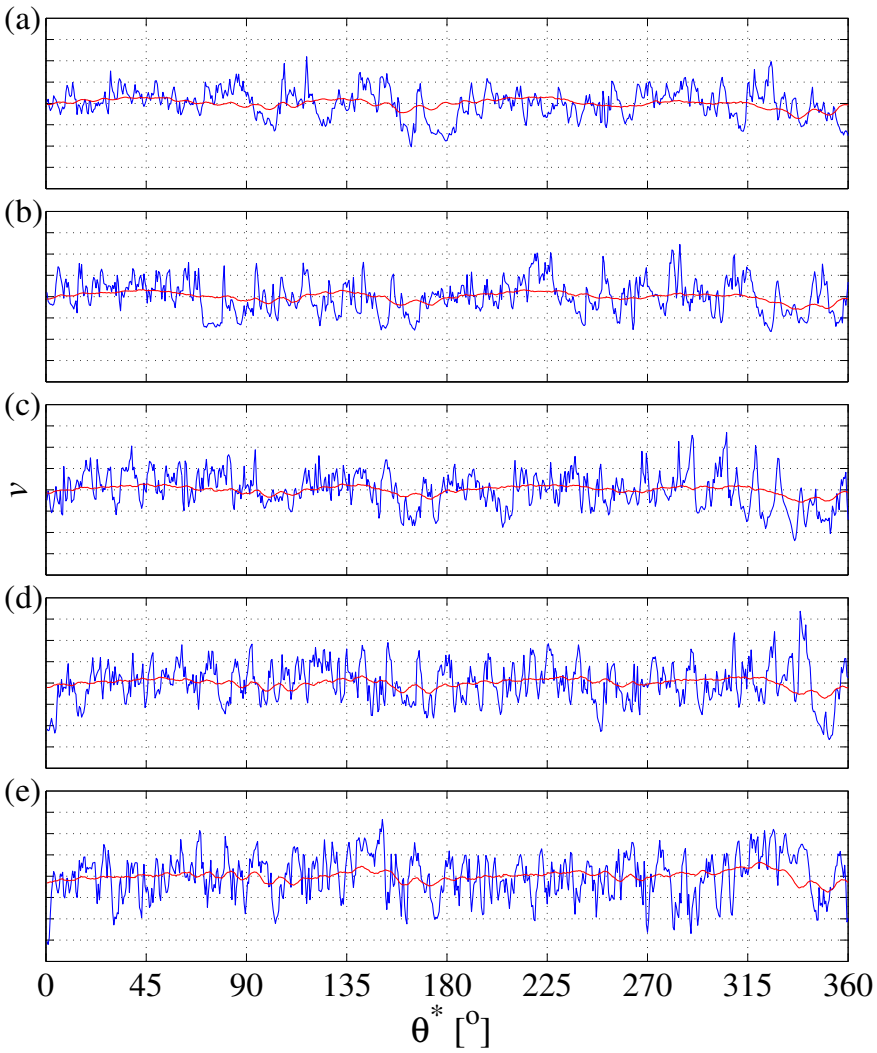

FIGURE 5. A single realization (blue) and ensemble-averaged (red) time series of azimuthal normalized fluctuation velocity at $R = 610$: (a) $z = 3.0$, (b) $z = 2.0$, (c) $z = 1.3$, (d) $z = 1.0$, (e) $z = 0.6$. The range of the ordinate is -0.4 to 0.4 with each 0.1 step for all z.

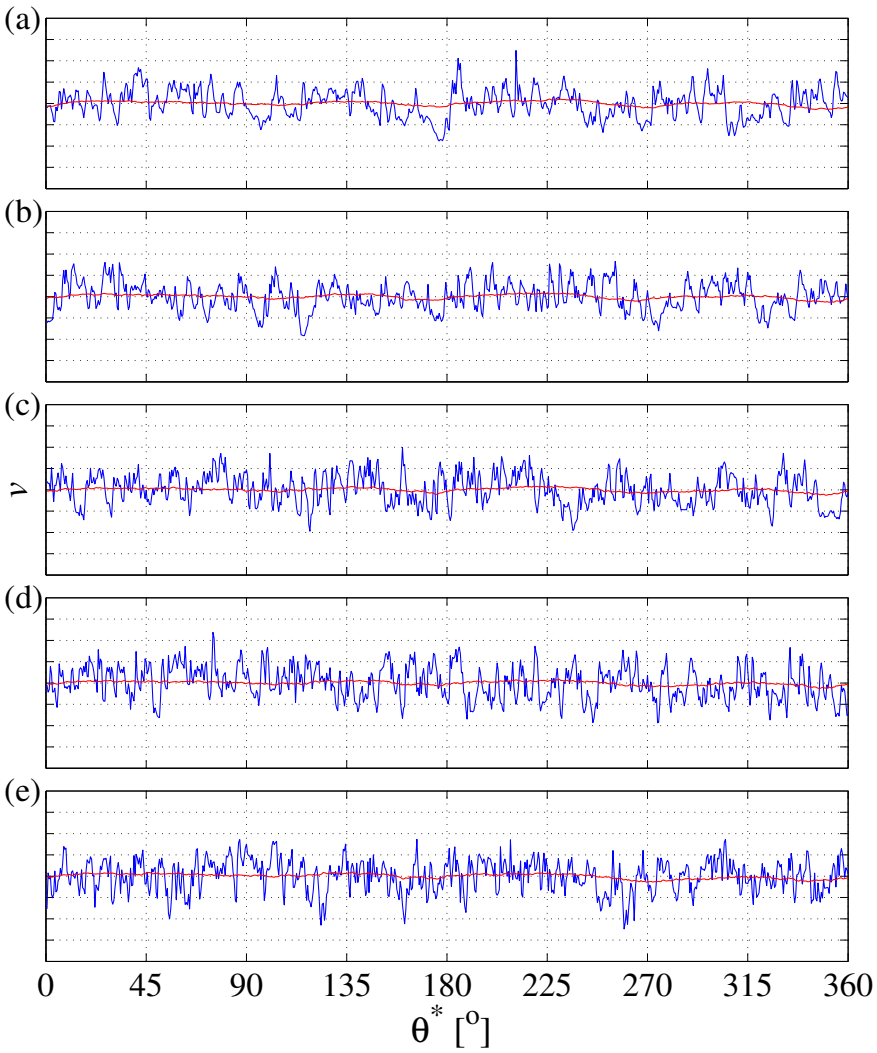

FIGURE 6. A single realization (blue) and ensemble-averaged (red) time series of azimuthal normalized fluctuation velocity at $R = 630$: (a) $z = 3.0$, (b) $z = 2.0$, (c) $z = 1.3$, (d) $z = 1.0$, (e) $z = 0.6$. The range of the ordinate is -0.4 to 0.4 with each 0.1 step for all z.

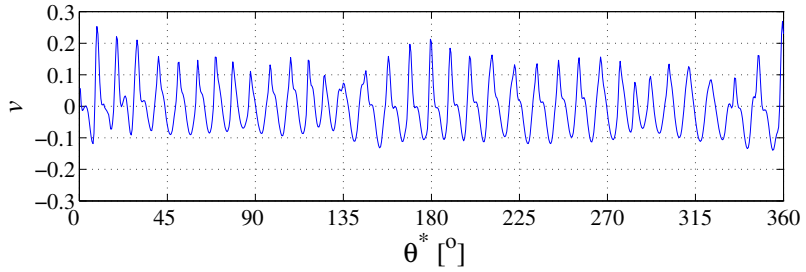

FIGURE 7. A single realization azimuthal normalized fluctuation velocity time series at $z = 1.8$, $R = 570$.

3.2. *Disturbance growth*

Single realizations and ensemble-averaged time series show different characteristic at increasing Reynolds number in figure 1–6. Here to investigate the disturbance growth of both components, the growth of the non-dimensional intensity of the azimuthal velocity fluctuation ($v_{rms} = v^*_{rms}/(r^*\Omega^*)$) is measured as a function of Reynolds number at constant wall normal heights $z = 1.3$, because v_{rms} has maximum value in the unstable region at around this height (see figure 3 in Imayama *et al.* 2012). Figures 8, 9 present disturbance growth of non-dimensional instantaneous azimuthal velocity fluctuations (v^2_{rms}), non-dimensional velocity fluctuation of ensemble-averaged time series $v_{rms,en}$ and non-dimensional velocity fluctuation of the time-dependent part of the time series $v_{rms,td}$ as a function of Reynolds number. Here the $v_{rms,td}$ is obtained as

$$v_{rms,td} = \sqrt{v^2_{rms} - v^2_{rms,en}}\ . \tag{1}$$

If an ensemble is large enough to get rid of time-dependent components in the average, $v_{rms,en}$ becomes the (non-dimensional) azimuthal velocity fluctuation amplitude of the stationary mode $v_{rms,st}$. In a similar way, $v_{rms,td}$ becomes the amplitude of the travelling mode $v_{rms,tr}$. In the present work the ensemble is assumed to be sufficiently large (of the order of 1000 revolutions of the disk. i.e. members of the ensemble).

The variation of v_{rms} as a function of Reynolds number shown in figure 9 and has been discussed in figure 5 in Imayama *et al.* (2012). The growth of $v_{rms,st}$ also shows almost same behaviour as v_{rms} up to $R = 550$. However at around $R = 550$ the growth of $v_{rms,en}$ is saturated and it does not grow further. This is maybe because at $R = 550$ strong non-linearity makes energy flow through a cascade process from the primary vortices to smaller scales as shown in figure 4 in Imayama *et al.* (2012), thereby both limiting the growth of the primary vortices as well as 'scrambling' them.

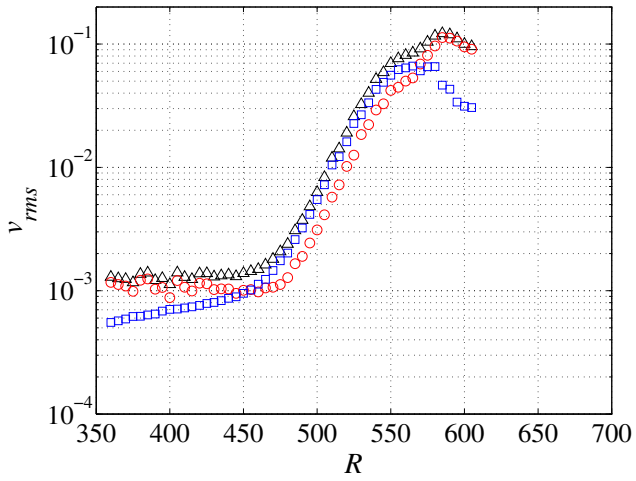

FIGURE 8. v_{rms} (△), $v_{rms,en}$ (□), $v_{rms,td}$ (○) variances measured at $z = 1.3, R_{edge} = 618$ as a function of Reynolds number (IP01).

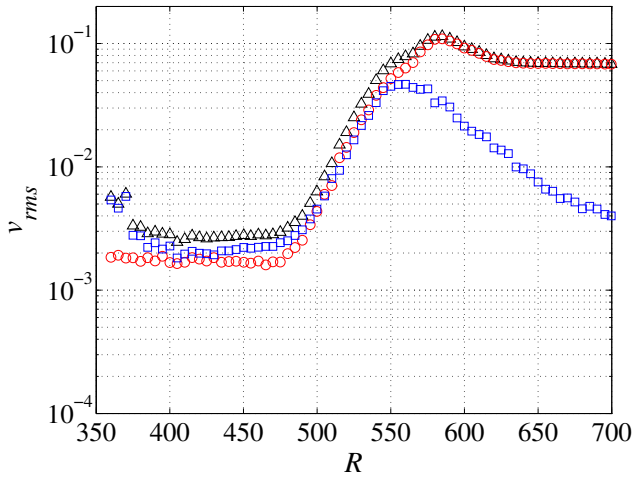

FIGURE 9. v_{rms} (△), $v_{rms,en}$ (□), $v_{rms,td}$ (○) variances measured at $z = 1.3, R_{edge} = 731$ as a function of Reynolds number (IP02).

This Reynolds number where the growth of $v_{rms,en}$ is saturated almost corresponds to the change of the slope in v_{rms}. $v_{rms,en}$ has an almost constant

amplitude between $R = 550$ and $R = 580$ and start to decrease beyond $R \approx 580$. Thus the reason that the slope of disturbance growth in v_{rms} at $R = 545$ is mainly due to the change of disturbance growth of the stationary mode. The decay of $v_{rms,en}$ can be considered as the turbulent breakdown of the stationary mode. On the other hand, $v_{rms,td}$ continues to grow up to $R = 580$. Figure 8 also show a similar trend of each disturbance growth at different edge Reynolds number.

Previous experimental studies (e.g. Gregory *et al.* 1955; Wilkinson & Malik 1985; Kobayashi *et al.* 1980) reveals between 28 and 32 stationary vortices sitting on a disk. Furthermore Wilkinson & Malik (1985) suggested that the number of stationary vortices increases with increasing Reynolds number. Figure 4 in Imayama *et al.* (2012) also shows the peaks around non-dimensional frequency $\omega^*/\Omega^* = 30$ in the spectrum. Thus the variation of $v_{rms,st}$ means the growth of these stationary vortices. To investigate the detail of the disturbance growth of the stationary mode, normalized peak amplitudes ($v_{peak} = v^*_{peak}/(r^*\Omega^*)$) of each stationary vortex are plotted in figures 10 and 11 as a function of Reynolds number. Each vortex grows exponentially but at different amplitudes up to $R = 550$. This different amplitude of each stationary vortex is due to the different level of initial disturbance and this initial environment dependence seems that the instability of the stationary mode has a convective behaviour beyond the onset of absolute instability at $R_{CA} = 507$ in a certain travelling mode. As increasing Reynolds number the appearance of new stationary vortex can be observed at $R = 540, 555$ in figure 10. At $R = 550$ most of stationary vortex stops its growth and maintain its amplitude up to $R = 575 - 580$. Subsequently most of stationary vortices start to decay at the Reynolds number which means the onset of turbulent breakdown of the stationary mode. Based on these facts it seems that the turbulent breakdown of stationary vortices is not triggered by the amplitude of the stationary vortices. At $R = 570$ in figure 3 the kinked fluctuation velocity associated with secondary instability is observed not in the ensemble-averaged time series but in the single realization time series, indicating that the secondary instability may consist of travelling waves. Then perhaps it is implied that the breakdown of stationary vortices is triggered by the travelling secondary instability instead of their amplitude.

4. Conclusions

The laminar-turbulent transition of the rotating-disk flow has been investigated experimentally, in particular, with respect to secondary instability and the turbulent breakdown region using hot-wire anemometry in a low disturbance environment. Single-realization and ensemble-averaged timeseries of azimuthal fluctuation velocity are shown. Kinked fluctuation azimuthal velocity associated with secondary instability is observed here (more prevalently at some wall-normal positions than others) in single-realization timeseries above R =

570, which corresponds to previous experimental observations of Kobayashi *et al.* (1980) and Wilkinson & Malik (1985). However, at $z = 1.3$ the kinked fluctuation velocity is less apparent than at other wall-normal positions, which may explain Lingwood's (1996) lack of observation of such features in her measurements at this wall-normal position. On the other hand, Kobayashi *et al.* (1980) and Wilkinson & Malik (1985) measured the azimuthal velocity fluctuation at $z = 1.77$ where we find that the kinked fluctuation velocity often appears. Ensemble-averaged fluctuation-velocity timeseries do not seem to feature kinks, indicating that the secondary instability is a travelling wave (which is therefore averaged away by the periodic ensembling process).

The growth of the instantaneous, ensemble-averaged and time-dependent velocity fluctuations as functions of Reynolds number have been investigated. The exponential growth shown by ensemble-averaged velocity fluctuations saturates at $R = 550$, plateaus for $R = 580 - 585$, and is followed by the turbulent breakdown of the stationary mode beyond that Reynolds number. More detail on the variation between single realizations making up the ensemble-averaged timeseries has been shown as a variance of the normalized peak amplitude of each stationary vortex. Each stationary vortex grows exponentially but with different amplitude up to $R = 550$, showing a convective behaviour. However the turbulent breakdown of each stationary vortex seems to be independent of its amplitude, which suggests this turbulent breakdown process is not due to its convectively behaviour. Just before the turbulent breakdown of the stationary mode, travelling secondary instabilities are observed at $R = 570$.

These facts may indicate that the turbulent breakdown of the stationary mode is triggered by the appearance of a travelling secondary instability. If so, based on the fact of almost constant transition Reynolds number observed experimentally in previous studies (e.g. Kobayashi *et al.* 1980; Malik *et al.* 1981; Wilkinson & Malik 1985; Lingwood 1996; Othman & Corke 2006), under conditions of low enough initial disturbances, the secondary instability itself could have, as theoretically suggested by Pier (2003), an absolute instability. However, the onset of the transition is either fixed by the primary absolute instability found by Lingwood (1995*a*), or it may be triggered by the primary absolute instability. We suggest that the travelling secondary instability controls the breakdown of the stationary mode and determines the turbulent breakdown as a whole.

This work is supported by the Swedish Research Foundation (VR) and the Linné FLOW Centre. Rebecca Lingwood and P. Henrik Alfredsson are acknowledged for useful discussions.

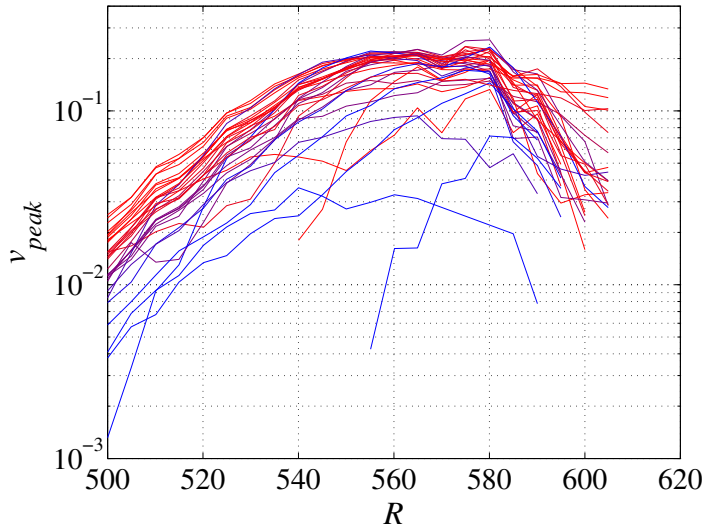

FIGURE 10. The normalized peak intensity v_{peak} of each stationary vortex at $R_{edge} = 618$ (IP01). The colour indicates the initial amplitude (0.006(Blue) $< v_{peak} <$ 0.016(Red)) at $R = 500$ or when new vortex appears.

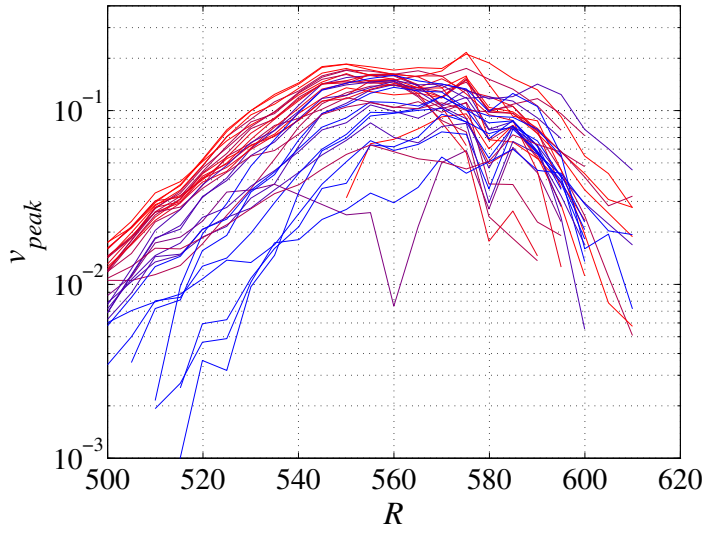

FIGURE 11. The normalized peak intensity v_{peak} of each stationary vortex at $R_{edge} = 731$ (IP02). The colour is the same as in figure 10.

References

Balachandar, S., Streett, C. L. & Malik, M. R. 1992 Secondary instability in rotating-disk flow. *J. Fluid Mech.* **242**, 323–347.

Briggs, R. J. 1964 *Electron-stream interaction with plasmas*. MIT Press.

Corke, T. C., Matlis, E. H. & Othman, H. 2007 Transition to turbulence in rotating-disk boundary layers—convective and absolute instabilities. *Journal of Engineering Mathematics* **57**, 253–272.

Gregory, N., Stuart, J. T. & Walker, W. S. 1955 On the stability of three-dimensional boundary layers with application to the flow due to a rotating disk. *Phil. Trans. R. Soc. Lond.* **248**, 155–199.

Hussain, Z., Garrett, S. J. & Stephen, S. O. 2011 The instability of the boundary layer over a disk rotating in an enforced axial flow. *Physics of Fluids* **23** (11), 114108.

Imayama, S., Alfredsson, P. H. & Lingwood, R. J. 2012 A new way to describe the transition characteristics of a rotating-disk boundary-layer flow. *Phys. Fluids* **24**, 031701.

von Kármán, T. 1921 Über laminare und turbulent Reibung. *Z. Angew. Math. Mech.* **1**, 233–252.

Kobayashi, R., Kohama, Y. & Takamadate, C. 1980 Spiral vortices in boundary layer transition regime on a rotating disk. *Acta Mechanica* **35**, 71–82.

Kohama, Y. 1984 Study on boundary layer transition of a rotating disk. *Acta Mechanica* **50**, 193–199.

Lingwood, R. J. 1995*a* Absolute instability of the boundary layer on a rotating disk. *J. Fluid Mech.* **299**, 17–33.

Lingwood, R. J. 1995*b* Stability and Transition of the Boundary Layer on a Rotating Disk. Phd thesis, Cambridge Unniversity.

Lingwood, R. J. 1996 An experimental study of absolute instability of the rotating-disk boundary-layer flow. *J. Fluid Mech.* **314**, 373–405.

Lingwood, R. J. 1997 Absolute instability of the Ekman layer and related rotating flows. *J. Fluid Mech.* **331**, 405–428.

Malik, M. R., Wilkinson, S. P. & Orszag, S. A. 1981 Instability and transition in rotating disk flow. *AIAA J.* **19**, 1131–1138.

Othman, H. & Corke, T. C. 2006 Experimental investigation of absolute instability of a rotating-disk boundary layer. *J. Fluid Mech.* **565**, 63–94.

Pier, B. 2003 Finite-amplitude crossflow vortices, secondary instability and transition in the rotating-disk boundary layer. *J. Fluid Mech.* **487**, 315–343.

Viaud, B., Serre, E. & Chomaz, J.-M. 2011 Transition to turbulence through steep global-modes cascade in an open rotating cavity. *J. Fluid Mech.* **688**, 493–506.

Wilkinson, S. P. & Malik, M. R. 1985 Stability experiments in the flow over a rotating disk. *AIAA J.* **23**, 588–595.

Paper 4

4

An Experimental Study of a Rotating-Disk Turbulent Boundary-Layer Flow

By Shintaro Imayama[1], R. J. Lingwood[1,2] & P. Henrik Alfredsson[1]

[1]Linné FLOW Centre, KTH Mechanics, SE-100 44 Stockholm, Sweden
[2]University of Cambridge, Cambridge, CB23 8AQ, UK

Internal report

The turbulent boundary layer on a rotating disk in otherwise quiescent fluid is discussed. The turbulent boundary layer has a three-dimensional shape with an inflection point in the radial velocity component. The aim of this study is to give the statistical description of the rotating turbulent boundary layer and also to compare it with a two-dimensional flat-plate boundary layer. A special challenge is to determine the wall friction velocity accurately and here this is done through direct measurement of the velocity distribution close to the rotating disk in a very thin viscous sublayer. We use hot-wire anemometry for the velocity measurements and compared to other flow cases the rotating disk has the advantage of having the highest relative velocity at the wall itself (if the hot-wire probe is in the laboratory frame of reference), thereby limiting the effect of heat conduction to the wall from the hot-wire probe. Here the friction velocity is determined directly from the azimuthal velocity profile in the viscous sublayer and the turbulent statistics from the rotating boundary layer are presented and compared with similar statistics from two-dimensional boundary layers. This study is still ongoing and the results should be viewed as preliminary.

---

1. Introduction

On a rotating disk, in otherwise still fluid, a boundary layer forms that has a three-dimensional velocity profile and where fluid is transported both azimuthally with the disk as well as outwards in the radial direction. An exact similarity solution for the laminar boundary layer, first reported by von Kármán (1921), can be found for an infinite disk rotating in an otherwise quiescent fluid. This boundary layer has the property that the thickness is constant, independent of radius. On the one hand the laminar-turbulent transition process has been addressed, both experimentally and theoretically, in many studies (e.g. Gregory *et al.* 1955; Kobayashi *et al.* 1980; Kohama 1984; Lingwood 1995,

1996; Davies & Carpenter 2003; Pier 2003; Imayama *et al.* 2012). On the other hand, only few experimental studies of the turbulent boundary-layer on the rotating-disk have been made, (see Littell & Eaton (1994) and references therein), despite both the fundamental interest in three-dimensional turbulent boundary layers as well as from their technical applications (e.g. rotor-stator systems, see Crespo del Arco *et al.* 2005). In the following we will denote the turbulent boundary layer on the rotating disk as the von Kàrmàn turbulent boundary layer and abbreviate it as vKTBL. As usual it is a non-dimensional Reynolds number that determines whether the flow is laminar or turbulent and in this case the Reynolds number R is defined as $R = r^*(\Omega^*/\nu^*)^{1/2}$, where r^* is the radius of the disk at the measurement position, Ω^* is the rotational speed of the disk, ν^* is the kinematic viscosity of the fluid and * denotes a dimensional quantity.

Some early work of the drag exerted by turbulent flow on rotating disks was undertaken by Goldstein (1935). Theodorsen & Regier (1944) also performed measurements of drag on"revolving disks" but in addition measured the azimuthal velocity profile using hot-wire anemometry. With the hot wire they measured mean velocity profiles both in the laminar, transitional and turbulent regions up to about $R = 2600$. In contrast to the laminar boundary layer the turbulent boundary layer thickness was shown to increase in the radial direction and they found good agreement of the velocity profile with the 1/7 power law.

Cham & Head (1969) performed radial and azimuthal velocity profile measurement of the vKTBL with a Pitot tube as well as entrainment measurement. They concluded that the azimuthal distribution is closely approximated by a two-dimensional family of boundary-layer profiles suggested by Thompson (1965) and the radial velocity profiles by the a crossflow model by Mager (1952). They also estimated the azimuthal local skin-friction coefficient using the Clauser (1954) plot, resulting in "realistic" values. Erian & Tong (1971) performed experiments and concluded that "the eddy viscosity in the turbulent boundary layer generated by the disk rotation is substantially larger than that of the turbulent boundary layer over a flat plate". The vKTBL experiments by Littell & Eaton (1994) showed that the radial mean velocity component was at most 10% of the azimuthal one. They also concluded that the main difference from the two dimensional turbulent boundary layer (2DTBL) was the lack of a wake component in the mean profile and stated that "the cause of the lack of a wake is unclear".

In order to scale the mean and fluctuating velocity with inner variables, the friction velocity used in the above studies was obtained by classical empirical methods based on the knowledge of 2DTBL. However Nagib & Chauhan (2008) shows that the von Kármán constant κ which is one of the coefficients for the logarithmic law in the turbulent boundary layer may change its value depending not only on Reynolds number but also on the flow system (e.g. different

values are suggested for boundary layers, pipes and channels). To accurately evaluate the turbulent statistics normalized by the inner variables, an accurate determination of the skin friction is required. Nagib *et al.* (2004) suggests that "oil film interferometry technique is the most reliable method for accurate and direct measurement of mean skin friction ($\sim 1.5\%$)". However this technique is not applicable on the rotating disk.

Hot-wire measurement in the viscous sublayer of turbulent boundary-layer flows (e.g.flat-plate boundary layers, pipes and channels) gives in general errors in the near-wall region due to the heat transfer from the hot-wire probe to the wall. However hot-wire measurement of the azimuthal turbulent rotating-disk velocity profile has a maximum azimuthal velocity at the wall in the laboratory frame of reference. This means that heat conduction from the wall to the probe becomes relatively small compared with heat convection and direct measurement of the skin-friction velocity using hot-wire anemometry becomes possible as does evaluation of accurate turbulent statistics in the near-wall region. Furthermore Alfredsson *et al.* (2011) proposed a new way to evaluate the skin-friction velocity using a hot-wire probe and the similarity of the cumulative distribution function (CDF) of the velocity profiles in the near-wall region for canonical flows. This method also allows evaluation of heat-transfer effects.

The aim of the present study is to evaluate the turbulence statistics of the vKTBL using both inner and outer variables. To do so efforts have been put on the direct determination of the skin-friction velocity using hot-wire anemometry measurement of the velocity distribution in the viscous sublayer. It will be shown that close to the wall the boundary-layer statistics are comparable to those of 2DTBL whereas the outer region shows distinct differences.

2. Experimental Set-up

2.1. *Overview*

The experimental set-up is an identical with the one used by Imayama *et al.* (2012), see figure 1, and only a short description is given here. On the original aluminum-alloy disk a new disk made of glass with a thickness of 24 mm and a diameter of 474 mm has been mounted. The aluminum-alloy disk is connected to a DC-servo motor via a vertical shaft, and a pressurized air bearing ensures that the vibrations of the disk are small. The surface of the glass disk is polished resulting in a surface roughness of less than 1 μm and the rotational imbalance is less than 10 μm at the edge and smaller at the centre region of the glass disk. A non-rotational extended annular plate made of wood with an outside diameter of 900 mm is mounted around the glass disk. This extension plate eliminates the effects of the eight aluminum clamps fixing the glass plate and also reduces the effects of noise coming from the air bearing and DC-servo motor. The horizontal gap between the disk and plate is less than 1 mm and vertically the disk surface and plate are approximately flush.

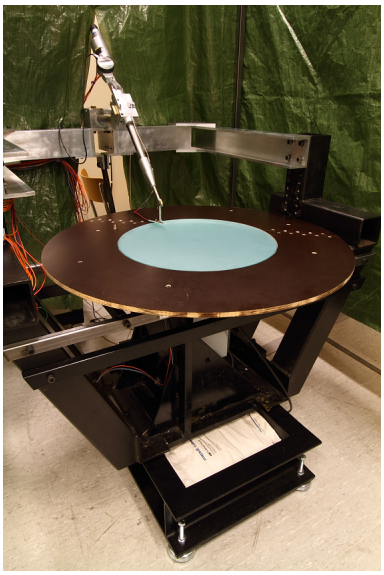

FIGURE 1. The experimental set-up of the rotating disk.

A hot-wire probe with a single sensor made of platinum, with a diameter of 1 μm and 0.3 mm in length, is operated by a constant-temperature anemometer (CTA) with an overheat ratio of 0.8. The sensing element of the hot-wire is oriented in the radial direction, making it mainly sensitive to the azimuthal velocity. The signal from the CTA is digitized using a 16-bit A/D converter at a sampling rate of 2880 data points per disk revolution during a 60 second sampling time. The hot-wire probe is mounted on a two-axis, remotely-controlled traverse mechanism at 45° to the vertical to limit disturbance of the incoming downward axial flow.

The experimental conditions for the present work are shown in table 1. Here the boundary layer thickness δ^*_{99} is defined as the position where the azimuthal velocity reaches 1% of the disk velocity, V_w. The displacement thickness δ^*_1 is defined as

$$\delta^*_1 = \int_0^\infty \frac{V^*(z^*)}{V^*_w} dz^*, \tag{1}$$

where V^*_w is the local disk velocity and z^* is the wall normal height of the hot-wire probe from the disk. The momentum thickness δ^*_2 is defined as

$$\delta^*_2 = \int_0^\infty \left(1 - \frac{V^*(z^*)}{V^*_w}\right) \frac{V^*(z^*)}{V^*_w} dz^*. \tag{2}$$

The shape factor H is defined as $H = \delta^*_1/\delta^*_2$. The Reynolds number based

on the friction velocity v_τ^* is defined as $Re_\tau = v_\tau^* \delta_{99}^* / \nu^*$, and the Reynolds number based on the momentum thickness is defined as $Re_\theta = V_w^* \delta_2^* / \nu^*$. We also introduce an outer length scale, the so called Rotta-Clauser boundary-layer thickness defined as $\Delta^* = \delta_1^* V_w / v_\tau^*$.

The viscous length and time units are defined as $\ell^* = \nu^* / v_\tau^*$ and $t^* = \nu^* / v_\tau^{*2}$, respectively, whereas superscript $^+$ denotes non-dimensionalisation with the viscous units. $\Delta t^* = 1/f_s^*$ is the time between samples, with f_s^* being a sampling frequency.

Imayama *et al.* (2012) suggested that a fully-developed turbulent rotating-disk boundary layer is seen for $R > 650$. The experimental conditions were selected at two different Reynolds number beyond the threshold to have a fully-developed turbulent flow.

2.2. *Calibration of the hot wire*

The calibration of the hot wire is carried out on the rotating disk using the laminar profile changing the radial position and wall-normal height of the hot-wire probe as well as the rotational speed of the disk. There is a principal difference from similar calibration within the boundary layer over a stationary plate, where the smallest velocity is at the plate itself and the highest in the freestream; for the rotating plate the opposite is true. The procedure requires that the absolute wall-normal distance of the hot wire from the disk to be known accurately. The height of the hot wire is determined by taking a photograph of the hot wire together with a precision gauge block with a thickness of 1.000 mm utilizing the reflection of the sensor in the glass plate. A typical image captured from the front of the hot wire by a camera with micro lens is shown in figure 2. However in the turbulent boundary-layer flow the velocity exceeds the range of the calibration due to the high velocities close to the rotating disk. An extrapolated calibration data point is added as the maximum calibration datum using the azimuthal velocity of the disk. Figure 3 shows the variation of the anemometer output voltage close to the disk surface. The voltage at the disk is estimated by a linear extrapolation of the data points.

At the wall the local disk speed is already known so that figure 4(a) shows the hot-wire calibration points obtained from the laminar profile plus the extra datum point. This procedure allows calibration of the hot-wire probe over a broad velocity range without using an external calibration apparatus. The accuracy of this scheme can be tested *a posteriori* when measurements are made in the near wall region, where velocity fluctuations give instantaneous values that are higher than the calibration points.

The calibration data points are fitted by a fourth-order polynomial given as

$$V^* = a_0 + a_1 E^* + a_2 E^{*2} + a_3 E^{*3} + a_4 E^{*4}, \tag{3}$$

Case	R	Re_τ [-]	Re_θ [-]	r^* [mm]	V_w^* [m/s]	δ_{99}^* [mm]	δ_1^* [mm]	δ_2^* [mm]	H [-]	v_τ^* [m/s]	c_f [-]	ℓ^* [μm]	L^+ [-]	Δt^+ [-]
T01	668	885	1714	210	32.0	9.3	1.08	0.81	1.34	1.43	0.00399	10.5	28.6	1.96
T02	698	1011	1935	220	33.5	10.4	1.16	0.87	1.33	1.46	0.00380	10.3	29.2	2.05
2D01		492	1420						1.43		0.00388			
2D02		974	3032						1.40		0.00319			

TABLE 1. Experimental conditions and DNS data used in the present study. T01 and T02 are the two experimental profiles for the vKTBL used in the present study. 2D01 and 2D02 are profiles for a 2DTBL flow taken from Schlatter & Örlü (2010). For the experiments the rotational speed for T01, T02 is $\Omega^* = 1455$ rpm. The skin friction is defined as $c_f = 2(v_\tau^*/V_w^*)^2$ for the vKTBL and $c_f = 2(u_\tau^*/U_\infty^*)^2$ for the 2DTBL.

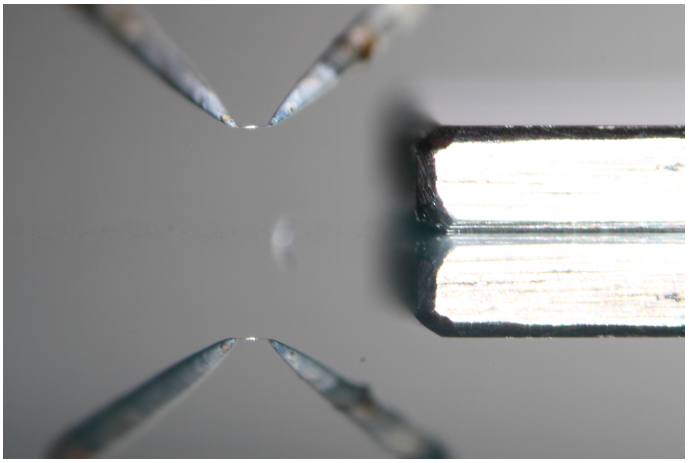

FIGURE 2. Typical calibration photograph to determine the position of the hot wire (left side in the image) using a precision gauge block with 1.000 mm thickness (right side in the image). The upper half-plane shows the real objects and the reflections in the glass surface in the lower half-plane.

where V^* is a mean azimuthal velocity, E^* is a mean output voltage from the anemometer and $a_0 - a_4$ are the coefficients of the polynomial approximation. Figure 4(b) shows the deviations of the calibration data points from the polynomial fitting. The deviation is less than $\pm 1\%$ except in the low velocity region ($V* < 0.5$ m/s).

3. Results and discussion

The following chapter is divided into four parts. First we discuss the near-wall measurements and the procedure to obtain the skin-friction velocity. Secondly we discuss the mean velocity profile and the turbulence intensity. In a third part we discuss the higher moments (i.e. skewness and flatness) and finally we show some spectral maps. We show data for two Reynolds numbers taken at two radial position and at two different wall velocities (32.0 and 33.5 m/s, respectively). The Reynolds numbers for these two stations are however quite similar, and the inclusion of both of them is mainly to get an indication of the accuracy (or rather repeatability) of the measurements. For the turbulence statistics we compare with two-dimensional turbulent boundary-layer data at approximately the same Reynolds numbers. Here we use DNS data that have been extensively verified by experiments (Schlatter & Örlü 2010) and the DNS database has the advantage that a range of Reynolds numbers is available. We chose two Reynolds numbers from the simulation, one which has a similar

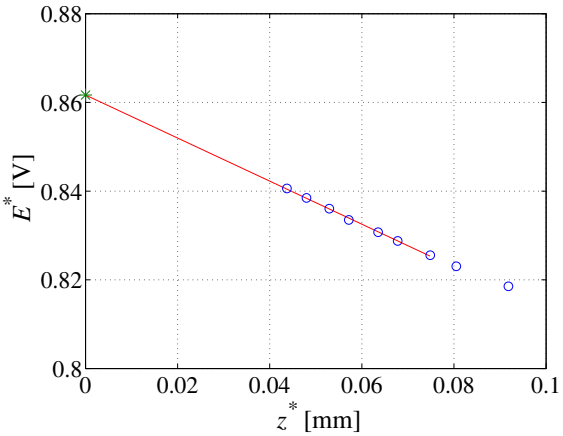

FIGURE 3. The highest velocity of the calibration curve is estimated by extrapolating the anemometer voltage to the wall. The local radius is $r^* = 210$ mm and the rotational speed is $\Omega^* = 1455$ rpm. Then the local disk speed V_w^* reaches 32 m/s.

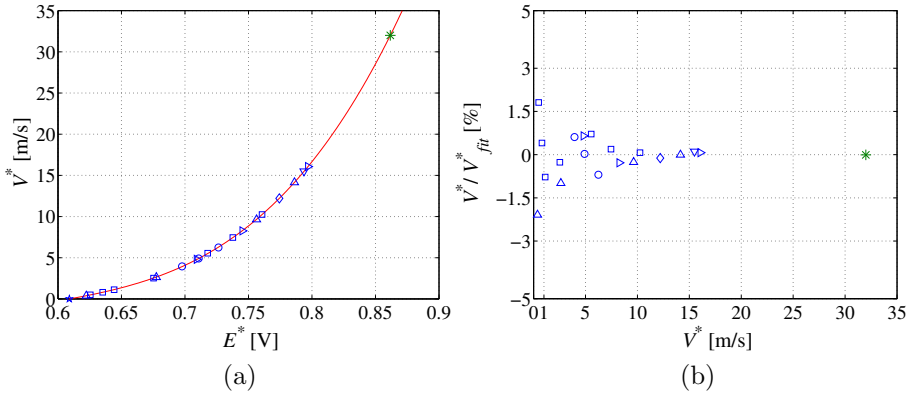

FIGURE 4. (a) The calibration curve with the extrapolated point given as $*$. (b) The scatter between the relation 3 and the calibration points.

skin-friction coefficient to our experiments, and one where the Reynolds number based on the boundary-layer thickness and friction velocity is about the same both for the DNS and the present experiments.

When plotting mean velocity we have chosen to plot $1-V^*/V_w^*$ rather than V^*/V_w^*. In the former case the variable is zero at the wall and velocity profiles

can be easily compared with velocity profiles over stationary plates. With respect to even moments of the fluctuating velocity (such as the variance or the flatness) no change is necessary but odd moments (such as the skewness) have the opposite sign compared with the stationary case and are therefore plotted with the sign changed.

3.1. *Determination of the skin-friction velocity*

In the present work we estimate the skin-friction velocity in a direct way by measuring the velocity distribution in the near-wall region, i.e. within the viscous sublayer. Recently Alfredsson *et al.* (2011) showed that the probability density functions (PDF) or equivalently the cumulative distribution functions (CDF) of the fluctuating streamwise velocity in 2DTBL is self similar in the near-wall region. The same approach is taken here, but now with respect to the azimuthal velocity. Figure 5 shows the mean azimuthal velocity profile in the near-wall region together with five different values of the CDF, namely 0.2, 0.3, 0.4, 0.5 and 0.6. If the CDF is self similar, then straight lines through the points should all meet at the same position at zero velocity, which corresponds to the wall position. As can be seen this is the case for the present data, the wall position is estimated with an error of about 2 μm and less than 1% in velocity. This gives confidence in both the determination of the wall position and extrapolation of the calibration as described in section 2.2.

It is noteworthy to see that the effect of the heat conduction seems to be negligible in the present case in contrast to the velocity data in figure 9 in Alfredsson *et al.* (2011). This is clearly an effect of the high velocity close to the wall with respect to the hot wire thereby limiting the effect of heat transfer to the wall.

The azimuthal skin friction at the wall τ_w^* is calculated by the slope of the mean velocity data in the viscous sublayer ($z^+ < 5$) and the estimated wall position where $z^+ = v_\tau^* z^*/\nu^*$, v_τ^* is the friction velocity defined by $\sqrt{\tau_w^*/\rho}$, ρ is a density and ν^* is the kinematic viscosity.

3.2. *Mean flow and turbulence intensity statistics*

In figure 6 we show the so-called diagnostic plot introduced by Alfredsson & Örlü (2010) with the comparison of the 2DTBL data. The overall picture is the same for the two cases, however there are clear differences in the details. Close to the wall, in the viscous sublayer ($1 - V^*/V_w^* < 0.2$), the 2DTBL data show that the local turbulence intensity is close to 36-40% whereas for the rotating-disk flow data is about 30% (can be obtained from the slope of the curve in the viscous sublayer). The near-wall maximum is found for a higher value of $(1 - V^*/V_w^*)$ for the rotating disk compared with the 2DTBL and the local turbulence intensity is smaller in the outer region. However for the measurements on the rotating disk the sensor length is about 29 ℓ^* (see

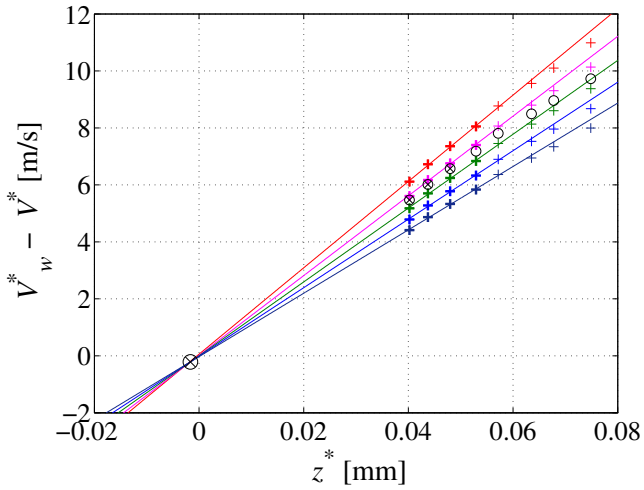

FIGURE 5. Application of the self-similarity of the CDFs in the viscous sublayer. The circles show the azimuthal mean velocity profile obtained through hot-wire measurement. The solid lines indicate the linear fits of CDFs in the viscous sublayer. The $\otimes$ is the estimated wall position by the linear fits of CDFs. The azimuthal friction velocity is calculated by the slope of the three mean velocity measurements closest to the surface together with wall value (all marked in the graph by $\otimes$). For the data shown here, v_τ^* and ℓ^* are 1.43 m/s and 10.5 μm, respectively.

Table 1) so one would expect some effects from spatial averaging along the sensor. An estimate based on the work by Segalini *et al.* (2011) shows that at the maximum of the rms distribution in the near-wall region measurements could be underestimated by as much as 10%.

The mean azimuthal velocity profiles normalized with inner scales in the standard semi-logarithmic plot are shown in figure 7, where V_w^+ is the local disk velocity normalized by the azimuthal friction velocity, V^+ is the azimuthal mean velocity normalized by the azimuthal friction velocity and z^+ is the wall-normal height from the disk normalized by inner scales which are given as $z^+ = v_\tau^* z^*/\nu^*$, respectively.

The rotating disk velocity profiles look as expected close to the wall and overlap nicely with the DNS profiles there. In the logarithmic region they are slightly above the standard logarithmic profile, but seem to have the same slope, i.e. the same Kàrmàn constant (κ). Here the straight line corresponds to the logarithmic law with $\kappa = 0.41$ and logarithmic intercept of 5.0. However,

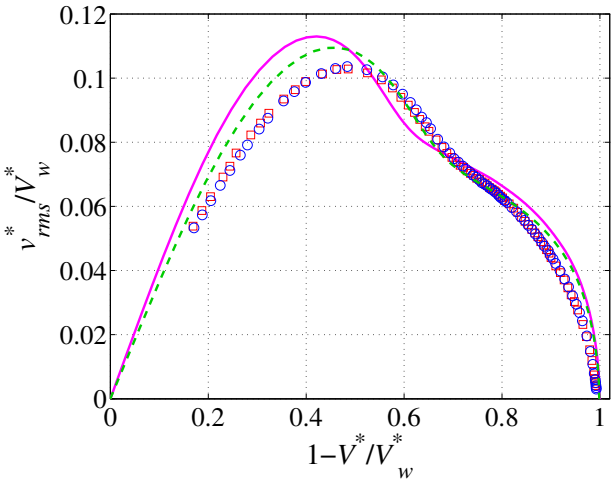

FIGURE 6. Diagnostic plot at T01 (○), T02 (□), 2D01 (dashed line), 2D02 (solid line).

a large difference between the two cases is found in the outer region, i.e. the wake region, where the wake contribution is much smaller for vKTBL as also pointed out by Littell & Eaton (1994).

If plotted in outer scaling, see figure 8, the difference between the 2DTBL and the vKTBL is even more pronounced in the outer region. This is an interesting observation and we hypothesise that it has to do with the inflow towards the disk. It is well known that for a favourable pressure gradient the wake contribution in the outer region becomes smaller which could be a similar effect to what is observed here. An even more appropriate comparison could be made with the asymptotic turbulent suction boundary layer that has an inflow from the free stream resulting in an almost nonexistent wake contribution (see Schlatter & Örlü 2011). With the outer scaling using Δ^* the boundary layer seems to be thicker than the corresponding 2DTBL cases.

The variance profiles (or rather the rms-profile) are plotted in figure 9. The overall features are similar to what one would expect from a 2DTBL profile, the inner maximum is at approximately $z^+ = 14$, however the amplitude is lower than for the 2DTBL profiles. As mentioned before the hot-wire sensor length is almost 30 wall units which gives rise to spatial averaging and hence a lower amplitude of the rms. The spatial averaging along the hot-wire probe may explain most of the difference between the two cases in the inner region. When plotted normalized by the outer length scale the difference becomes exaggerated in the outer region, see figure 10 as also here it seems that the rotating-disk boundary layer is thicker with this scaling.

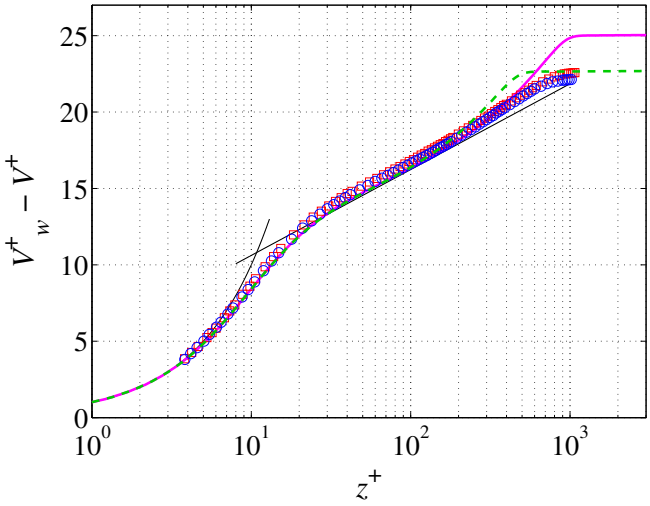

FIGURE 7. Mean azimuthal velocity profile normalized by the inner scales in logarithmic plot. The symbols are same as in Fig. 6.

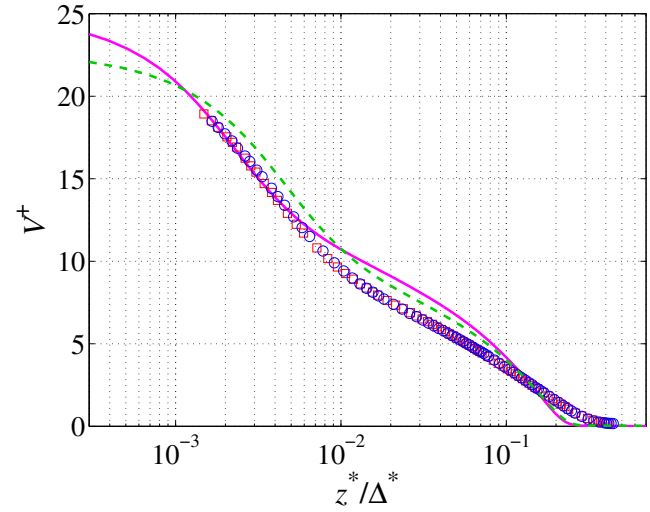

FIGURE 8. Mean azimuhtal velocity profile normalized by the outer scales in logarithmic plot. The symbols are same as in Fig. 6.

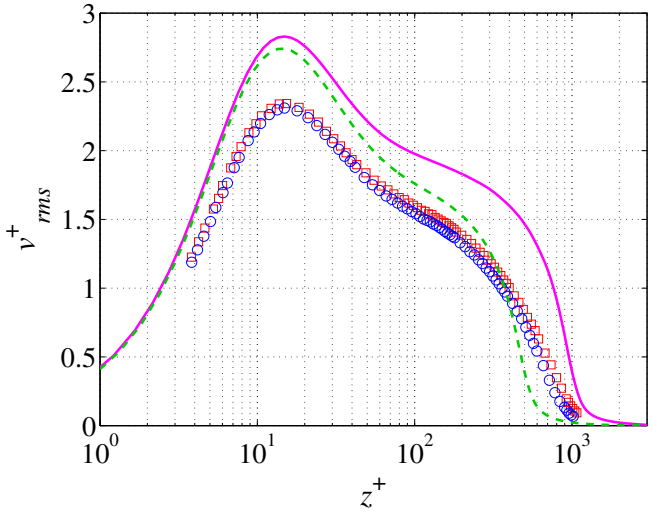

FIGURE 9. Azimuthal fluctuation velocity profile normalized by the inner scales in logarithmic plot. The symbols are the same as in figure 6.

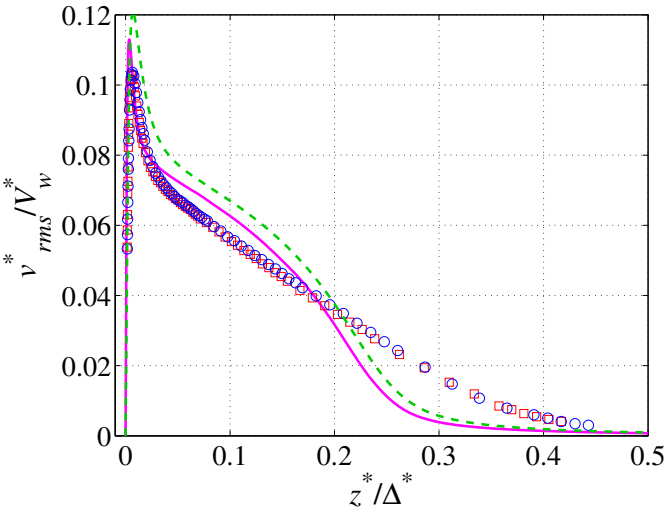

FIGURE 10. Azimuthal fluctuation velocity profile nomalized by the outer scales. Same data as in figure 9.

3.3. *Skewness and flatness profiles*

The higher moments, skewness and flatness were also calculated. The skewness factor is for the rotating disk flow defined as

$$S_v = -\frac{\overline{v^3}}{v_{rms}^3}$$

where the negative sign is used to allow comparison with the case of a stationary plate. The flatness factor is defined as

$$F_v = \frac{\overline{v^4}}{v_{rms}^4}$$

The skewness factor (see figure 11) shows a similar behaviour to what is known for 2DTBL flows near the wall. S_v reaches a value close to one at the wall itself, is almost constant within the viscous sublayer, whereafter it decreases, becomes zero around $z^+ = 15$ and is almost constant and slightly negative in the logarithmic region after which it becomes highly negative in the intermittent part of the wake region before it goes towards zero in the undisturbed freestream. With inner scaling the intermittent region seems to occur in between the two chosen 2DTBL profiles, and shows slightly larger negative values.

In outer scaling the rotating disk boundary layer is clearly seen to be thicker than the 2DTBL as shown in figure 12.

A similar comparison can be done with the flatness factor (see figure 13). Near the wall F_v approaches a value around 5 whereafter it decreases, becomes 3 (the Gaussian value) around $z^+ = 7$ has a minimum around $z^+ = 15$ and then is again around 3 in the logarithmic region, before it peaks in the outer intermittent wake region. Also here the vKTBL shows a higher flatness factor in that region as compared with the 2DTBL. The same feature as for the skewness is seen with outer scaling; the vKTBL seems to be thicker with this scaling (see figure 14).

3.4. *Turbulence spectra*

The spectral maps of the azimuthal velocity fluctuations are shown in figure 15 and figure 16 in the form of premultiplied spectra. The spectra are measured at 78 different z^+ positions between $z^+ \approx 4$ and $z^+ \approx 1000$ and plotted as a spectral map as function of z^+ and t^+, i.e. the inverse of the frequency $(f^+)^{-1}$. There is a maximum around $z^+ = 15$ where also the maximum in rms is located. The corresponding frequency or rather its inverse is at $t^+ \approx 40$. The spectra also show that the maximum energy content goes to larger time scales, i.e. lower frequencies away from the wall. The maximum that is observed for small z^+ around $t^+ = 5000$ is due to the imbalance of the disk and can be seen not to interfere with the turbulent scales.

An interesting comparison can be done with the spectral maps published by Örlü & Schlatter (2012) for 2DTBL (obtained both from experiments and DNS) where the spectral map is different both quantitatively and qualitatively. In that case spectra have their inner maximum at a t^+ of 100, and the frequency for the maximum energy content is almost constant across the boundary layer. An explanation of both these behaviours may be that in the vKTBL the structures become inclined due to the three-dimensional nature of the vKTBL and one may say that from the hot wire's point of view the structures will then 'look' shorter. On the other hand, Littell & Eaton (1994) showed that the maximum inclination of the mean profile is less than 10° which is too little to explain the difference from $t^+ = 40$ to $t^+ = 100$.

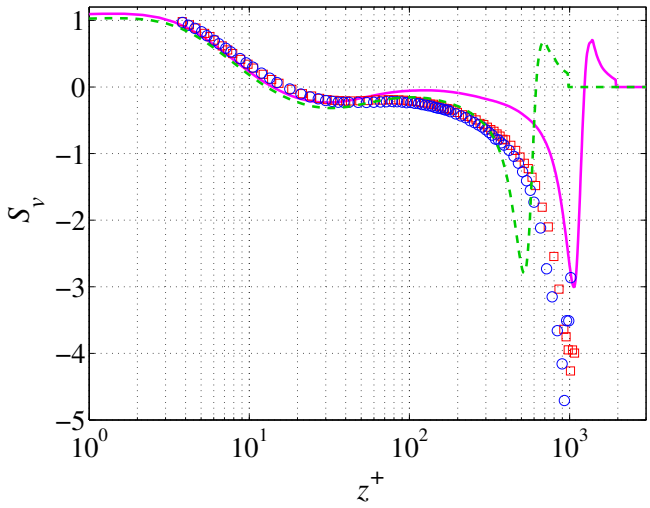

FIGURE 11. Skewness profile of azimuthal velocity in logarithmic and inner scale plot. The symbols are same as in figure 6. Note that the skewness in T01, T02 is multiplied by -1.

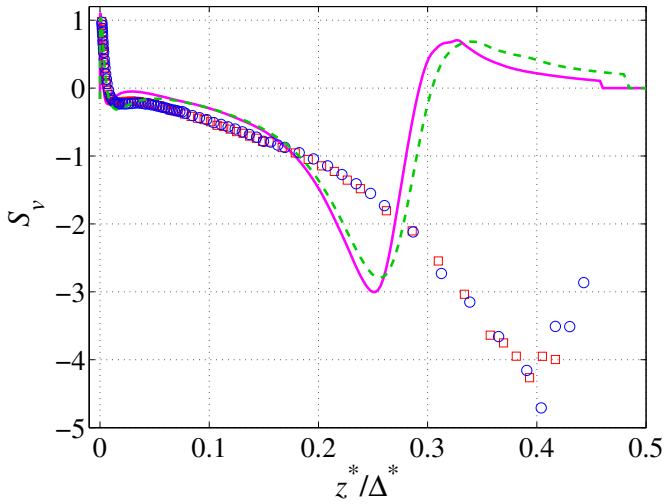

FIGURE 12. Skewness profile of azimuthal velocity in outer scale plot. Same data as in figure 11.

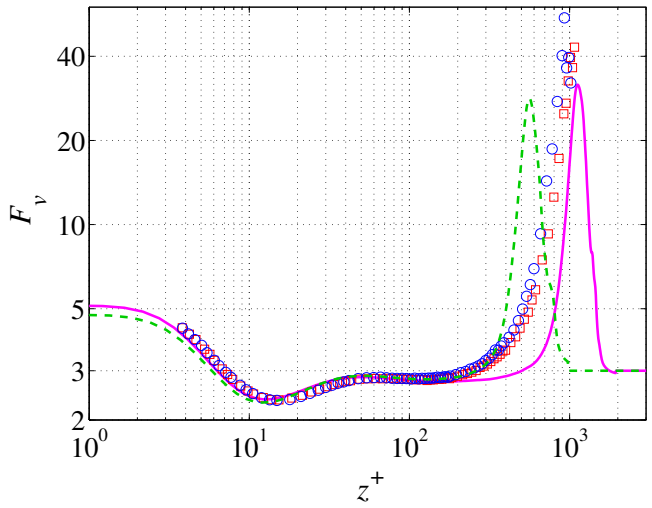

FIGURE 13. Flatness profile of azimuthal velocity in logarithmic and inner scale plot. The symbols are same as in figure 6.

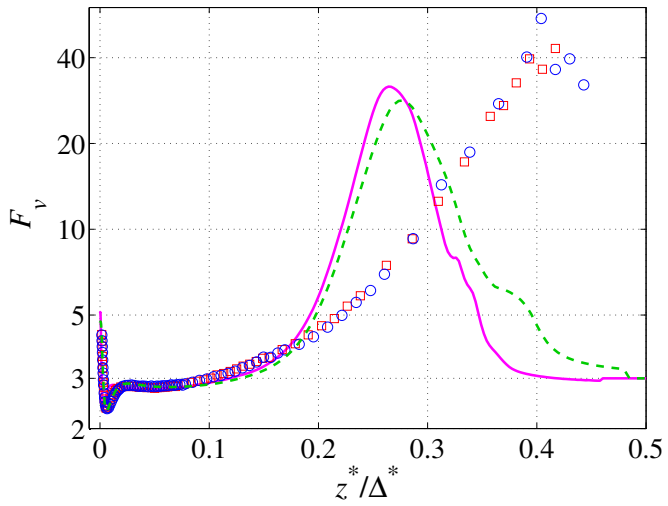

FIGURE 14. Flatness profile of azimuthal velocity in logarithmic and outer scale plot. Same data as in figure 13.

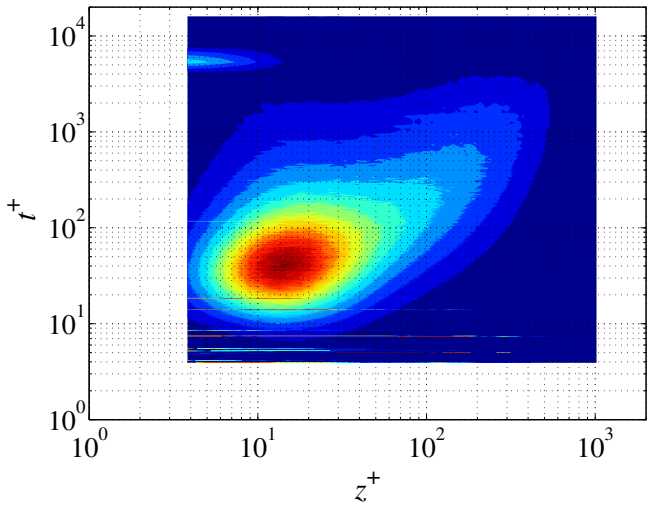

FIGURE 15. Premultiplied spectrum of T01. Filled contours are equally spaced.

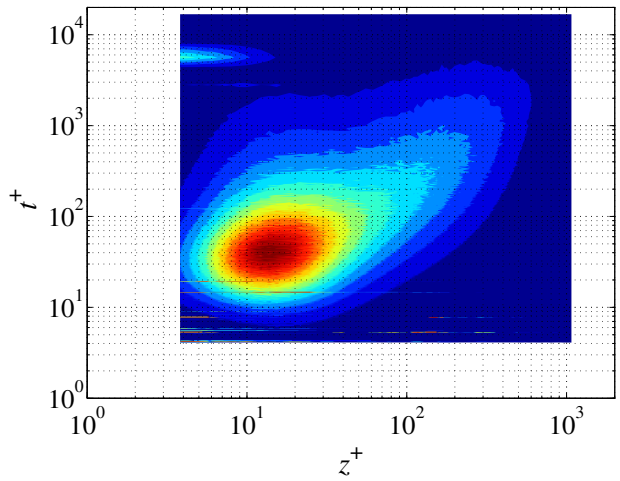

FIGURE 16. Premultiplied spectrum of T02. Filled contours are equally spaced.

4. Conclusions

We have here presented experimental results for turbulent boundary layers driven by a rotating disk. We compare the mean velocity and variance as well as higher moments with results obtained for a 2DTBL. Here we have to make a choice what Reynolds number one should chose for the comparison. We chose one Reynolds number for the 2DTBL case with a similar skin friction coefficient and one with about the same Re_τ as for the vKTBL.

In contrast to earlier studies we claim to have been able to determine the skin friction (or friction velocity) accurately by direct measurement of the velocity distribution close to the disk.

The mean azimuthal velocity profile shows strong similarity with the velocity profile in a 2DTBL especially in the near-wall region and in the logarithmic region. However, the wake region is clearly less pronounced than for the 2DTBL. This also results in a lower shape factor for the vKTBL as compared to the 2DTBL. Also when normalizing the normal distance from the plate with the Rotta-Clauser length the differences between the vKTBL and the 2DTBL become apparent in the outer region.

The turbulence intensities are quite similar in qualitative terms near the wall, although quantitatively the experimental results for the vKTBL show lower values. This can be explained by the spatial averaging of the hot-wire probe which in this case has a length of almost 30 ℓ^*, despite the fact that the sensing length is only 0.3 mm long.

Also the higher moments, i.e. the skewness and flatness factors, show very similar behaviour in the near-wall and logarithmic regions, as compared with the 2DTBL. However as also in the other cases there is a difference in the outer region.

An interesting aspect that needs further investigation is the difference between the spectral maps for the vKTBL and the 2DTBL. First we find that the spectral peak corresponding to the maximum in the rms distribution near the wall is located at a different (higher) frequency for the vKTBL. The spectral maps also differ from that of a 2DTBL as reported by Örlü & Schlatter (2012) where the maximum frequency for the energy in the spectra is almost constant across the boundary layer.

In summary, three main conclusions can be drawn from the present work:

- The flow statistics close to the wall and in the logarithmic region correspond well to that of 2DTBL.
- The flow in the outer intermittent region is quite different, which may be an influence of the inflow normal to the disk.
- The spectral frequencies do not scale on inner variables when comparing the two cases, and the shape of the spectral maps also differs. This may be an effect of the three-dimensional nature of the vKTBL.

Acknowledgement

This work is supported by the Swedish Research Foundation and Linné FLOW Centre at KTH. Ramis Örlü is acknowledge for useful discussions.

References

Alfredsson, P. H. & Örlü, R. 2010 The diagnostic plot - a litmus test for wall bounded turbulence data. *Eur. J. Mech. - B/Fluids* **29**, 403–406.

Alfredsson, P. H., Örlü, R. & Schlatter, P. 2011 The viscous sublayer revisited: exploiting self-similarity to determine the wall position and friction velocity. *Exp. Fluids* http://www.springerlink.com/index/10.1007/s00348-011-1048-8.

Crespo del Arco, E., Serre, E., Bontoux, P. & Launder, B. E. 2005 Stability, transition and turbulence in rotating cavities. In *Instability of Flows* (ed. M. Rahman), pp. 141–195. WIT Press.

Cham, T.-S. & Head, M. R. 1969 Turbulent boundary-layer flow on a rotating disk. *J. Fluid Mech.* **37**, 129–147.

Clauser, F. H. 1954 Turbulent boundary layers in adverse pressure gradients. *AIAA J.* **21**, 91–108.

Davies, C. & Carpenter, P.W. 2003 Global behaviour corresponding to the absolute instability of the rotating-disc boundary layer. *J. Fluid Mech.* **486**, 287–329.

Erian, F. F. & Tong, Y. H. 1971 Turbulent flow due to a rotating disk. *Phys. Fluids* **14**, 2588–2591.

Goldstein, S. 1935 On the resistance to the rotation of a disc immersed in a fluid. *Math. Proc. Camb. Phil. Soc.* **31**, 232–241.

Gregory, N., Stuart, J. T. & Walker, W. S. 1955 On the stability of three-dimensional boundary layers with application to the flow due to a rotating disk. *Phil. Trans. R. Soc. Lond.* **248**, 155–199.

Imayama, S., Alfredsson, P. H. & Lingwood, R. J. 2012 A new way to describe the transition characteristics of a rotating-disk boundary-layer flow. *Phys. Fluids* **24**, 031701.

von Kármán, T. 1921 Über laminare und turbulent Reibung. *Z. Angew. Math. Mech.* **1**, 233–252.

Kobayashi, R., Kohama, Y. & Takamadate, C. 1980 Spiral vortices in boundary layer transition regime on a rotating disk. *Acta Mechanica* **35**, 71–82.

Kohama, Y. 1984 Study on boundary layer transition of a rotating disk. *Acta Mechanica* **50**, 193–199.

Lingwood, R. J. 1995 Absolute instability of the boundary layer on a rotating disk. *J. Fluid Mech.* **299**, 17–33.

Lingwood, R. J. 1996 An experimental study of absolute instability of the rotating-disk boundary-layer flow. *J. Fluid Mech.* **314**, 373–405.

Littell, H. S. & Eaton, J. K. 1994 Turbulence characteristics of the boundary layer on a rotating disk. *J. Fluid Mech.* **266**, 175–207.

Mager, A. 1952 Generalisation of boundary layer momentum-integral equations to three-dimensional flows including those of rotating system. *NACA Rep. 1067* .

Nagib, H., Christophorou, C., Rüedi, J.-D. & Monkewitz, P. 2004 Can we ever rely on results from wall-bounded turbulent flows without direct measurements of wall shear stress AIAA paper-2004-2392.

Nagib, H. M. & Chauhan, K. A. 2008 Variations of von Kàrmàn coefficient in canonical flows. *Phys. Fluids* **20**, 101518.

Örlü, R. & Schlatter, P. 2012 Turbulent boundary-layer flow: Comparing experiments with DNS. In *Prog. Turbulence and Wind Energy IV* (ed. M. Oberlack, J. Peinke, A. Talamelli, L. Castillo & M. Hölling), *Springer Proceedings in Physics*, vol. 141, pp. 213–216. Springer Berlin Heidelberg.

Pier, B. 2003 Finite-amplitude crossflow vortices, secondary instability and transition in the rotating-disk boundary layer. *J. Fluid Mech.* **487**, 315–343.

Schlatter, P. & Örlü, R. 2010 Assessment of direct numerical simulation data of turbulent boundary layers. *J. Fluid Mech.* **659**, 116–126.

Schlatter, P. & Örlü, R. 2011 Turbulent asymptotic suction boundary layers studied by simulation. *J. Phys.: Conf. Ser.* **318**, 022020.

Segalini, A., Örlü, R., Schlatter, P., Alfredsson, P. H., Rüedi, J.-D. & Talamelli, A. 2011 A method to estimate turbulence intensity and transverse Taylor microscale in turbulent flows from spatially averaged hot-wire data. *Exp Fluids* **51**, 693–700.

Theodorsen, T. & Regier, A.A. 1944 Experiments on drag of revolving disks, cylinders and streamline rods at high speeds. *NACA Rep. 793* .

Thompson, B. G. J. 1965 A new two-parameter family of mean velocity profiles for incompressible turbulent boundary layers on smooth walls. *Aero. Res. Coun. R & M 3463* .